Graduate School of Science
Nagoya University

Experimental study of discrete symmetry in a compound nucleus using polarized neutrons

by

Tomoki Yamamoto

A dissertation submitted in partial fulfillment of the requirements for the degree of

Doctor of Science

February 2021

Acknowledgements

Firstly, I would like to express my sincere gratitude to my supervisor Prof. Hirohiko M. Shimizu in Particle property laboratory for the continuous support of my Ph.D study, for his patience, motivation, and immense knowledge. His guidance helped me in all the time of research and writing of this thesis. I could not have imagined having a better advisor and mentor for my Ph.D study.

Apart from my supervisor, I would like to thank Associate Prof. Masaaki Kitaguchi and Designated Associate Prof. Katsuya Hirota for their encouragement and insightful suggestions for six years since I joined the laboratory as an undergraduate student. I am very grateful to Assistant Prof. Takuya Okudaira for being able to lead a very exciting research life by holding discussions day and night, not only in physics. His passionate and sincere attitude toward physics serves as a model for researchers and is highly respected.

I would like to express my special thanks to NOPTREX collaborators, Associate Prof. Tamaki Yoshioka, Associate Prof. Shima Tatsushi, Associate Prof. Hiroyuki Fujioka, and Assistant Prof. Masataka Iinuma. Advice on analysis and deep insight must have improved the quality of my research. I would like to express my deep gratitude to Mr. Shunsuke Takada and Mr. Jun Koga for sharing many difficulties in our experiments and for their friendly competition. I am deeply grateful that Dr. Christopher C. Haddock always corrected my English writing carefully. I will never forget the happy days I spent with him in Japan. I would like to thank Ms. Danielle Schaper for taking care of me during the experiment at the Los Alamos laboratory. I would like to express my gratitude to Dr. Kenji Sakai, Dr. Takayuki Oku and Lecture Takashi Ino for their assistance in preparing the polarization experiment and giving advice on the experiment. I would like to express my deep gratitude to Dr. Atsushi Kimura and Dr. Shoji Nakamura who were in charge of the maintenance of the beamline. They always responded to various equipment troubles every time.

Thank my colleagues in the laboratory and other universities. They made my life more colorful and have enriched me with a lot of precious memories. Thank you for always responding to my confusing jokes without getting tired of them. I would like to thank secretaries Ms.

Kazumi Hasegawa, Ms. Eri Ozaki , and Ms. Yoko Yamamoto for always helping me with complicated paperwork and applications.

Last, but not least, I would like to thank my parents and my sister for their unconditional love and support.

Abstract

It is difficult to explain the existence of the present "Matter-Dominated Universe" using only the framework of the Standard Model. This strongly suggests CP-violation Beyond the Standard Model, which has been explored by various experiments. CP-violation and T-violation are equivalent via the CPT theorem. Therefore, we plan to search for T-violation using the phenomenon that the symmetry violation is enhanced in some nuclear reactions in order to access CP-violation Beyond the Standard Model.

P-violation in slow neutron and nuclear reactions has been observed to be up to 10^6 times larger than that in nucleon nucleon reactions. This is theoretically interpreted as resulting from the fact that metastable states are formed by the reaction of neutron and nucleus, and partial waves with different parities are mixed for a long time to enhance P-violation in nucleon nucleon reactions (*sp*-mixing model). Building upon this *sp*-mixing model, it has been suggested that T-violation is enhanced in these nuclear reactions as well as P-violation. The parameter $\kappa(J)$ indicating the degree of T-violation enhancement in these nuclear reactions is derived from nuclear structure and can be determined by angular correlation measurements in (n, γ) reactions. In a previous study of ^{139}La with regards to large P-violation, $\kappa(J)$ was constrained by measuring the angular distribution of the $^{139}\mathrm{La}(n, \gamma)$ reaction using unpolarized neutrons. On the other hand, more accurate $\kappa(J)$ are required to discuss the feasibility of the T-violation search. The realization of higher accuracy was achieved by measuring the different correlation terms in the (n, γ) reaction. Correlation measurements have been carried out by installing a neutron polarizer into a high intensity neutron source at J-PARC to polarize incident neutrons. As a result, a significant asymmetry in the emission direction of γ-ray in the $^{139}\mathrm{La}(\vec{n}, \gamma)$ reaction was found $A_{\mathrm{LR}}^{\mathrm{gnd}} = 0.73 \pm 0.14$. This asymmetry was analyzed using the *sp*-mixing model, and a high accuracy determination of the enhancement parameter was realized as $\kappa(J) = 1.62^{+2.60}_{-0.95}$. The feasibility of a T-violation search is discussed quantitatively, and the required performance and measurement methodology are discussed.

Contents

List of Figures

List of Tables

Chapter 1

Introduction

The Standard Model (SM) was almost completed by the discovery of Higgs boson at the Large Hadron Collider in 2012 [1, 2]. The SM has succeeded in quantitatively explaining various experimental results as well as predicting phenomena. However, there remain some experimental observations and known phenomena which are difficult to explain using only SM physics. This fact suggests the existence of physics beyond SM (BSM), and its elucidation is the main theme in particle physics today. One of the facts that cannot be explained by SM is a "Matter-Dominated Universe". There is a discrepancy of 10^9 between the asymmetry of matter and antimatter quantities in today's universe obtained by cosmological observations and that predicted by SM [3]. Sakharov pointed out that charge symmetry violation (C-violation) and charge conjugation parity symmetry violation (CP-violation) must exist as one of the conditions for today's universe to be matter-dominated [4]. Since this requires the existence of additional CP-violation in BSM, it is an urgent matter to clarify it from both theoretical and experimental standpoints. Various experiments have searched for BSM CP-violation. For example, in high energy experiments using a large collider, CP-violation is directly searched for by generating new particles [5]. On the other hand, since CP-violation and time reversal symmetry violation (T-violation) are equivalent via CPT theorem, CP-violation is also searched for indirectly by searching for T-violation in low energy phenomena. On the experimental side, theoretical constraints for BSM physics are given by various experiments and clues for new physics are searched for from various viewpoints.

1.1 CP-violation in the Standard Model

The SM explains CP-violation obtained by existing experimental results well. CP-violation within the SM framework can be generated from two sources. One is the existence of complex

phases contained in the Cabibbo-Kobayashi-Maskawa (CKM) matrix. The charged current associated with the exchange of W boson can be described as follows and which can be changed into quarks of different generations via the weak interaction

$$J^{\mu} = \begin{pmatrix} \bar{u} & \bar{c} & \bar{t} \end{pmatrix} \gamma^{\mu} \frac{(1-\gamma^5)}{2} V_{\rm CKM} \begin{pmatrix} d \\ s \\ b \end{pmatrix}, \tag{1.1}$$

where γ^{μ} is the gamma matrix, $\gamma^5 = i\gamma^0\gamma^1\gamma^2\gamma^3$, and CKM matrix $V_{\rm CKM}$ is a 3×3 unitary matrix and given as [6]

$$\begin{aligned} V_{\rm CKM} &= \begin{pmatrix} V_{ud} & V_{us} & V_{ub} \\ V_{cd} & V_{cs} & V_{cb} \\ V_{td} & V_{ts} & V_{tb} \end{pmatrix} = \begin{pmatrix} c_{12}c_{13} & s_{12}c_{13} & s_{13}e^{-i\delta} \\ -s_{12}c_{23} - c_{12}s_{23}s_{13}e^{i\delta} & c_{12}c_{23} - s_{12}s_{23}s_{13}e^{i\delta} & s_{23}c_{13} \\ s_{12}s_{23} - c_{12}c_{23}s_{13}e^{i\delta} & -c_{12}s_{23} - s_{12}c_{23}s_{13}e^{i\delta} & c_{23}c_{13} \end{pmatrix} \\ &= \begin{pmatrix} 0.97446 \pm 0.00010 & 0.22452 \pm 0.00044 & 0.00365 \pm 0.00012 \\ 0.22438 \pm 0.00044 & 0.97359^{+0.00010}_{-0.00011} & 0.04214 \pm 0.00076 \\ 0.00896^{+0.00024}_{-0.00023} & 0.04133 \pm 0.00074 & 0.999105 \pm 0.000032 \end{pmatrix}, \end{aligned} \tag{1.2}$$

where $s_{ij} = \sin\theta_{ij}$, $c_{ij} = \cos\theta_{ij}$, θ_{ij} is flavor mixing angles, and δ is the complex phase, which violates CP.

The other source of CP-violation is due to the θ term in Quantum Chromodynamics (QCD). The Lagrangian of QCD is given as

$$\mathcal{L}_{\rm QCD} = \sum_f \overline{q_f} \left(i\gamma^{\mu} \left(\partial_{\mu} + ig_s \sum_a G^a_{\mu} \frac{\lambda_a}{2} \right) - m_f \right) q_f - \frac{1}{4} \sum_a G^a_{\mu\nu} G^{a\mu\nu} + \frac{g_s^2 \theta}{32\pi^2} \sum_a G^a_{\mu\nu} \tilde{G}^{a\mu\nu}, \tag{1.3}$$

where q_f is the quark field for a quark flavor f with its mass m_f , λ_a are Gell-Mann matrices, a subscript a runs from 1 to 8 for the 8 kinds of gluons, g_s is the strong coupling constant, G^a_{μ} is the gluon field. $G^a_{\mu\nu}$ and $\tilde{G}^{a\mu\nu}$ are defined as follows

$$\begin{aligned} G^a_{\mu\nu} &\equiv \partial_{\mu} G^a_{\nu} - \partial_{\nu} G^a_{\mu} - g_s \sum_{b,c} f_{abc} G^b_{\mu} G^c_{\nu} \\ \tilde{G}^{a\mu\nu} &\equiv \frac{1}{2} \varepsilon^{\mu\nu\lambda\rho} G^a_{\lambda\rho}, \end{aligned} \tag{1.4}$$

where f_{abc} are completely antisymmetric constants, $\varepsilon^{\mu\nu\lambda\rho}$ is completely antisymmetric tensor in four dimension. The third term in Eq.1.3 is called the θ term and violates CP. However, the value of θ is limited to $|\theta| < \mathcal{O}\left(10^{-10}\right)$ from the measurement of the neutron electric dipole moment (nEDM). This leads to very small CP-violation in the strong interaction. It is pointed

out that θ may be strongly suppressed by some mechanism because of its unnaturally small value in spite of its parameter capable of taking a value ranging from 0 to 2π, which is called the strong CP problem [7, 8]. In this context, the search for unknown CP-violation is very important in understanding QCD and the Matter-Dominated Universe.

1.2 T-violation search by EDM measurement

The electric dipole moment of elementary particles or composite particles can be used as a powerful probe of T-violation in low energy phenomenon. The existence of the EDM indicates T-violation as shown in Fig.1.1. The effective Hamiltonian of a magnetic moment $\boldsymbol{\mu}$, electric dipole moment $\boldsymbol{d}$ in both a magnetic field $\boldsymbol{B}$ and an electric field $\boldsymbol{E}$ is expressed as

$$H_{\text{eff}} = -\boldsymbol{\mu} \cdot \boldsymbol{B} - \boldsymbol{d} \cdot \boldsymbol{E}. \tag{1.5}$$

Under the T transformation $\boldsymbol{\mu}$, $\boldsymbol{B}$, $\boldsymbol{d}$, $\boldsymbol{E}$ are transformed as follows

$$\boldsymbol{\mu} \to -\boldsymbol{\mu},\ \boldsymbol{B} \to -\boldsymbol{B},\ \boldsymbol{d} \to -\boldsymbol{d},\ \boldsymbol{E} \to \boldsymbol{E}. \tag{1.6}$$

Therefore, the Hamiltonian H_{eff} is transformed by the T transformation as follows:

$$H_{\text{eff}} = -\boldsymbol{\mu} \cdot \boldsymbol{B} + \boldsymbol{d} \cdot \boldsymbol{E}. \tag{1.7}$$

The Hamiltonian H_{eff} is invariant for the T transformation only when the value of d is zero. A Larmor frequency ω in the electric field and the magnetic field is given as follows

$$\omega = -\frac{2}{\hbar}\left(\mu B \pm dE\right). \tag{1.8}$$

The difference of the Larmor frequency with respect to the direction of the electric field is measured.

Since the EDM predicted by SM is very small in general (nEDM $d_n^{\text{SM}} \leq 10^{-32}\, e \cdot \text{cm}$, electron EDM $d_e^{\text{SM}} \leq 10^{-38}\, e \cdot \text{cm}$ [9]), the discovery of an EDM that can be measured by current experimental techniques is directly connected to new physics. Figure 1.2 shows how fundamental CP-violation propagates and appears in various energy regions and sectors as observable EDMs. Unknown CP-violation is searched for through EDM measurements in various regions. The measurement of nEDM is currently the most sensitive for T-violation [10]. Figure 1.3 shows the transition of the upper limit of nEDM, and various theoretical predictions have been rejected. The search sensitivity for T-violation year by year has improved due to performance

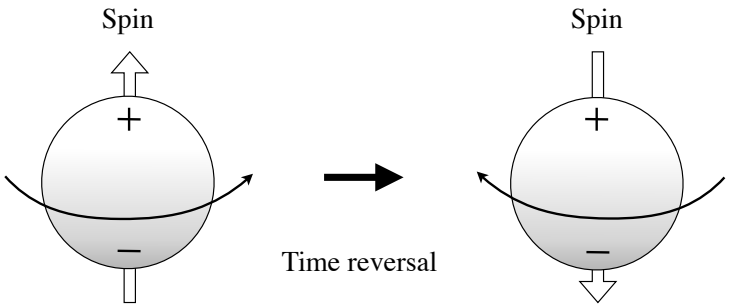

Figure 1.1: Illustration of time reversal of particles with EDM. The spin is reversed for time reversal, but the EDM is invariant. Therefore, the presence of EDM in a static system implies T-violation.

enhancement of the equipment and through upgrading the various control technologies, and it is expected that the search sensitivity will continue to improve. On the other hand, it is very significant that experiments with different systematic uncertainties are independently performed to search for unknown physics. Therefore our group is planning a new type of T-violation search using low energy nuclear reactions, distinct from EDM measurements.

1.3 T-violation search by nuclear reaction

Large parity violation (P-violation) has been observed in some neutron nucleus (n+N) reactions. This size may be enhanced up to 10^6 times as large as the size of P-violation in the $N + N$ reaction. It is understood that a compound state is formed by the $n + N$ reaction, and the P-violation caused by the weak interaction is enhanced as a result of the mixing of partial waves with opposite parities over a long period of time [26]. In this compound nuclear reaction, it is suggested that T-violation is also enhanced by the same mechanism [27]. The T-odd term in the forward scattering of polarized neutrons and polarized nuclear reactions can be experimentally measured in order to search for T-violation [28]. When the neutron wavelength is large compared to the effective radius of the nuclear potential, the neutron behavior in the medium can be treated optically (Neutron optics). In measurements of T-odd terms in decay and scattering process, a final state interaction (FSI) caused by the difference between the final state and the initial state of the reaction exists. The existence of the FSI produces false T-violation, and it is one of the factors which make the T-violation search by measurement of the T-odd term difficult. On the other hand, in neutron optics the forward scattering process can be treated as a state invariant process, so that a T-violation search free from the FSI can be carried out. Therefore, it may become a very powerful search method from the viewpoint of direct access to T-violation.

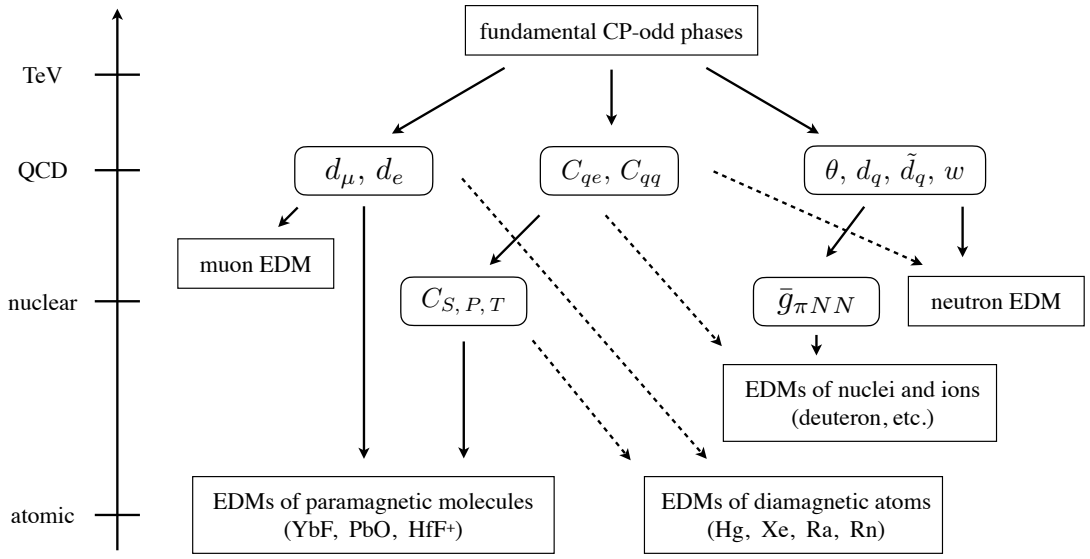

Figure 1.2: A schematic plot of the hierarchy of scales between the CP-odd sources and three generic classes of observable EDMs. The dashed lines indicate generically weaker dependencies. By combining the results of each EDM measurement, new physics can be found while theoretical predictions are restricted [11].

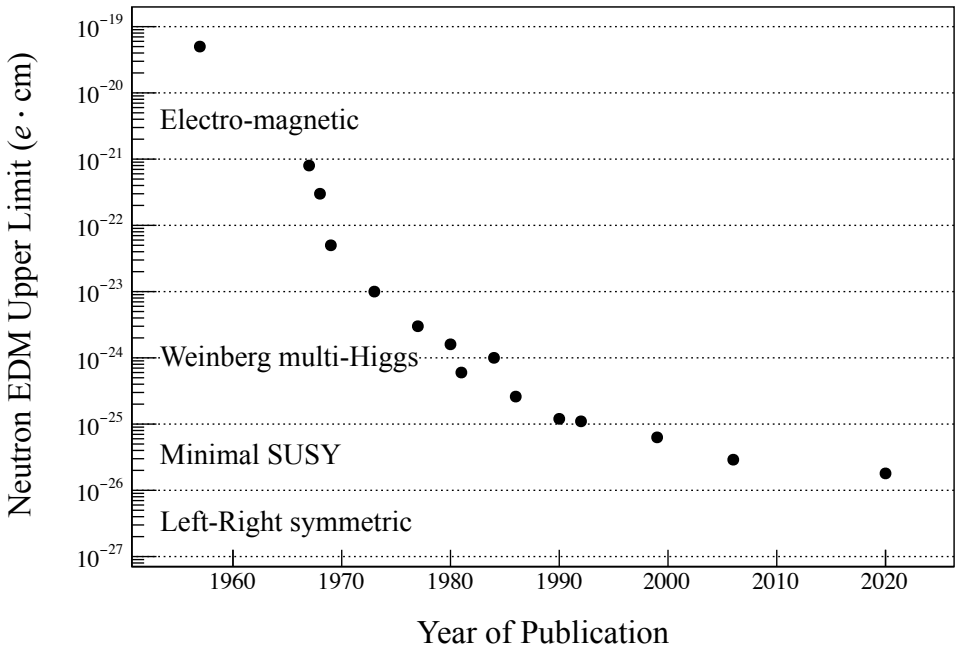

Figure 1.3: Historical transition of the upper limit of the experimental value of nEDM. A theoretical model corresponding to the size of nEDM is described on the left side. The size of the nEDM predicted by the SM is order of 10^{-31} e·cm [10, 12–25].

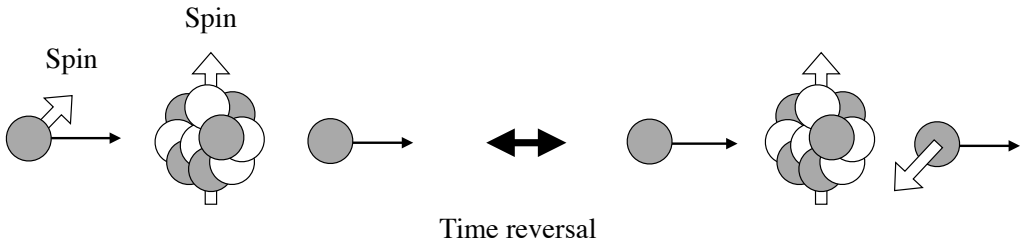

Figure 1.4: Illustration of the time inversion in the $n + N$ reaction. T-violation is searched for by measuring the triple vector correlation formed by the momentum vector of neutron, the polarization vector of the neutron and the polarization vector of nucleus in the reaction of polarized neutron and polarized nucleus.

As mentioned before, this experiment is important because it has systematic uncertainties different from EDM measurements. In addition, the physical quantities obtained by the experiment are important from the viewpoint that they can be complementary to those obtained by EDM measurements. The ratio of the T-violating cross section $\Delta\sigma_{\not T\not P}$ to the total cross section $\sigma_{\rm tot}$ in neutron deuteron scattering can be described as follows using the meson exchange model [29]:

$$\frac{\Delta\sigma_{\not T\not P}}{2\sigma_{\rm tot}} \simeq \frac{(-0.185\ \text{b})}{2\sigma_{\rm tot}} \left[\bar{g}_\pi^{(0)} + 0.26\bar{g}_\pi^{(1)}\right], \tag{1.9}$$

where $\bar{g}_\pi^{(I)}$ is pion nucleon T-violating coupling constant with isospin I. The cross section of T-violating forward scattering in compound nuclear reactions is proportional to Eq.1.9. The nEDM d_n and deuteron EDM d_D are also described using the meson exchange model as follows,

$$\begin{aligned} d_n &\simeq 0.14 \left[\bar{g}_\pi^{(0)} - \bar{g}_\pi^{(2)}\right] \\ d_D &\simeq 0.22\bar{g}_\pi^{(1)}. \end{aligned} \tag{1.10}$$

From Eq.1.9 and Eq.1.10, $\Delta\sigma_{\not T\not P}$ is sensitive to $\bar{g}_\pi^{(0)}$ and $\bar{g}_\pi^{(1)}$, d_n is sensitive to $\bar{g}_\pi^{(0)}$ and $\bar{g}_\pi^{(2)}$ and d_D is sensitive to $\bar{g}_\pi^{(1)}$. Figure 1.5 shows the dependence of $\bar{g}_\pi^{(0)}$, $\bar{g}_\pi^{(1)}$, and $\bar{g}_\pi^{(2)}$ on each measurement, the coupling constant of each rank can be determined by each measurement. The integration of the results of each measurement allows access to new physics.

In order to discuss the feasibility of the T-violation search quantitatively, it is necessary to experimentally determine the enhancement factor $\kappa(J)$ which is brought about in the extension of the symmetry violation enhancement mechanism in the nuclear reactions. The $\kappa(J)$ can be determined by measurements of correlation terms in the (n, γ) reaction. The $\kappa(J)$ has been determined in a previous study [30]. However, in order to design the T-violation search, further improvement of the determination accuracy of it is desired. In this study, the author aims to eliminate the uncertainties of $\kappa(J)$ through additional correlation term measurements. In

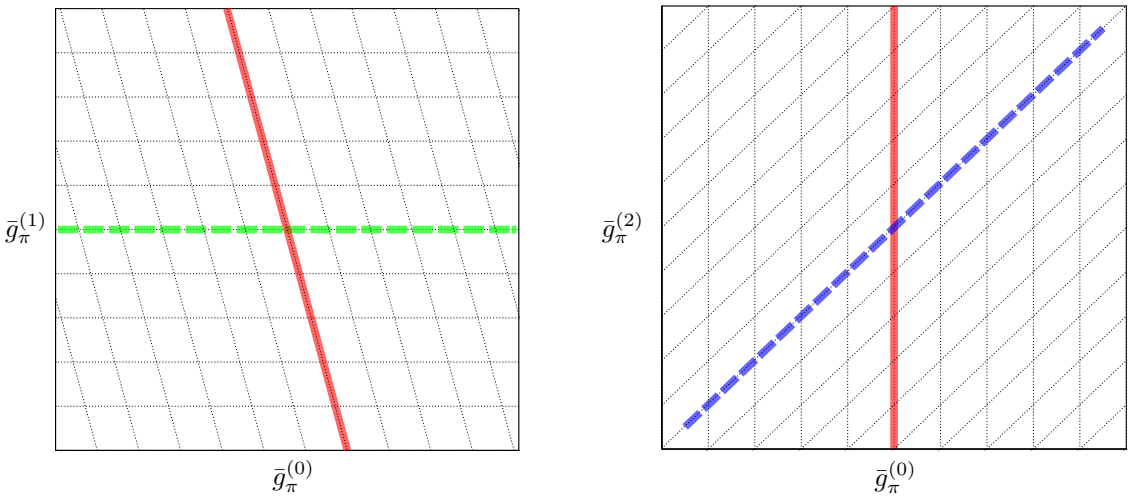

Figure 1.5: Complementary relationship between EDMs and the T-violation in compound nuclei. The left figure shows the dependence of the deuteron EDM and the T-violation on the T-violating π meson isoscalar and isovector coupling constants. The solid and dotted lines correspond to the T-violation and deuteron EDM, respectively. The right figure shows the dependence of neutron EDM and the T-violation on the T-violating π mesons isoscalar and isotensor coupling constants. The solid and dotted lines correspond to the T-violation and nEDM, respectively. The broken line axis shows how the coupling constant is limited by each measurement, and the limited region is determined parallel to the axis.

addition, the author estimated the reach of experimental sensitivity for the T-violation search and discussed the experimental design.

1.4 Thesis organization

In this thesis, the author discusses experimental studies of symmetry violation enhancement in nuclear reactions using polarized neutrons. In chapter 1, the research motivation is outlined. Chapter 2 discusses the theoretical understanding of the phenomenon of symmetry violation enhancement, the concept of a T-violation search exploiting it, and the method used to determine the $\kappa(J)$ via a (n,γ) correlation measurement. Chapter 3 describes the facilities and equipment used for the above (n,γ) correlation term measurements. Chapter 4 discusses (n,γ) correlation measurements. Chapter 5 discusses the results obtained in the measurement and the analysis using the results of previous studies. Chapter 6 estimates the experimental sensitivity of the T-violation search from the results of Chapter 5 and discusses the experimental design. Finally, Chapter 7 summarizes the entire thesis.

Chapter 2

Theoretical background

This chapter describes the theoretical interpretation for the enhancement of the symmetry violation phenomenon in compound nuclear reactions. The concept and features of the T-violation search using neutron induced compound nuclei are discussed. The method of determining the parameters necessary to estimate the experimental sensitivity of the search for T-violation is described.

2.1 Neutron-nucleus interaction

In a nuclear reaction, various processes can be observed according to the energy of the reaction. There are roughly four processes in the reaction: "Optical potential scattering processes" which do not excite the nucleus while interacting with nuclear potential, "Direct processes" which involve only a few nucleons in the nucleus (it is known that this process takes approximately 10^{-21} s, which is equivalent to the time required for a nucleon to pass through the nuclear region), "Pre-equilibrium processes" which involve multiple nucleons in nucleus, and "Compound nuclear process" which is the process in which the energy of the incident particle propagates throughout the whole nucleus over a relatively long time period of $\sim 10^{-16}$ s. In particular when the incident particle is a neutron, it can easily penetrate into the nucleus at low energies because it is not affected by the Coulomb potential of the nucleus due to its electric neutrality. Therefore, in low energy neutron - nucleus reactions, it is common to form compound nuclei without a direct process. It is possible to observe the phenomenon which deeply reflects the metastable state and properties of the many-body system in a heavy nuclei.

Table 2.1: Longitudinal asymmetry in $\vec{p}p$ scattering.

Proton energy (MeV)	A_{NN}
15	$(-1.7 \pm 0.8) \times 10^{-7}$ [31]
45	$(-2.31 \pm 0.89) \times 10^{-7}$ [32]
45	$(-1.50 \pm 0.22) \times 10^{-7}$ [33]
800	$(+2.4 \pm 1.1) \times 10^{-7}$ [34]

2.2 P-violation in nuclear reaction

2.2.1 P-violation in the direct process

The longitudinal asymmetry A_{NN} in the scattering cross section of longitudinal polarized protons irradiating an unpolarized proton target is defined as follows,

$$A_{NN} \equiv \frac{\sigma^{+}_{NN} - \sigma^{-}_{NN}}{\sigma^{+}_{NN} + \sigma^{-}_{NN}}, \tag{2.1}$$

where $\sigma^{\pm}_{NN}$ are the scattering cross sections for helicity positive- and negative- states of incident protons, respectively. As shown in Table 2.1, A_{NN} was measured in various energy regions, and for each result $A_{NN} \sim \mathcal{O}(10^{-7})$ [31–34]. The reactions in these energy regions are dominated by direct processes, which means that P-violation exists in nucleon-nucleon interactions. The probability amplitude f of the nucleon-nucleon interaction consists of the parity conserved (PC) amplitude f_{PC} and the parity nonconserved (PNC) amplitude f_{PNC}, the magnitude of the interaction is given as

$$\begin{aligned} |f|^2 &= |f_{\mathrm{PC}} + f_{\mathrm{PNC}}|^2 \\ &\sim |f_{\mathrm{PC}}|^2 \left(1 + 2\frac{|f_{\mathrm{PNC}}|}{|f_{\mathrm{PC}}|} + \frac{|f_{\mathrm{PNC}}|^2}{|f_{\mathrm{PC}}|^2}\right). \end{aligned} \tag{2.2}$$

Since the weak nucleon-nucleon interaction is considered to be dominated by the one meson exchange process, the ratio of f_{PNC} and f_{PC} is given approximately as the ratio of PNC and PC light meson exchange potential as follows,

$$\begin{aligned} \frac{|f_{\mathrm{PNC}}|}{|f_{\mathrm{PC}}|} &\sim \frac{V_{PNC}}{V_{PC}} \\ &\sim G_F m_\pi^2 \\ &\sim 2 \times 10^{-7}, \end{aligned} \tag{2.3}$$

where G_F and m_π are the Fermi coupling constant and the pion mass, respectively. In this way, the theoretical calculation for P-violation in the direct process can find agreement with experimental values.

2.2.2 P-violation in the compound nuclear process

In the 1980s, large P-violation was observed at the p-wave resonance in compound nuclear reactions by Alfimenkov [35]. Longitudinally polarized neutrons were made to irradiate an unpolarized target causing the neutron spin to flip, and the number of transmitted neutrons were measured. They found that the longitudinal asymmetry $A_{\rm L}$, defined as follows, has a large value only in the vicinity of the p-wave resonance.

$$A_{\rm L} \equiv \frac{\sigma_{p+} - \sigma_{p-}}{\sigma_{p+} + \sigma_{p-}}, \tag{2.4}$$

where $\sigma_{p\pm}$ are the absorption cross sections of the p-wave resonance for helicity positive- and negative- states of incident neutrons. Starting with the discovery of a large P-violation of ^{117}Sn [35], the longitudinal asymmetry was measured in various nuclides and energy regions as shown in Fig.2.1. In particular, ^{139}La was confirmed to have an extremely large asymmetry, $A_{\rm L} \sim \mathcal{O}(10^{-1})$ [36]. The phenomenon that the P-violation, which is approximately 10^{-7} in the direct process, is enhanced to approximately 10^6 in the compound nuclear process is given the following theoretical interpretation [26].

The large P-violation observed in compound nuclear reactions is often observed at a p-wave resonance when the p-wave resonance exists at the tail of the large s-wave resonance as shown in Fig.2.2. In view of these observations, a theoretical interpretation has been given that the P-violation, which was 10^{-7} in the direct process, is enhanced by a factor of 10^6 by the mixing of partial waves with opposite parities in the compound nuclear process. In general, in the case of low energy neutron and nuclear reactions, only the contribution of the lower order partial wave should be considered. Therefore, in the theoretical interpretation, it is called the "sp-mixing" model, since the mixing of the s- and p-wave amplitudes is assumed. The angular momentum of the incident neutron $\boldsymbol{j}$ can be written as

$$\boldsymbol{j} = \boldsymbol{l} + \boldsymbol{s}, \tag{2.5}$$

where $\boldsymbol{l}$ is the orbital angular momentum and $\boldsymbol{s}$ is the spin of the incident neutron, respectively. Since the s- and p-wave correspond to $l = 0$ and 1, respectively, there are states $j = 1/2$ for s-wave resonances and $j = 1/2$ and $j = 3/2$ for p-wave resonances. The neutron width of the

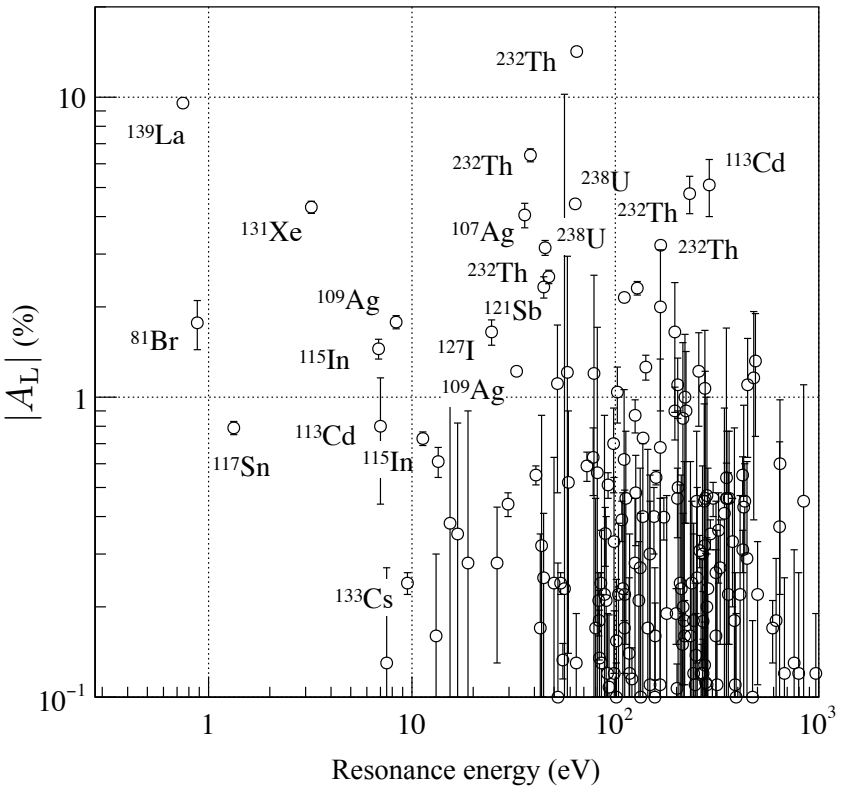

Figure 2.1: Longitudinal asymmetry of various nuclei [37]

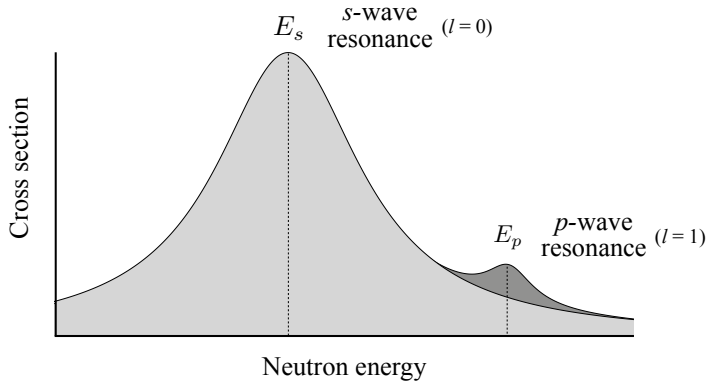

Figure 2.2: Schematic of a p-wave resonance at the tail of a large s-wave resonance. Large P-violation has been observed in p-wave resonance under these conditions.

s- and p-wave resonances Γ^n_s, Γ^n_p have the following relation,

$$\Gamma^n_s = \Gamma^n_{s,j=\frac{1}{2}}, \quad \Gamma^n_p = \Gamma^n_{p,j=\frac{1}{2}} + \Gamma^n_{p,j=\frac{3}{2}}, \tag{2.6}$$

where $\Gamma^n_{s,j=\frac{1}{2}}$, $\Gamma^n_{p,j=\frac{1}{2}}$ and $\Gamma^n_{p,j=\frac{3}{2}}$ are the partial neutron width of $j = 1/2$ for s-wave and $j = 1/2$ and $j = 3/2$ for p-wave resonances, respectively. In this model, the longitudinal asymmetry in Eq.2.4 is described as follows,

$$A_{\rm L} \simeq -\frac{2xW}{E_p - E_s}\sqrt{\frac{\Gamma^n_s}{\Gamma^n_p}}, \tag{2.7}$$

where E_s and E_p are the resonance energies of the s- and p-wave resonances, respectively. The W is the weak matrix element in the transition to the partial wave with opposite parity. The variable x is defined as

$$x \equiv \sqrt{\frac{\Gamma^n_{p,j=\frac{1}{2}}}{\Gamma^n_p}}. \tag{2.8}$$

It is theoretically understood that two types of factors cause the enhancement of P-violation. One is "dynamic enhancement" and the other is "structural enhancement". The "dynamic enhancement" originates from the statistical properties of compound nuclei. The Hamiltonian of the compound state consists of parts of parity conservation $H_{\rm PC}$ and parity non-conservation $H_{\rm PNC}$. The amplitudes $|s'\rangle$ and $|p'\rangle$, which are the mixed amplitudes of partial waves with opposite parity due to the existence of the parity non-conserving process, is expressed as

$$\begin{aligned} |s'\rangle &= |s\rangle - \frac{\langle s\,|H_{\rm PNC}|\,p\rangle}{E_p - E_s}|p\rangle, \\ |p'\rangle &= |p\rangle + \frac{\langle s\,|H_{\rm PNC}|\,p\rangle}{E_p - E_s}|s\rangle, \end{aligned} \tag{2.9}$$

where $|s\rangle$ and $|p\rangle$ are wave functions of s- and p-waves, respectively. The weak matrix element W corresponds to $\langle s\,|H_{\rm PNC}|\,p\rangle$. The s- and p-wave compound states can be expressed as a linear combination of single particle-hole states in a nuclear shell model as

$$|s\rangle = \sum_i^N a_i|\psi_i\rangle, \quad |p\rangle = \sum_j^N b_j|\psi_j\rangle, \tag{2.10}$$

where the coefficients a_i and b_j give the magnitude of each wave function and are of the order of $1/\sqrt{N}$ as a result of the normalization of $|s\rangle$ and $|p\rangle$, respectively, and N is the number of compound states. The average spacing of single particle-hole states is D_0 and the average level spacing of the compound state is D. Therefore, N has the following relationship,

$$N \sim \frac{D_0}{D}. \tag{2.11}$$

The weak matrix element is written using Eq.2.10 as

$$\begin{aligned} |W| &= |\langle s\,|H_{\rm PNC}|\,p\rangle| \\ &= \left|\left\langle \sum_i^N a_i\psi_i\,|H_{\rm PNC}|\sum_j^N b_j\psi_j\right\rangle\right| \\ &= \left|\sum_{i,j}^N a_i^* b_j\,\langle\psi_i\,|H_{\rm PNC}|\,\psi_j\rangle\right|. \end{aligned} \tag{2.12}$$

Assuming that the phases of a_i and b_j are random, $|W|$ is given as

$$|W| \sim \frac{\overline{\langle\psi_i\,|H_{\rm PNC}|\,\psi_j\rangle}}{N}\sqrt{N}. \tag{2.13}$$

Eq.2.7 can then be described as

$$\begin{aligned} \frac{2W}{E_p - E_s} &\sim \frac{|W|}{D} \\ &\sim \frac{\overline{\langle\psi_i\,|H_{\rm PNC}|\,\psi_j\rangle}}{D_0}\sqrt{N} \\ &\sim F\sqrt{N}, \end{aligned} \tag{2.14}$$

where F is the size of the parity mixing in the single particle-hole state and has the same order of magnitude as the P-violation in the direct process. The typical values in Eq.2.11 are $D_0 \sim 10^6$ eV and $D \sim 10$ eV, therefore $N \sim 10^5$, and the size of the P-violation in the direct process is approximately 10^{-7} from Eq.2.3. Therefore, the "dynamical enhancement" is approximately 10^2 – 10^3. The other enhancement factor, "structural enhancement," is caused by the different centrifugal barriers of neutron waves, and the neutron widths for the s- and p-wave are written as

$$\Gamma_s^n \propto kR, \quad \Gamma_p^n \propto (kR)^3, \tag{2.15}$$

where k is the neutron momentum and R is the radius of the nucleus. Therefore the "structural enhancement" is given as

$$\sqrt{\frac{\Gamma_s^n}{\Gamma_p^n}} \sim \frac{1}{kR}. \tag{2.16}$$

Since typical values of $R \sim 10$ fm and $k \sim 10^{-4}$ fm^{-1}, the amplitude of the "structural enhancement" is approximately 10^3. Thus, it is understood that the P-violation in the direct process is enhanced 10^6 times by two types of enhancement factors. On the other hand, the

parameter x in Eq.2.8 is estimated to be of the order of 1 and can be determined by measuring the angular distribution of the (n, γ) reaction.

2.3 T-violation in nuclear reactions

2.3.1 Enhancement of the T-violation in the compound nuclear process

It has been pointed out by Gudkov that CP-violation can also be enhanced when the enhancement mechanism of P-violation based on the *sp*-mixing model in the compound nuclear process is expanded [27]. Since CP-violation is equivalent to T-violation via the CPT theorem, it can be observed as a T-violating cross section experimentally. The wave function $|lsI\rangle$ is transformed by parity inversion as

$$P : |lsI\rangle \rightarrow (-1)^l |lsI\rangle. \tag{2.17}$$

In the case of a time reversal transformation, it changes as follows,

$$T : |lsI\rangle \rightarrow (-1)^{i\pi S_y} \hat{K} |lsI\rangle, \tag{2.18}$$

where $\boldsymbol{I}$ is the target nuclear spin, $\boldsymbol{S}$ is the channel spin, which is defined as $\boldsymbol{S} = \boldsymbol{s} + \boldsymbol{I}$ and $\hat{K}$ is an operator that gives complex conjugation. Enhancement of T-violation is caused by mixing of different channel spin. We then consider the recombination of the angular momentum as follows,

$$\begin{aligned} |((Is)S, l)J\rangle &= \sum_j \langle (I, (sl)j)J \mid ((Is)S, l)J\rangle |(I, (sl)j)J\rangle \\ &= \sum_j (-1)^{1+I+\frac{1}{2}+J} \sqrt{(2j+1)(2S+1)} \begin{Bmatrix} 1 & \frac{1}{2} & j \\ I & J & S \end{Bmatrix} |((ls)j, I)J\rangle, \end{aligned} \tag{2.19}$$

where $\boldsymbol{J} = \boldsymbol{s} + \boldsymbol{I} + \boldsymbol{l}$ is the spin of the compound nuclear state. This recombination produces the following relationship between T- and P-violation as follows,

$$\Delta\sigma_{\mathrm{T}} = \kappa(J) \frac{W_{\mathrm{T}}}{W} \Delta\sigma_{\mathrm{P}}, \tag{2.20}$$

where the spin factor $\kappa(J)$ is a coefficient representing the change in the combination of angular momentum, $\Delta\sigma_{\mathrm{T}}$ and $\Delta\sigma_{\mathrm{P}}$ are T- and P-violating cross section in the compound nuclear reaction, and W_{T} and W are the T- and P-violating weak matrix elements. The spin factor

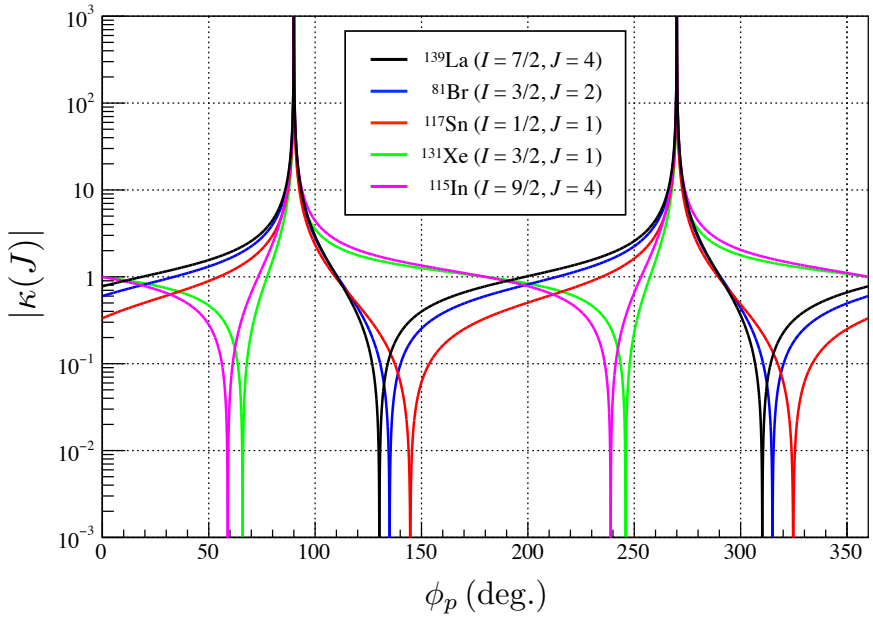

Figure 2.3: ϕ_p dependence of $|\kappa(J)|$ for various nuclei.

$\kappa(J)$ can be described in terms of the target nuclear spin I as

$$\kappa(J) = \begin{cases} (-1)^{2I}\left(1 + \frac{1}{2}\sqrt{\frac{2I-1}{I+1}}\frac{y}{x}\right) & \left(J = I - \frac{1}{2}\right) \\ (-1)^{2I+1}\frac{I}{I+1}\left(1 - \frac{1}{2}\sqrt{\frac{2I+3}{I}}\frac{y}{x}\right) & \left(J = I + \frac{1}{2}\right) \end{cases}, \tag{2.21}$$

where x and y can be written in terms of the $j = 1/2$ and $j = 3/2$ components of the partial neutron width of the p-wave resonance as

$$x \equiv \sqrt{\frac{\Gamma^n_{p,j=\frac{1}{2}}}{\Gamma^n_p}}, \quad y \equiv \sqrt{\frac{\Gamma^n_{p,j=\frac{3}{2}}}{\Gamma^n_p}}, \tag{2.22}$$

where x and y satisfy the following relationship from Eq.2.6

$$x^2 + y^2 = 1. \tag{2.23}$$

Since the above relation represents a unit circle in the xy plane, the mixing angle ϕ_p can be defined as

$$x = \cos\phi_p, \quad y = \sin\phi_p. \tag{2.24}$$

Fig.2.3 shows the ϕ_p dependence of $\kappa(J)$ for various nuclei. Since the value of $\kappa(J)$ determines the experimental sensitivity of the T-violation search, its determination is crucial.

2.3.2 Experimental concept of the T-violation search

The forward scattering amplitude in the reaction of low energy neutrons with a polarized nuclear target with only vector polarization can be described as follows,

$$f = A' + B'\boldsymbol{\sigma}\cdot\hat{\boldsymbol{I}} + C'\boldsymbol{\sigma}\cdot\hat{\boldsymbol{k}} + D'\boldsymbol{\sigma}\cdot(\hat{\boldsymbol{I}}\times\hat{\boldsymbol{k}}), \tag{2.25}$$

where $\boldsymbol{\sigma}$, $\hat{\boldsymbol{I}}$, and $\hat{\boldsymbol{k}}$ are the incident neutron spin, nuclear target spin and the unit vector parallel to neutron momentum, respectively. When the propagation of neutrons through a target of finite thickness can be treated optically, the following relationship is given between the initial state spinor U_i and the final state spinor U_f,

$$\begin{aligned} U_f &= \mathfrak{S}U_i, \\ \mathfrak{S} &= e^{i(n-1)kz}, \\ n &= 1 + \frac{2\pi\rho}{k^2}f, \end{aligned} \tag{2.26}$$

where k is the wave number of neutrons, z is the thickness of the target and ρ is the number density of the target nucleus. A density matrix $\mathfrak{S}$ is given as

$$\mathfrak{S} = A + B\boldsymbol{\sigma}\cdot\hat{\boldsymbol{I}} + C\boldsymbol{\sigma}\cdot\hat{\boldsymbol{k}} + D\boldsymbol{\sigma}\cdot(\hat{\boldsymbol{I}}\times\hat{\boldsymbol{k}}), \tag{2.27}$$

where

$$\begin{aligned} A &= e^{iZA'}\cos b, \\ B &= e^{iZA'}\frac{\sin b}{b}ZB', \\ C &= e^{iZA'}\frac{\sin b}{b}ZC', \\ D &= e^{iZA'}\frac{\sin b}{b}ZD', \\ Z &= \frac{2\pi\rho z}{k}, \\ b &= Z\sqrt{B'^2 + C'^2 + D'^2}, \end{aligned} \tag{2.28}$$

where the A term is the coherent scattering amplitude, B is the incoherent scattering amplitude, C is the P-odd and T-even scattering amplitude and D is the P-odd and T-odd scattering amplitude. The D term is the T-violating term. Therefore, by experimentally confirming that the D term has a non-zero value, the discovery of T-violation may be confirmed. As an example of a measurement of the D term, as shown in Fig.2.4, polarized neutrons are injected in the direction of z-axis, and neutrons are polarized in the direction of x-axis and target is polarized

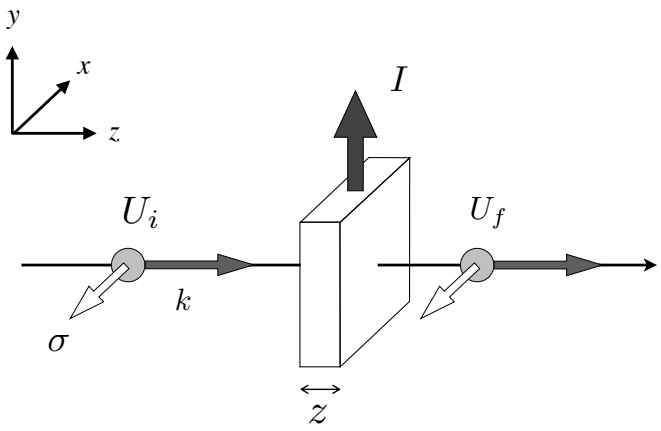

Figure 2.4: Basic concept of the T-violation search. Measurement of the D term with polarized neutrons and polarized target.

in the direction of y-axis. Then, if D has a finite value, additional neutron spin rotations other than the contributions of the A, B, and C terms occur in the xy-plane in the polarized target. Therefore, the following four observables are considered. One is the analyzing power A_x, i.e., the transmittance when polarized neutrons are injected. The second is the polarization of transmitted neutrons P_x when unpolarized neutrons are injected. Finally, the polarization transfer coefficient K^{+x}_{+x}, K^{-x}_{-x} in the target when polarized neutrons were injected. Each of them has the following relation as observables including the D term,

$$A_x \equiv \frac{\mathrm{Tr}\left(\sigma_x \mathfrak{S}^\dagger \mathfrak{S}\right)}{\mathrm{Tr}\left(\mathfrak{S}^\dagger \mathfrak{S}\right)} = 4\left(\frac{\mathrm{Re}\, A^* D}{|A|^2} + \frac{\mathrm{Im}\, B^* C}{|A|^2}\right), \tag{2.29}$$

$$P_x \equiv \frac{\mathrm{Tr}\left(\mathfrak{S}^\dagger \sigma_x \mathfrak{S}\right)}{\mathrm{Tr}\left(\mathfrak{S}^\dagger \mathfrak{S}\right)} = 4\left(\frac{\mathrm{Re}\, A^* D}{|A|^2} - \frac{\mathrm{Im}\, B^* C}{|A|^2}\right), \tag{2.30}$$

$$\begin{aligned} K^{+x}_{+x} &\equiv \frac{\mathrm{Tr}\left(\frac{1+\sigma_x}{2} \mathfrak{S}^\dagger \frac{1+\sigma_x}{2} \mathfrak{S}\right)}{\mathrm{Tr}\left(\mathfrak{S}^\dagger \mathfrak{S}\right)} = \frac{|A|^2 + 2\,\mathrm{Re}\, A^* D + |D|^2}{|A|^2}, \\ K^{-x}_{-x} &\equiv \frac{\mathrm{Tr}\left(\frac{1-\sigma_x}{2} \mathfrak{S}^\dagger \frac{1-\sigma_x}{2} \mathfrak{S}\right)}{\mathrm{Tr}\left(\mathfrak{S}^\dagger \mathfrak{S}\right)} = \frac{|A|^2 - 2\,\mathrm{Re}\, A^* D + |D|^2}{|A|^2}. \end{aligned} \tag{2.31}$$

By combining these observables, the terms proportional to D can be extracted. For example, as shown in Fig.2.5, the summation of A_x and P_x gives $8\,\mathrm{Re}\, A^* D/|A|^2$, or the subtraction of K^{+x}_{+x} and K^{-x}_{-x} gives $4\,\mathrm{Re}\, A^* D/|A|^2$. In Eq.2.20, W_T/W is given an upper limit by a measurement of the neutron EDM and ^{199}Hg and the $\vec{n}p$ measurement [38], $\Delta\sigma_\mathrm{P}$ is determined from the measurement of longitudinal asymmetry A_L, and $\Delta\sigma_\mathrm{T}$ is proportional to the D term. It follows that the sensitivity for a T-violation search in compound nuclei can be estimated by determining the spin factor $\kappa(J)$.

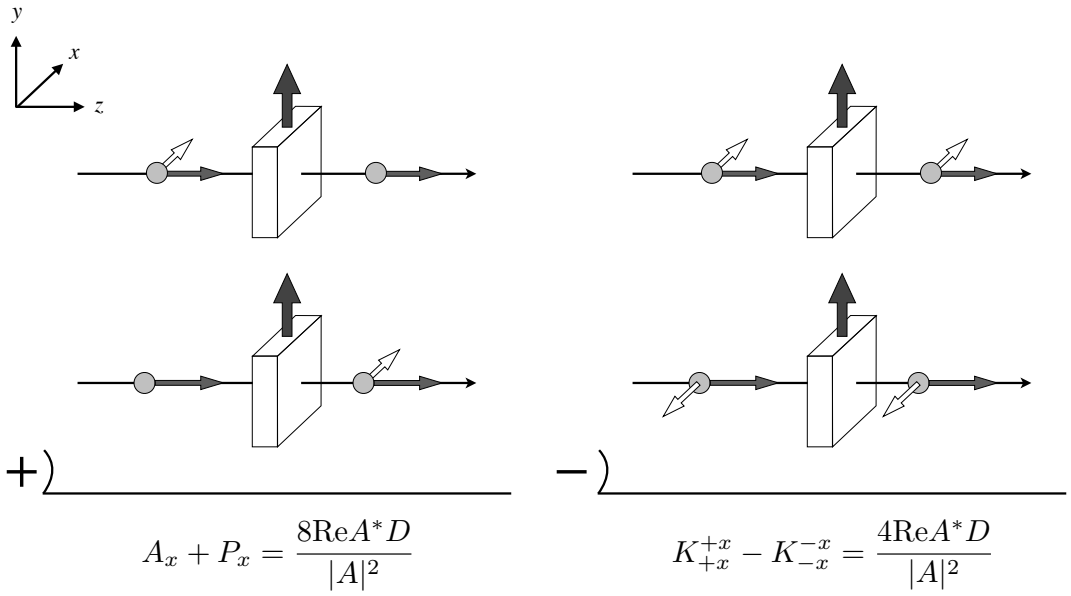

Figure 2.5: Examples of combinations for observables in T-violation search. The left figure shows a combination of analyzing power and polarization measurements. The right figure shows the polarization transitions are measured and subtracted.

2.3.3 Final State Interactions in Neutron Optics

Decay and scattering processes of particles transitioning from the initial state i to the final state f are discussed. If the reaction matrix proportional to the scattering amplitude is defined as T, the condition that the scattering matrix is unitary is given as

$$T^\dagger - T = iTT^\dagger. \tag{2.32}$$

If we assume the first-order Born approximation, the right side is negligibly small so that the T is hermitian ($T^\dagger = T$). Therefore, the following relationship is obtained,

$$\langle i|T|f\rangle = \langle i\,|T^*|\,f\rangle\,. \tag{2.33}$$

Using the time reversal invariance relation, the following equation is given as

$$\langle f|T|i\rangle = \langle -i|T|-f\rangle^*. \tag{2.34}$$

The Hermiticity of T, that is, the Eq.2.34 is modified by using Eq.2.33 to give the following equation,

$$|\langle f|T|i\rangle|^2 = |\langle -f|T|-i\rangle|^2. \tag{2.35}$$

Therefore, if the reaction process can be represented by the first-order Born approximation, A T-violation search can be performed by measuring the T-odd term. However, when the first-order Born approximation cannot be applied, i.e., when the right side of Eq.2.32 cannot be ignored and the T matrix has no hermiticity, Eq.2.33 is not satisfied. Therefore, false T-violation occurs in the measurement of the T-odd term, which is called FSI. In general, the search for T-violation via a measurement of a T-odd term is often limited in sensitivity by the FSI. However, the forward scattering process in the framework of neutron optics does not involve the FSI because it does not change the state. Therefore, the attractive feature of this method is that it is FSI-free, and it is easy to improve sensitivity from a statistical viewpoint.

2.3.4 Candidate nuclei for the T-violation search

It is necessary to select an optimal nuclide used for the T-violation search as this search strongly reflects the nature of the nucleus used, and each has its advantages. Therefore, it is important to evaluate and determine these comprehensively. The primary requirement is a large $\Delta\sigma_{\mathrm{T}}$. For this purpose, it is necessary to estimate the magnitude of $\Delta\sigma_{\mathrm{T}}$ by measuring $\Delta\sigma_{\mathrm{P}}$ and $\kappa(J)$ for each nuclide. As for $\Delta\sigma_{\mathrm{P}}$, as shown in Fig.2.1, many nuclides have been studied in advance, and it is reasonable to determine $\kappa(J)$ of those nuclides. On the other hand, experimental constraints need to be considered. The effect of T-violation is observed at the p-wave resonance. It is necessary to consider the characteristics of the neutron intensity of the neutron source because it has different resonance energies depending on the nuclide. In general, the neutron intensity increases with decreasing energy due to the neutron moderation process. Therefore, nuclides with low p-wave resonance energy are desirable from the statistical point of view. And, it is also necessary to consider the nuclear polarization method, because the observable quantity in the T-violation search is proportional to the nuclear polarization. Fundamentally, it is possible to polarize any nucleus, if the Bruteforce (BF) method using the fact that the nuclear spin follows the Boltzmann distribution under high magnetic field and very low temperature is used. However, the BF method requires a long time to achieve high polarization because of their very long relaxation time (months to a year). Therefore, nuclides for which Dynamic nuclear polarization (DNP) method [39] has been established are desirable from the viewpoint of obtaining high polarization. Candidate nuclei for the T-violation search are listed in Table 2.2. The $\kappa(J)$ measurements of these nuclides are in progress in parallel [40, 41]. Among them, ^{139}La with large A_{L} was found to have $\kappa(J)$ of the order of 1. In addition, polarization of lanthanum can get close to 50% by applying the DNP method to single crystal $LaAlO_3$ doped with Nb [42]. Therefore, ^{139}La is one of the most promising nuclides at present.

Table 2.2: Candidate nuclei for the T-violation search. The nuclides are listed in order of decreasing energy for p-wave resonance.

Nuclide	E_p (eV)	A_{L} (%)	I	Natural abundance (%)	Polarization method
^{139}La	0.74	9.8 ± 0.2	7/2	99.9	DNP [42]
^{81}Br	0.88	1.77 ± 0.33	3/2	49.3	SEOP[1] [43]
^{117}Sn	1.33	0.79 ± 0.04	1/2	8.6	DNP [44]
^{131}Xe	3.2	4.3 ± 0.2	3/2	21.2	SEOP[1] [45]
^{115}In	6.85	-1.45 ± 0.11	9/2	95.7	DNP [46]

However, two different values are given from the restriction on the value of ϕ_p and $\kappa(J)$ for ^{139}La in previous studies as shown in Fig.2.6 and 2.7 [30], and the experimental sensitivity of the T-violation search remains uncertain. Therefore, it is desired to limit the experimental sensitivity of the T-violation search to one value of ϕ_p and $\kappa(J)$ of ^{139}La by upgrading the (n, γ) measurement.

2.4 The angular distribution in (n, γ) reaction

Determining the value of ϕ_p and $\kappa(J)$ is important for estimating the sensitivity of the T-violation search. These values can be determined by measuring the correlation term in the

[1] discussed in detail in chapter 3.

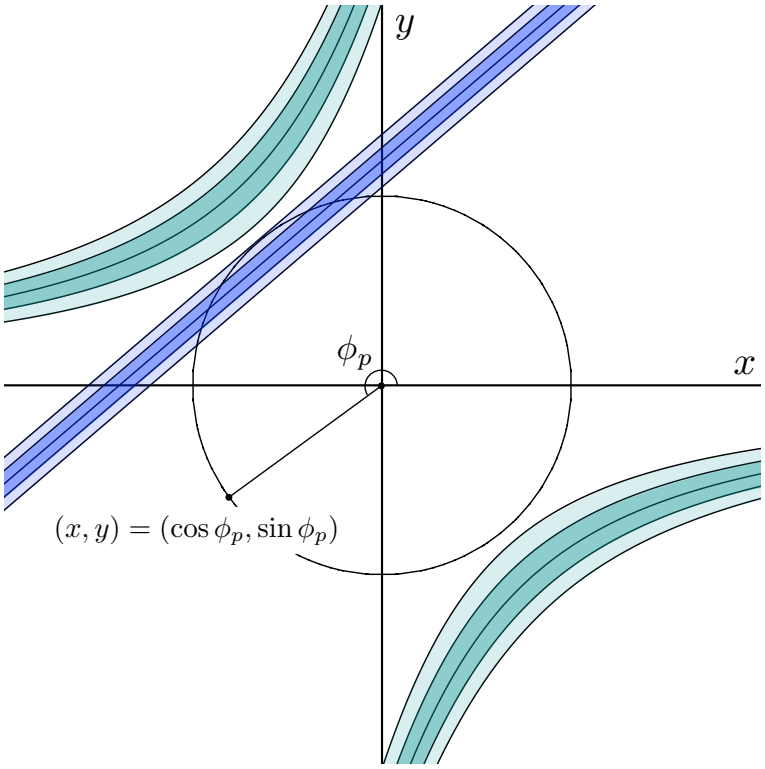

Figure 2.6: The restricted regions of ϕ_p was determined by measuring the angular distribution of the ^{139}La(n, γ) reaction with unpolarized neutrons [30]. Blue and green regions represent the a_1 and a_3 terms, respectively. The dark color region represents the 1σ region, and the light color region represents the 2σ region.

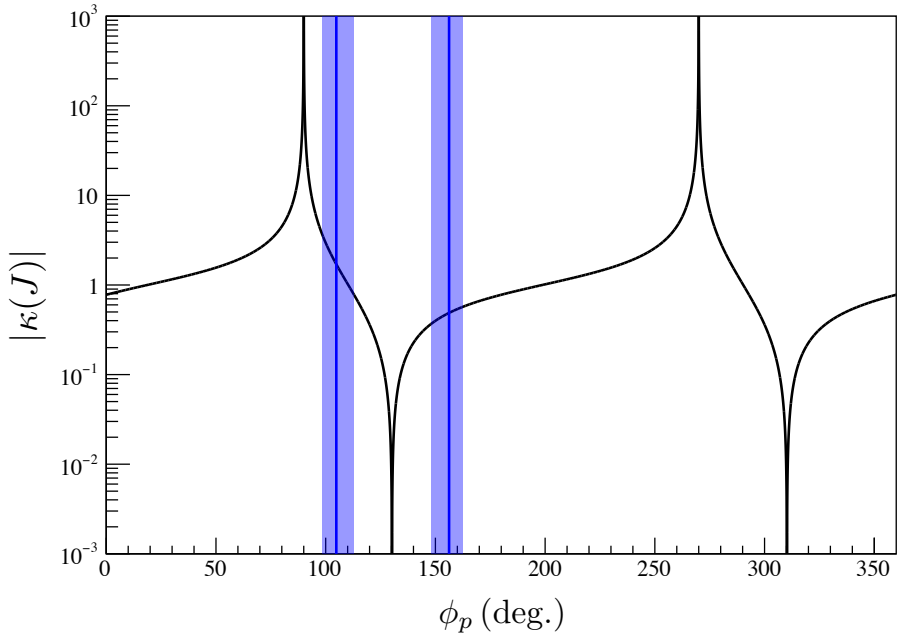

Figure 2.7: The restricted regions of $\kappa(J)$ for ^{139}La was determined by measuring the angular distribution of the ^{139}La(n, γ) reaction with unpolarized neutrons [30].

(n,γ) reaction. The differential cross section of the (n,γ) reaction can be written as [47]

$$\begin{aligned}\frac{\mathrm{d}\sigma_{n\gamma_f}}{\mathrm{d}\Omega_\gamma} = \frac{1}{2}\Bigg(& a_0 + a_1\hat{k}_n\cdot\hat{k}_\gamma + a_2\sigma_n\cdot\left(\hat{k}_n\times\hat{k}_\gamma\right) + a_3\left(\left(\hat{k}_n\cdot\hat{k}_\gamma\right)^2 - \frac{1}{3}\right)\\ &+ a_4\left(\hat{k}_n\cdot\hat{k}_\gamma\right)\left(\sigma_n\cdot\left(\hat{k}_n\times\hat{k}_\gamma\right)\right) + a_5\left(\sigma_\gamma\cdot\hat{k}_\gamma\right)\left(\sigma_n\cdot\hat{k}_\gamma\right)\\ &+ a_6\left(\sigma_\gamma\cdot\hat{k}_\gamma\right)\left(\sigma_n\cdot\hat{k}_n\right) + a_7\left(\sigma_\gamma\cdot\hat{k}_\gamma\right)\left(\left(\sigma_n\cdot\hat{k}_\gamma\right)\left(\hat{k}_\gamma\cdot\hat{k}_n\right) - \frac{1}{3}\sigma_n\cdot\hat{k}_n\right)\\ &+ a_8\left(\sigma_\gamma\cdot\hat{k}_\gamma\right)\left(\left(\sigma_n\cdot\hat{k}_n\right)\left(\hat{k}_n\cdot\hat{k}_\gamma\right) - \frac{1}{3}\sigma_n\cdot\hat{k}_\gamma\right)\\ &+ a_9\sigma_n\cdot\hat{k}_\gamma + a_{10}\sigma_n\cdot\hat{k}_n + a_{11}\left(\left(\sigma_n\cdot\hat{k}_\gamma\right)\left(\hat{k}_\gamma\cdot\hat{k}_n\right) - \frac{1}{3}\left(\sigma_n\cdot\hat{k}_n\right)\right)\\ &+ a_{12}\left(\sigma_n\cdot\hat{k}_n\right)\left(\left(\hat{k}_n\cdot\hat{k}_\gamma\right) - \frac{1}{3}\left(\sigma_n\cdot\hat{k}_\gamma\right)\right)\\ &+ a_{13}\sigma_\gamma\cdot\hat{k}_\gamma + a_{14}\left(\sigma_\gamma\cdot\hat{k}_\gamma\right)\left(\hat{k}_n\cdot\hat{k}_\gamma\right)\\ &+ a_{15}\left(\sigma_\gamma\cdot\hat{k}_\gamma\right)\sigma_n\cdot\left(\hat{k}_n\times\hat{k}_\gamma\right) + a_{16}\left(\sigma_\gamma\cdot\hat{k}_\gamma\right)\left(\left(\hat{k}_n\cdot\hat{k}_\gamma\right)^2 - \frac{1}{3}\right)\\ &+ a_{17}\left(\sigma_\gamma\cdot\hat{k}_\gamma\right)\left(\hat{k}_n\cdot\hat{k}_\gamma\right)\left(\sigma_n\cdot\left(\hat{k}_n\times\hat{k}_\gamma\right)\right)\Bigg),\end{aligned} \tag{2.36}$$

where $\hat{k}_n$ and $\hat{k}_\gamma$ are units vectors parallel to momenta of neutron and γ-ray, σ_n and σ_γ are the neutron and γ-ray spins, respectively (See Appendix A for a detailed expression of the correlation term). When incident neutrons are unpolarized and the γ-ray circular polarization is not measured, Eq.2.36 can be described as

$$\frac{\mathrm{d}\sigma_{n\gamma_f}(\theta)}{\mathrm{d}\Omega_\gamma} = \frac{1}{2}\left(a_0 + a_1\cos\theta + a_3\left(\cos^2\theta - \frac{1}{3}\right)\right), \tag{2.37}$$

where θ is the polar angle of the emitted γ rays with respect to the incident neutron momentum as shown in Fig.2.8. The a_1 and a_3 terms have an angular distribution which can be expanded in terms of x and y as

$$\begin{aligned} a_1 &= a_{1x}x + a_{1y}y,\\ a_3 &= a_{3xy}xy + a_{3yy}y^2. \end{aligned} \tag{2.38}$$

The theoretical calculation for x and y for ^{139}La were determined by measuring the angular distribution using unpolarized neutrons. In previous studies, ϕ_p was determined from the results of a_1 and a_3 terms. Additionally, when incident neutrons are polarized perpendicular to the incident direction as shown in Fig.2.8 and the circular polarization of the γ-rays is not measured,

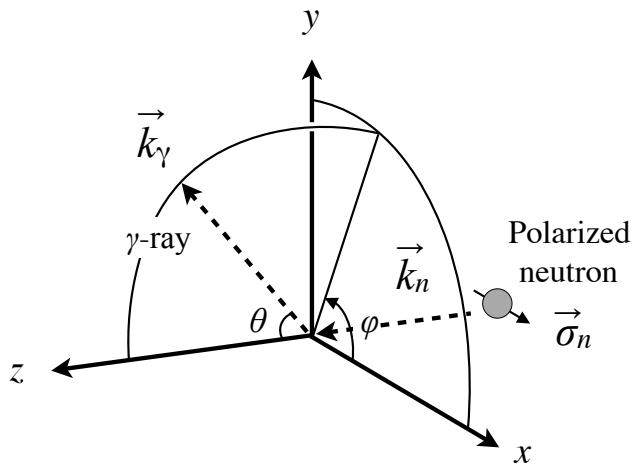

Figure 2.8: Definition of coordinate systems and vector elements. The z axis is defined in the beam direction, the y axis is the vertical upward axis, the x axis is perpendicular to them. The polar angle in the spherical coordinate is denoted by θ and the azimuthal angle is φ.

Eq.2.36 can be described as

$$\begin{aligned}\frac{d\sigma^{\pm}_{n\gamma}(\theta,\varphi)}{d\Omega} = \frac{1}{2}\Bigg(a_0 + a_1\cos\theta + a_3\left(\cos^2\theta - \frac{1}{3}\right) \\ \pm\Big(-a_2\sin\theta\sin\varphi - a_4\sin\theta\cos\theta\sin\varphi \\ + a_9\sin\theta\cos\varphi + a_{11}\sin\theta\cos\theta\cos\varphi\Big)\Bigg),\end{aligned} \tag{2.39}$$

where φ is the azimuthal angle. In particular, the a_2 term is important because its amplitude is predicted to be large given the value of ϕ_p in previous studies. The a_2 term can also be expanded in terms with x and y dependencies as

$$a_2 = a_{2x}x + a_{2y}y, \tag{2.40}$$

where

$$\begin{aligned}a_{2x} &= -2\,\mathrm{Im}\sum_{r_s r_p} V_{1r_s}V^*_{2r_p}\beta_{\frac{1}{2}}P\left(J_{r_s}J_{r_p}\frac{1}{2}\frac{1}{2}1IF\right), \\ a_{2y} &= -2\,\mathrm{Im}\sum_{r_s r_p} V_{1r_s}V^*_{2r_p}\beta_{\frac{3}{2}}P\left(J_{r_s}J_{r_p}\frac{1}{2}\frac{3}{2}1IF\right),\end{aligned} \tag{2.41}$$

where J_{r_s}, J_{r_p} are the spin of the compound states for s- and p-wave resonances, respectively. Variable I is the spin of the target nucleus and F is the spin of the final state. Therefore, the

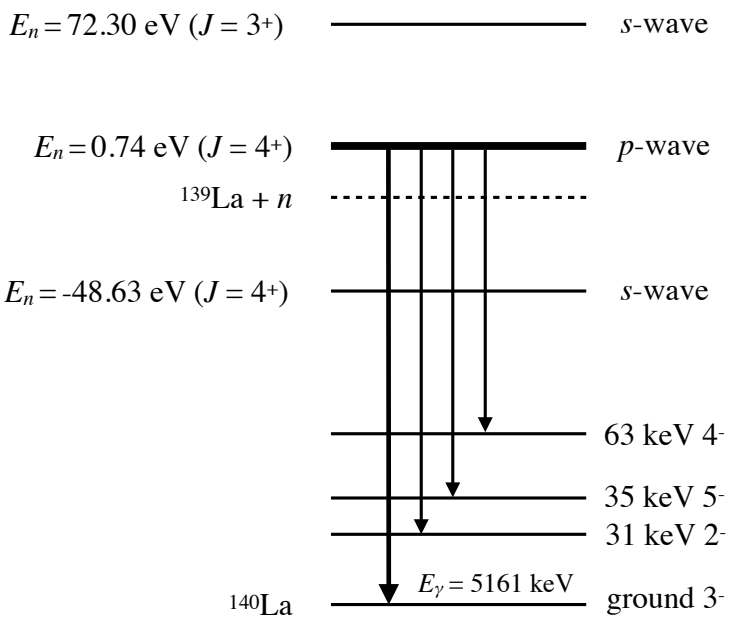

Figure 2.9: Transition scheme for neutron capture of ^{139}La. The scheme does not depict transitions from the s-wave resonance or other higher excited state [48].

value of a_2 depends on these variables, and it is required that the final state can be separated precisely and that the neutron resonance energy can be specified in the measurement. The state transition during the excitation and decay of compound nuclei for ^{139}La is shown in Fig.2.9. In this study, the author focused on the process in which ^{139}La absorbs neutrons, forms a p-wave resonance, and then transitions to the ground state. Figure 2.10 shows the energy dependence of the cross sections for a_{2x} and a_{2y} terms in the vicinity of the p-wave resonance for the case of $F = 3$ and the value of J was used from table.2.3. Therefore, by determining the amplitude of a_2 experimentally, the value of x, y, and ϕ_p are determined.

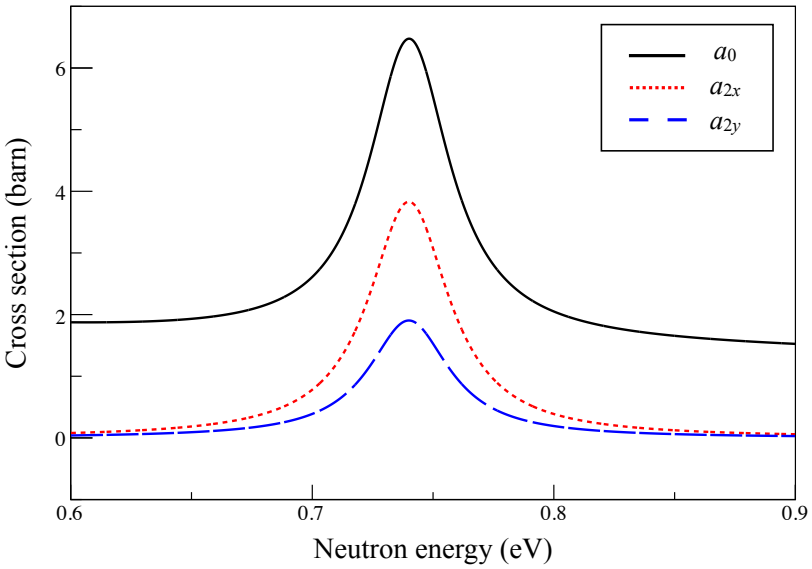

Figure 2.10: Energy dependence of the cross sections for a_{2x} and a_{2y} terms in the vicinity of the p-wave resonance for the case of $F = 3$, $J_{s_1} = 4$, $J_p = 4$, and $J_{s_2} = 3$. The a_0 term represents the uncorrelated absorption cross section of the (n, γ) reaction. The presence of a_2 changes the resonance amplitude.

Table 2.3: Resonance parameters of ^{139}La used in the analysis. r is the type of partial wave, E_r is the resonance energy, J_r is the spin of compound state, l_r is the orbital angular momentum of the incident neutron, Γ_r^γ is the partial γ width, $g_r = (2J_r + 1) / [2(2I + 1)]$ is the statistical factor and Γ_r^n is the neutron width.

r	E_r (eV)	J_r	l_r	Γ_r^γ (meV)	$g_r\Gamma_r^n$ (meV)
s_1	-48.63^a	4^a	0	62.2^a	$(571.8)^a$
p	0.740 ± 0.002^b	4	1	40.41 ± 0.76^b	$(5.6 \pm 0.5) \times 10^{-5\,c}$
s_2	72.30 ± 0.05^c	3	0	75.64 ± 2.21^c	11.76 ± 0.53^c

[a] Taken from Ref.[49, 50].
[b] Taken from Ref.[30, 51].
[c] Taken from Ref.[52].

Chapter 3

Experimental Procedure

The experiment was performed at beamline 04, Accurate Neutron-Nucleus Reaction measurement Instrument (BL04 ANNRI), of the Materials and Life science experimental Facility (MLF) of the Japan Proton Accelerator Research Complex (J-PARC). Facilities and equipment are described in the following sections.

3.1 J-PARC MLF

J-PARC located in Tokai, Ibaraki, Japan, uses high intensity proton beams to carry out cutting-edge research in a wide range of fields such as elementary particle physics, nuclear physics, materials science, life science, and nuclear engineering. As shown in Fig.3.1, J-PARC has three accelerators and three experimental facilities. There are a linear accelerator (LINAC), a 3 GeV Rapid-Cycling Synchrotron (RCS) and a 50 GeV Synchrotron (MR) as accelerators, and the Material an Life Science Experimental Facility (MLF), the Neutrino Facility, and the Hadron Experimental Facility as experimental facilities [53]. MLF is an experimental facility for material and life science using high intense pulsed neutrons and muons beams. The protons accelerated to 3 GeV by the RCS are injected into the mercury target at MLF at 25 Hz and cause a spallation reaction to generate neutrons.

As shown in Table 3.1, the incident proton beam from the RCS has a width of 150 ns with an interval of 600 ns (double bunch), and the average proton beam power was 530 kW or 600 kW during measurements. The high energy neutrons generated by the spallation reaction are moderated by a light water moderator and a supercritical hydrogen moderator at 20 K and 1.5 MPa. In order to collect neutrons efficiently into moderators, beryllium is placed as a neutron reflector around moderators, which amplifies the neutron intensity by approximately a factor of 10. A neutron absorber (Decoupler) is inserted between the moderator and the

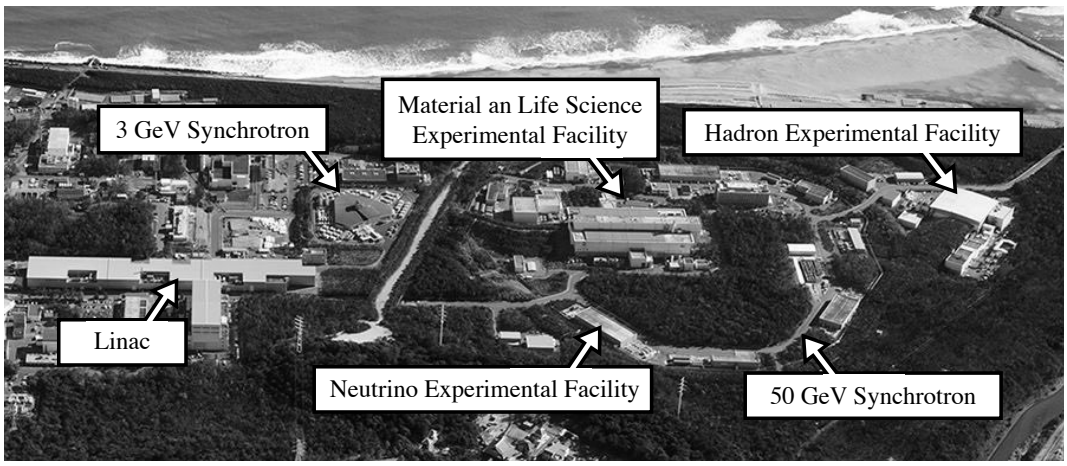

Figure 3.1: Bird's-eye view of J-PARC accelerators.

Table 3.1: Characteristics of the proton beam of RCS [53].

Parameter	Value
Perimeter	348 m
Designed beam power	1 MW
Extraction energy	3 GeV
Repetition rate	25 Hz
Bunch width (double bunch)	100 ns

neutron reflector to suppress the broadening of the pulse width in the moderator. In addition, in order to improve the time structure characteristics of the neutron beam, a plate of cadmium or gadolinium is inserted into the moderator as a neutron absorber (Poison). In MLF, three types of moderators: Coupled, Decoupled and Poison moderators, are used according to the pulse characteristics required for each beam line as shown in Fig.3.2. The beam line used in this study utilizes neutrons supplied from the coupled moderator. Couple moderators have a wider neutron pulse width than those of other moderators because no decoupler is inserted, however they have the highest neutron intensity as shown in Table 3.2.

3.1.1 BL04 ANNRI

BL04 ANNRI was designed and constructed for the purpose of high-precision measurements of neutron reaction cross sections of minor actinides and fission products required for the development of innovative nuclear systems.

As shown in Fig.3.3, BL04 is a beam line of approximately 30 m in total length, and surrounded with a concrete biological shield. The neutron beam was collimated to a 15-mm-

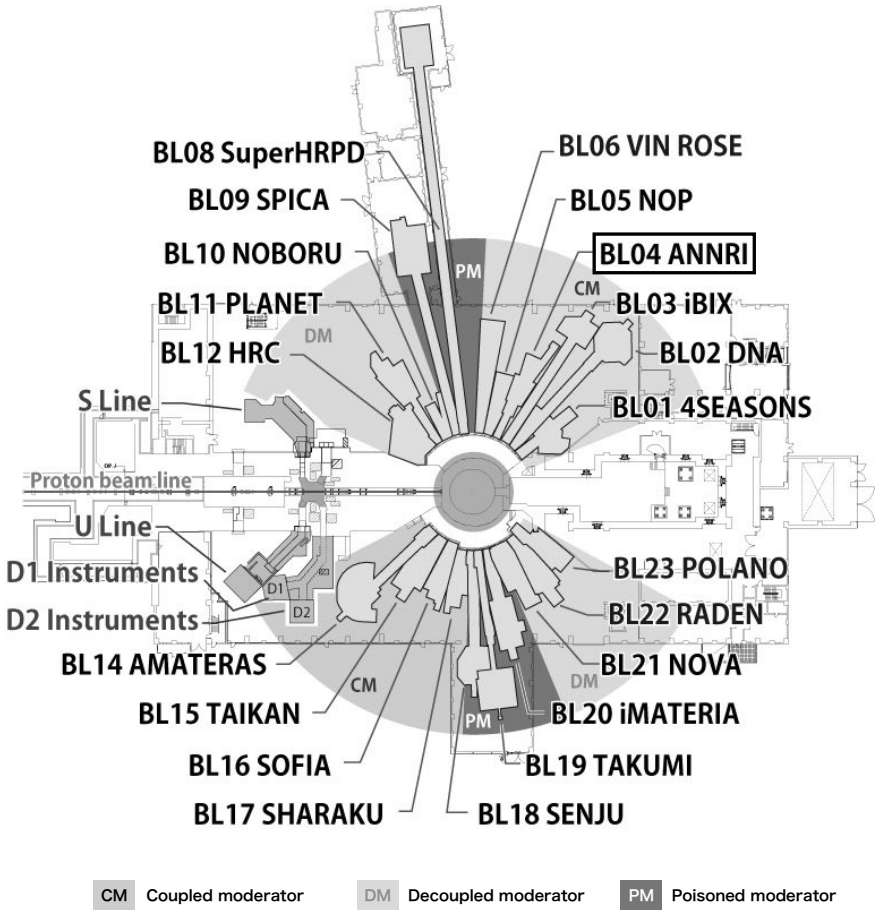

Figure 3.2: Top-view of MLF facility in J-PARC [53].

Table 3.2: Design characteristics of the moderators of MLF at J-PARC [53].

Type of moderators	Time-integrated thermal neutron flux ($n/s \cdot cm^2$)	Peak neutron flux at 10 meV ($n/eV \cdot s \cdot cm^2$)	Pulse width in FWHM at 10 meV (μs)
Coupled	4.6×10^8	6.0×10^{12}	92
Decoupled	0.95×10^8	3.0×10^{12}	33
Poisoned (thicker side)	0.65×10^8	2.4×10^{12}	22
Poisoned (thinner side)	0.38×10^8	1.4×10^{12}	14

diameter spot at the target position, placed 21.5 m from the moderator surface [54]. The lead filter (37.5 mm-thick in total) was installed to suppress the background caused by fast neutrons and γ flashes. The disk choppers operated in synchronization with the timing of the proton beam incidence to avoid frame overlap due to low-energy neutrons. In this study, a ^{3}He spin filter as a neutron polarizer was installed 1.5 m upstream from the target. The germanium detector assembly was arranged surrounding the target to detect the γ rays from the (n, γ) reaction. Neutrons passing through the target were detected by neutron detector located 27.9 m from the moderator through a downstream collimator. To avoid saturation of the neutron detector, a 10 μm-thick gadolinium foil was placed 3 m upstream from the neutron detector. Almost all regions from the moderator to the beam stopper were evacuated to reduce the background due to neutron scattering with atmosphere.

3.2 Experimental apparatus

3.2.1 γ-ray detectors

The germanium detector assembly shown in Fig.3.4 was used to detect the γ rays emitted from the target [55]. A right handed system is used in this thesis as shown in Fig.2.8, and the neutron beam direction is defined to be along the z axis.

The germanium detector assembly consists of two kinds of detectors. One is an "A-type detector", located above and below the target. Each A-type detector has seven separated germanium crystal regions. The other is called a "B-type detector", which consists of eight germanium crystals surrounding the target. The shape of the germanium crystals of the A-type and B-type detectors are cylindrical with a diameter of 70 mm and a height of 78 mm and a diameter of 70 mm and a height of 89 mm, respectively. Germanium crystals are protected by neutron shields such as lithium fluoride (LiF) and lithium hydride (LiH) to prevent lattice defects due to scattered neutrons and to reduce the background caused by (n, γ) reactions other than the sample. In addition, to protect fast neutrons and γ rays, the whole germanium detector assembly is covered with a shield consisting of iron, a boron compound and lead. The nuclear target is placed at the center of the beam duct through the center of the detector. The beam duct is made of aluminum (A5052) and the inside wall is covered with LiF plates. The beam duct is evacuated ($\sim 10^{-1}$ Pa) to prevent scattering of neutrons by atmosphere.

During the experiment, germanium crystals were cooled to 77 K by either liquid nitrogen or a mechanical refrigerator. The energy threshold level for γ-ray detection was set at approximately 100 keV in order to avoid electronic noise. Typical energy resolution is 2.4 keV for 1.332 MeV γ-rays during accelerator shutdown and 5.4 keV during accelerator operation [56]. In this

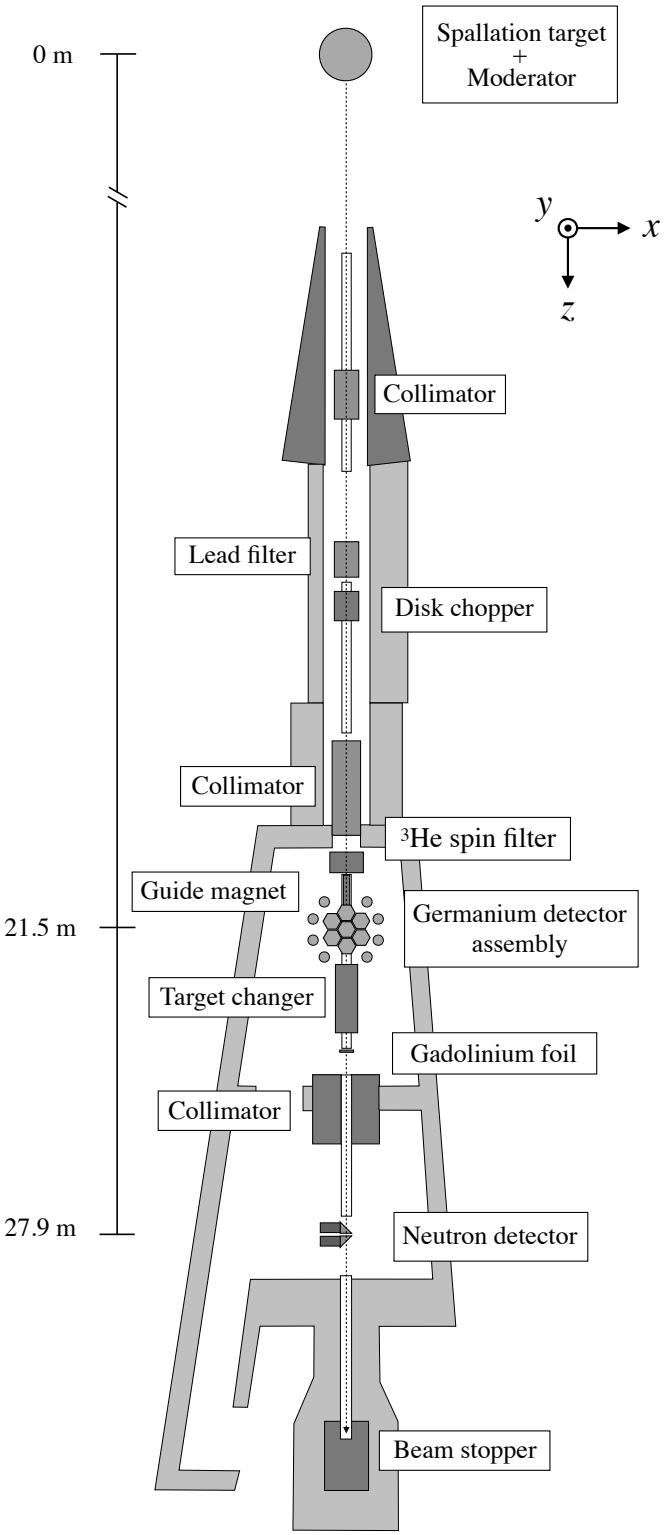

Figure 3.3: Top view of BL04 ANNRI.

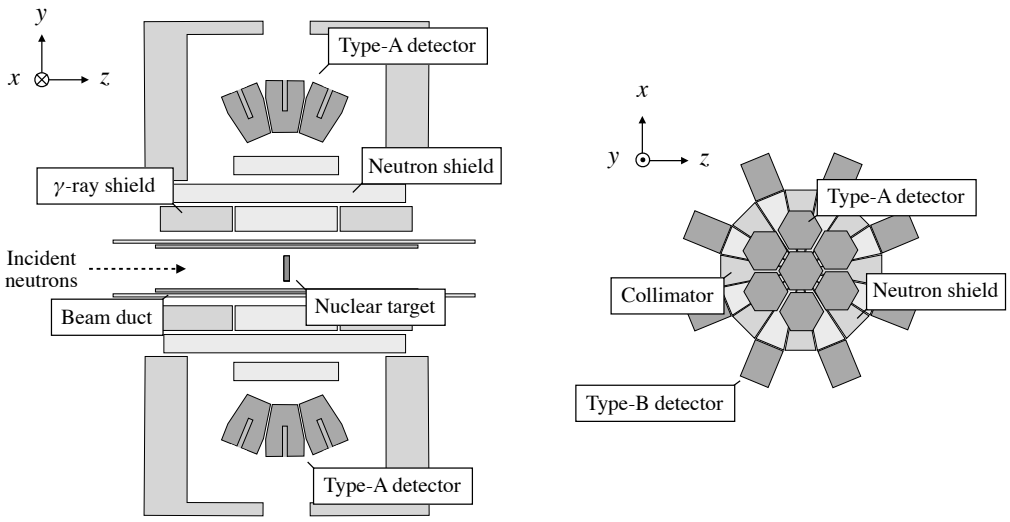

Figure 3.4: Germanium detector assembly. The left figure is a sectional view and the right figure is a top view.

analysis, only the lower A-type detectors were used because the B-type and the upper A-type detectors' condition were unstable. The correspondence between the position and the detector number of the lower A-type detectors is shown in Fig.3.5 and Table 3.3 [57].

3.2.2 Neutron detectors

Two types of lithium glass scintillation detectors were used to detect neutrons transmitted through the target [58]. One was a ^{6}Li 90% enriched type (GS20) and the other was a ^{7}Li 99.99% enriched type (GS30). The size of both scintillators is 50 mm × 50 mm × 1 mm. The

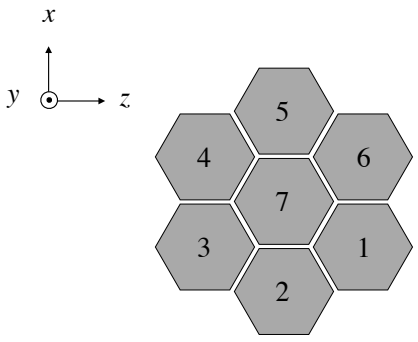

Figure 3.5: Number correspondence of the lower A-type detector (Top-view).

Table 3.3: Correspondence table of detector's number and position angle.

Detector	θ_i (deg)	φ_i (deg)
1	70.9	258.2
2	90.0	246.3
3	109.1	258.2
4	109.1	281.8
5	90.0	293.7
6	70.9	281.8
7	90.0	270.0

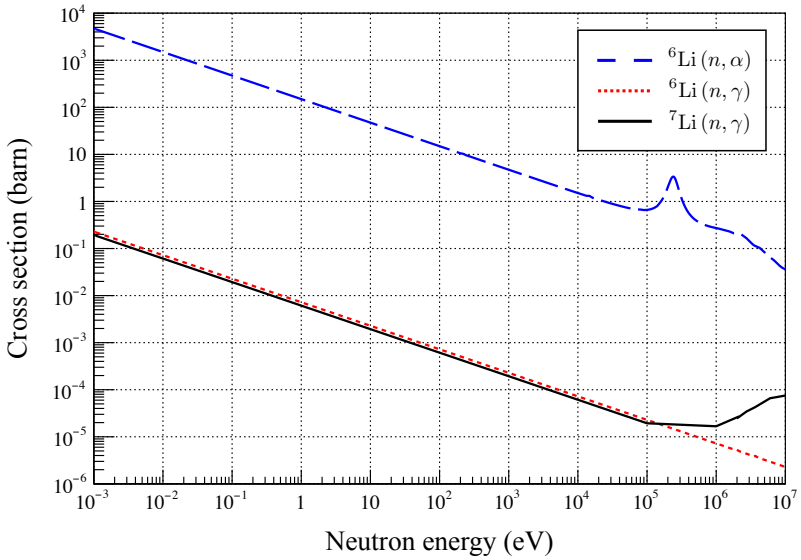

Figure 3.6: Figure of neutron capture cross sections for ^{6}Li and ^{7}Li. The dashed line, dotted line, and solid line show the cross section for $^6\mathrm{Li}\,(n, \alpha)$, $^6\mathrm{Li}\,(n, \gamma)$, and $^7\mathrm{Li}\,(n, \gamma)$, respectively [59].

^{6}Li reacts with neutrons mainly as follows,

$$^6\mathrm{Li} + n \rightarrow {}^3\mathrm{H} + \alpha\ (4.78\ \mathrm{MeV}). \tag{3.1}$$

By doping the scintillator with ^{6}Li, ^{3}H, and α-particles produced by the above reaction produce scintillation light. Therefore, it can be used as a neutron detector. The ^{6}Li isotope has a neutron absorption cross section of 940 barn for 25 meV neutrons as shown in Fig.3.6. On the other hand, ^{7}Li has a very low sensitivity (0.045 barn for 25 meV neutron) for neutron detection. Since GS20 and GS30 have similar sensitivities for γ rays, the γ-ray background of GS20 was evaluated by GS30 by installing two detectors in close proximity as shown in Fig.3.7. Scintillators were connected to the Hamamatsu Photonics H7195 photomultiplier tubes (PMT) whose diameters were 2 inches through a triangular light guide to increase the collection efficiency of scintillation light, and an ORTEC 556H was used for high-voltage power supply.

3.2.3 Data acquisition system

Two types of an analog to digital converter (ADC) were used for germanium detectors and neutron detectors for data acquisition. Since germanium detectors have a high energy resolution, they also require a high ADC resolution. A V1724, 8 channels, 14 bit, 100 MS/s, peak hold digitizer manufactured by CAEN was used as the ADC for the germanium detectors [60]. The neutron detector requires a fast response to the ADC because a high count rate was assumed

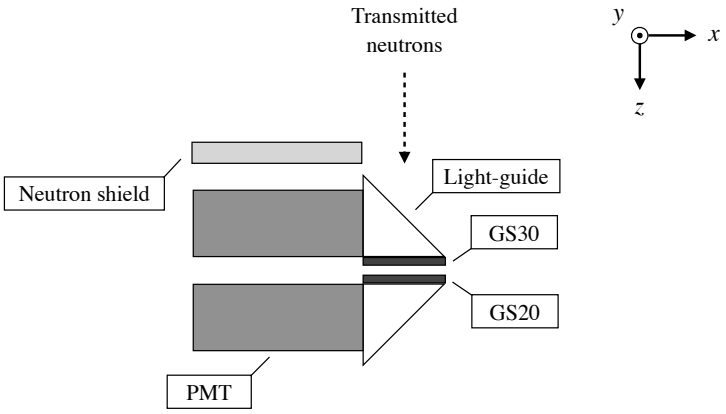

Figure 3.7: Top view of neutron detectors. Detectors were installed at 27.9 m from the moderator surface. GS30 and GS20 were installed in close proximity. Blocks of lithium fluoride were installed to prevent scattered neutrons from irradiating the PMTs.

for a high flux neutron beam. A V1720, 8 channels, 12 bit, 250 MS/s, charge sensitive digitizer was used as the ADC for neutron detectors [60]. The characteristics of each ADC are listed in Table 3.4. The process of signal processing of each ADC is described below. A block diagram of the signal processing of V1724 and V1720 and schematics of the waveform processing are shown in Fig.3.8, 3.9, 3.10, 3.11.

V1724

The signal from the germanium detector is converted from analog to digital by the ADC. The sampling rate is reduced by the Decimator to suppress high frequency noise. The signal is distributed to two signals, one sent to the "Trigger & Timing Filter (TTF)" and the other to the "Trapezoid Filter (TF)". TTF converts the signal to a bipolar signal, sends the zero-crossing point to the Counter, and sends it as a trigger signal to TF signal system. The Clock (CLK) outputs the Time Stamp of the signal sent to the counter, and the origin of the time is the timing information of the proton entering the mercury target supplied from MLF. On the other hand, the signal sent to TF is shaped into a trapezoid. After the trapezoidal shaping, the integration region of the trapezoidal signal is determined by referring to the trigger signal sent from TTF, and the pulse height information is output after the integration. When the time difference between the signals Δt in Fig.3.9 is in the range of 0.4 μs to 3.2 μs, it is called a "pile-up event", and the time stamp is recorded but the pulse height information is not recorded. Furthermore, when two signals are close and Δt is less than 0.4 μs, the two signals are processed as one signal, and neither time stamp nor pulse height information is recorded. Such an event is called a "dead event".

Table 3.4: Characteristics of ADCs [60].

Model	V1724	V1720
Sampling clock frequency	100 MHz	250 MHz
Resolution	14 bits	12 bits
Digitization	Peak-Hold	Charge-Integration
Impedance	50 Ω common mode	100 Ω differential mode

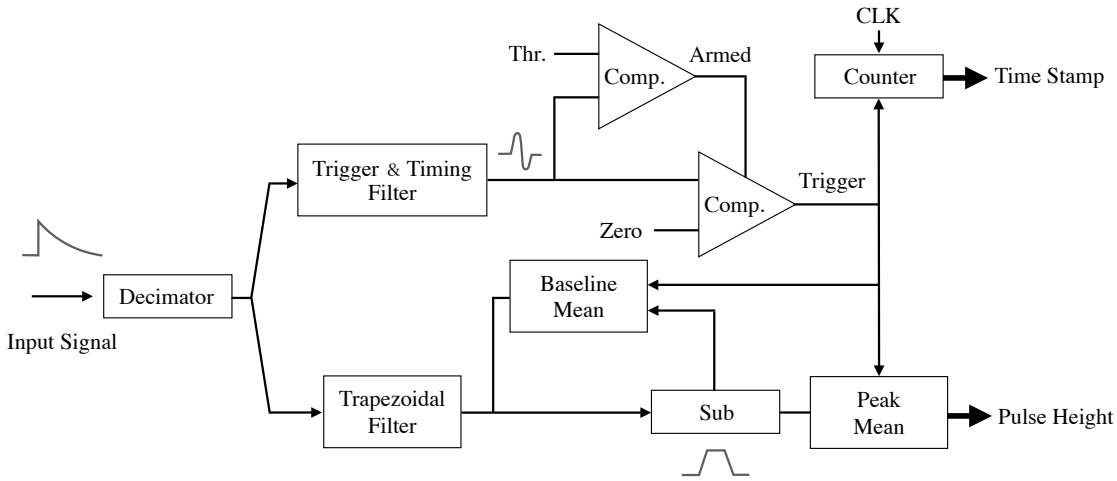

Figure 3.8: Block diagram of the signal processing chain for V1724 [60].

V1720

As in V1724, the analog signal from the Li-glass detector is converted into a digital signal by the ADC. The signal is distributed to TTF and Delay circuit. TTF converts the signal to a dipole signal and records the zero crossing point as the event generation time. The information of the point exceeding the threshold is transmitted to the Delay circuit. The signal sent to the Delay circuit is delayed, and the gate signal generated by the trigger signal from the TTF system is referred to, integrated by the Accumulator, and output as the pulse height information.

In the timing processing system, the difference between proton incident timing and the detection time is recorded as time information t^m. We can calculate the neutron energy E_n applying the time-of-flight (TOF) method and the pulse height information obtained in V1724 correspond to γ-ray energy E_γ after energy calibration.

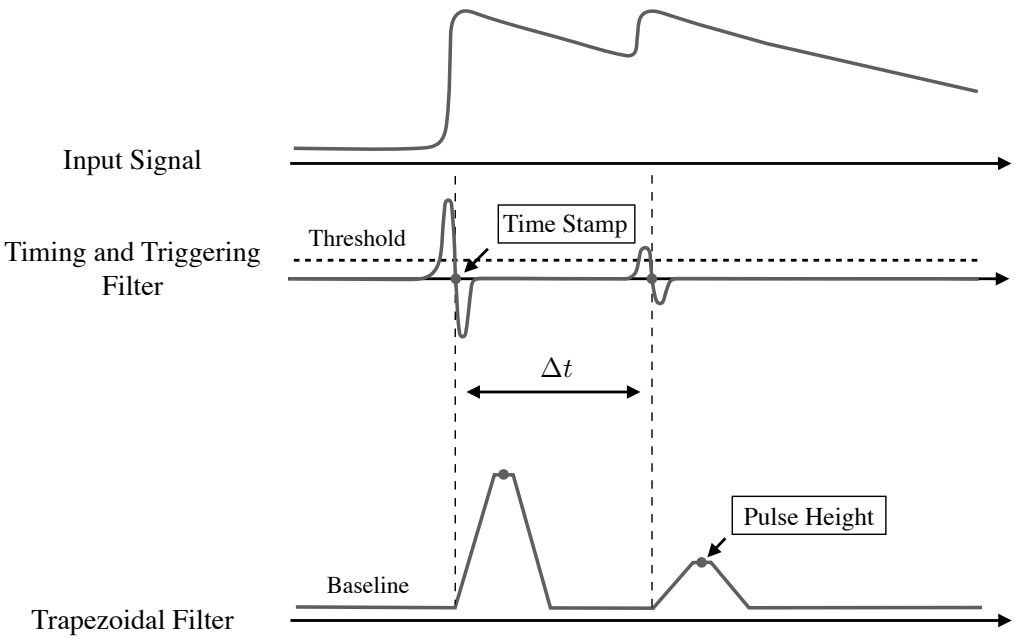

Figure 3.9: Schematic of the waveform processing in pulse height and time information processing system in V1724 [60].

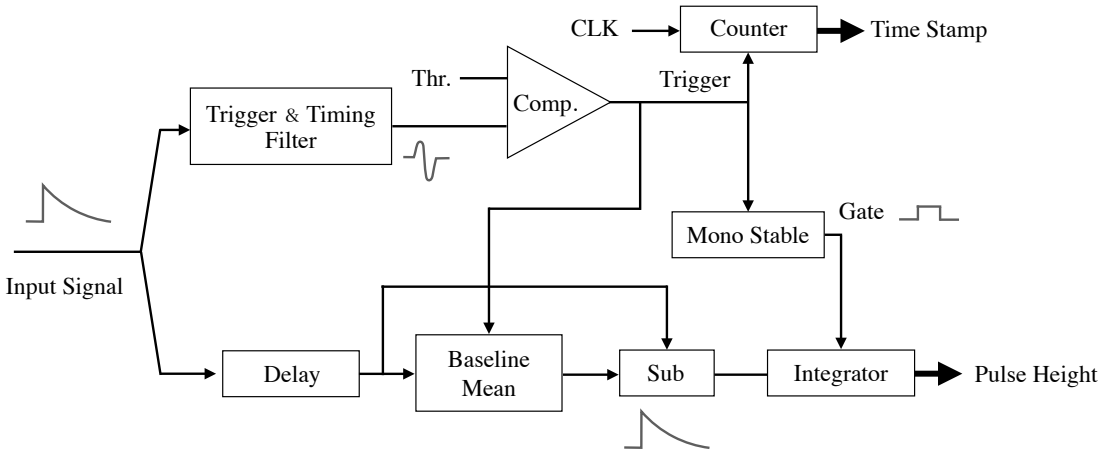

Figure 3.10: Block diagram of the signal processing chain for V1720 [60].

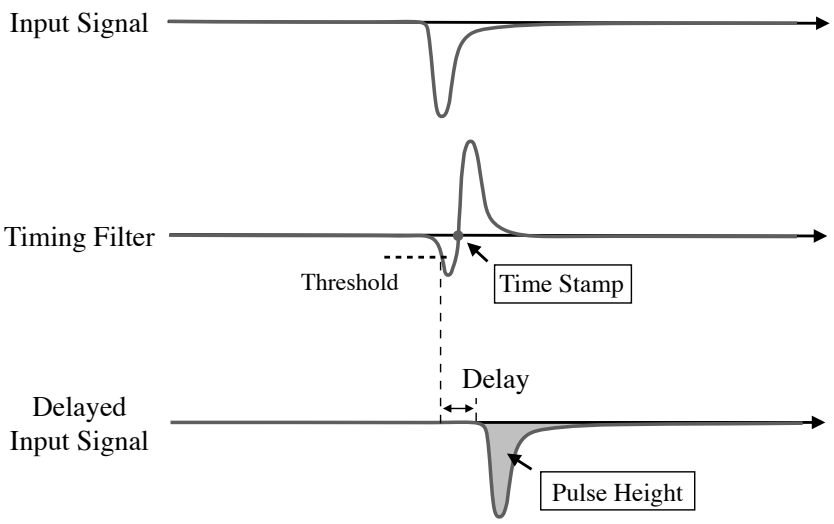

Figure 3.11: Schematic of the waveform processing in pulse height and time information processing system in V1720 [60].

3.2.4 Neutron polarizer

A ^{3}He spin filter was used as the neutron polarizer. The ^{3}He spin filter polarizes neutrons by utilizing the large spin-dependent cross section between ^{3}He and neutrons: the absorption cross sections for 25 meV neutrons with spins parallel and antiparallel to ^{3}He are approximately 0 and 10666 barn, respectively. The ^{3}He spin filter is a glass cell filled with ^{3}He gas and alkali metal. The ^{3}He was polarized by a spin exchange optical pumping (SEOP) method [61]. In this experiment, two kinds of SEOP methods were used. Each principle is described below.

SEOP

The SEOP method is a kind of DNP method. The rubidium atoms are polarized by the infrared ($\sim$770 nm) circularly polarized laser as shown Fig.3.12, and the ^{3}He nuclei are polarized via the hyperfine interaction. Since rubidium is solid at room temperature, metal rubidium is vaporized by heating (170 °C – 230 °C) and spin exchanged with ^{3}He. During these process, the quantization axis is defined by the applied external magnetic field. Type 180 glass (GE180) manufactured by General Electric Co. is generally used for the glass cell. Since GE180 does not contain boron with large neutron absorption cross section which is often contained in ordinary glass, neutron absorption is suppressed. In addition, since the surface is non-porous, relaxation of the ^{3}He polarization due to the wall collision can be suppressed.

Hybrid SEOP

The hybrid SEOP method is an evolution of the traditional SEOP method, in which ru-

Table 3.5: Physical parameters of alkali metals

Element	K	Rb
$\sigma_{\rm sd}$ (Å^2)	0.0128[a]	0.0994[a]
$k_{\rm se}$ (cm^3/s)	7.5×10^{-20}[b]	6.8×10^{-20}[c]

[a] Taken from Ref.[63].
[b] Taken from Ref.[64].
[c] Taken from Ref.[65].

bidium metal and potassium metal are filled in a glass cell [62]. Laser-pumped rubidium atoms spin exchange with potassium atoms and polarize the potassium atoms at approximately 100%. And, the polarization of the potassium atom transfers to the ^{3}He nucleus via the hyperfine interaction. Although there is a process in which the polarization of alkali metal is relaxed by the collision of alkali metal atoms, while the spin exchange rate $k_{\rm se}$ with ^{3}He is approximately equal as shown in Table 3.5, the spin destructive cross section $\sigma_{\rm sd}$ of potassium is one order lower than that of rubidium. As a result, the presence of potassium atoms facilitates the polarization of ^{3}He.

In this experiment, laser pumping was carried out in a SEOP system at either a polarizatoin station located within or outside of MLF as shown in Fig.3.13. As shown in Fig.3.14, a glass cell installed in a solenoid coil in the SEOP system was temperature-controlled by a heater and optimum temperature was determined by monitoring the polarization of ^{3}He by the adiabatic fast-passage (AFP) NMR method as shown in Fig.3.15. AFP-NMR is a method to flip the spin by following the spin to the effective magnetic field by applying the oscillating magnetic field in the direction perpendicular to the static magnetic field applied [66].

The polarization of ^{3}He is relaxed by various processes. The main processes include the relaxation by the magnetic dipole interaction between ^{3}He, the collision with the wall of the glass cell, and the spatial inhomogeneity of the magnetic field [67, 68]. Since the spatial inhomogeneity of the magnetic field strongly depends on the experimental environment, it is especially necessary to construct the optimum magnetic field environment in correspondence with the experimental environment. For this the optimum magnetic field design was estimated with Finite Element Method (FEM) analysis using Femtet manufactured by Murata Software Co. and FEMM [69], and the solenoid coil and a guide magnet were developed and installed. Details of the magnetic field design are given in Appendix B.

A solenoid coil was used to define the quantization axis and to suppress the relaxation of ^{3}He polarization due to the inhomogeneity of the external magnetic field. In this experiment, up and down polarized neutrons are defined as parallel and antiparallel to the x axis, respectively.

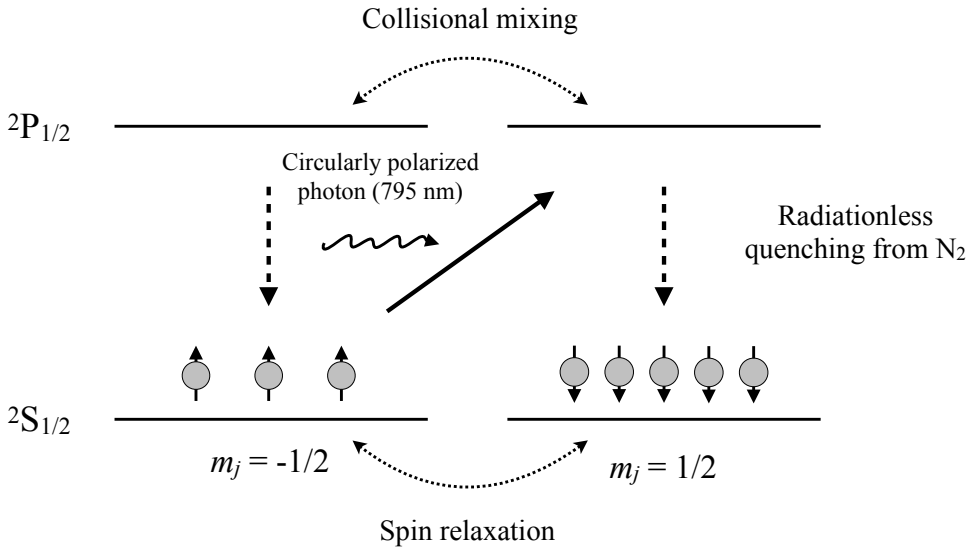

Figure 3.12: Energy state and transition process of rubidium in the SEOP method (A simplified two-level transition scheme). When rubidium interacts with polarized photons, rubidium is excited from the ground state of $^2S_{1/2}$ to $^2P_{1/2}$. However, it is restricted to the transition from $m_j = -1/2$ to $m_j = 1/2$ by the selection rule of magnetic quantum numbers. In addition, it transitions from $^2P_{1/2}$ to $^2S_{1/2}$ by the collision with the nitrogen molecules. This process is repeated, the electrons at a specific level increase, the rubidium atoms become polarized, and the polarized rubidium and ^{3}He nuclei can exchange spin via the hyperfine interaction, and the ^{3}He nuclei become polarized.

A magnetic field of approximately 15 G was applied by the solenoid coil at the cell installation position. In order to polarize neutrons along the x axis, after ^{3}He was polarized by SEOP, the glass cell was rotated adiabatically 90 degrees in the solenoid coil as shown in Fig.3.16.

Since the spin of ^{3}He follows the magnetic field of the solenoid coil, ^{3}He is polarized in the x axis direction. The spin filter was installed into the beam line after the ^{3}He was polarized in the ^{3}He polarization station [70]. As shown in Fig.3.17, unpolarized neutrons were injected through the side of the solenoid coil. After passing through the spin filter, a guide magnetic field was applied from the ^{3}He spin filter to the target using a permanent magnet to maintain the polarization of neutrons.

3.2.5 Nuclear target

Lanthanum and melamine ($C_3H_6N_6$) were used as nuclear targets. The lanthanum target was a metal lanthanum plate of 40 mm × 40 mm × 3 mm with a purity of 99.9%. Table 3.6 shows the concentration of impurities in the lanthanum target. The melamine target was a melamine resin plate of 40 mm × 40 mm × 2 mm. The melamine target is used for the relative γ-ray detection efficiency correction using γ rays emitted by $^{14}N(n,\gamma)$ reaction of nitrogen contained

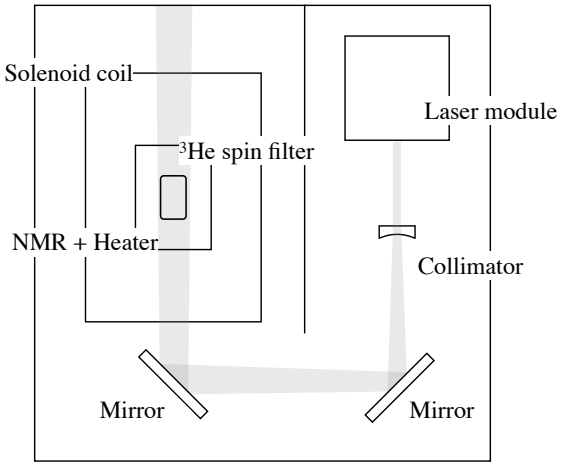

Figure 3.13: Top view of the ^{3}He pumping system in the pumping station at MLF. The circularly polarized laser irradiated from the laser module is diffused by a collimator, reflected by two mirrors, and irradiate a glass cell fixed in a cylindrical container of a NMR coil and a heater installed inside a solenoid coil.

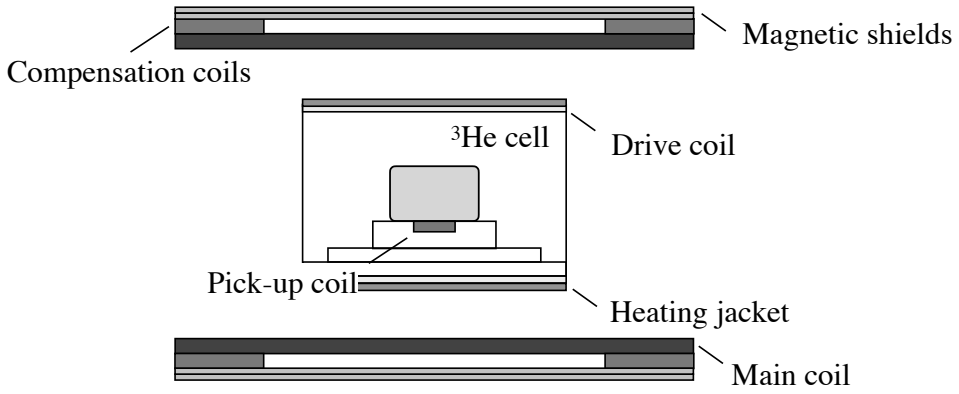

Figure 3.14: Cross-sectional view of ^{3}He spin filter. A solenoid coil of 300 mm in diameter and 500 mm in length with an aluminum wire of 0.95 mm in diameter coated with polyester was used as a conductor. The main coil is one wound layer, and the compensation coils are one wound layer on both outer sides. The entire solenoid is covered with a 0.1 mm thick permalloy film to shield the external magnetic field. A drive coil for NMR is wound around a cylindrical container inside the solenoid coil. This cylindrical container is also covered with a jacket heater, which is used to raise the temperature of the glass cell when ^{3}He is laser-pumped. In addition, a pickup coil is installed in the lower part of the glass cell in order to detect the signal by NMR and evaluate the polarization ratio of ^{3}He.

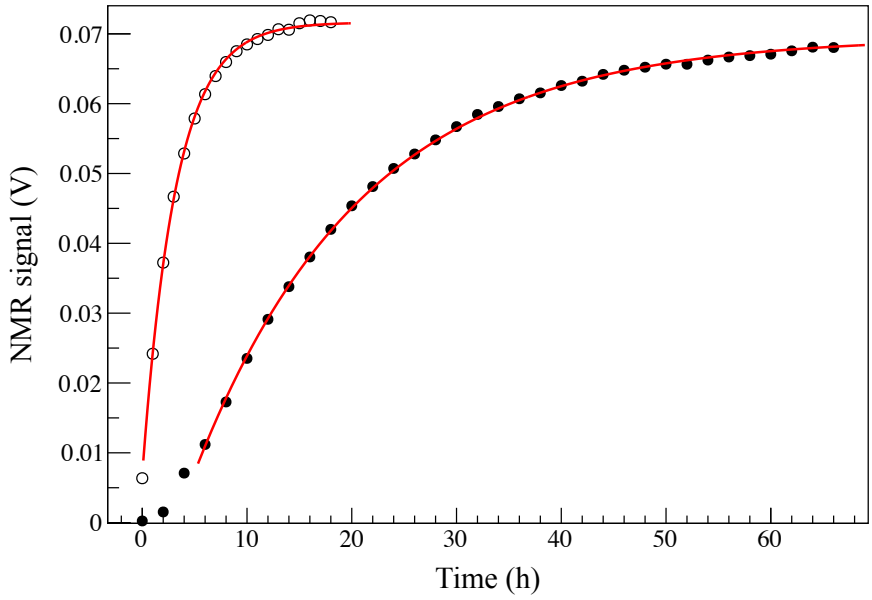

Figure 3.15: Time dependence of the polarization ratio of ^{3}He detected by the AFP-NMR during the laser pumping. Black and white points represent SEOP and hybrid SEOP methods, respectively. The solid line shows the fitting result by the buildup function $(1 - e^{-t/\tau_{\mathrm{build}}})$, where t is the pumping time and τ_{build} is time constant of the buildup for the ^{3}He. It takes 1–2 days to reach the maximum polarization ratio of ^{3}He in the case of the SEOP method, while it takes about half a day in the case of the hybrid SEOP method. Note that since the intensity of the NMR signal depends on the size of the cell and the positional relationship with the pickup coil, the comparison of the absolute values of both is not very important.

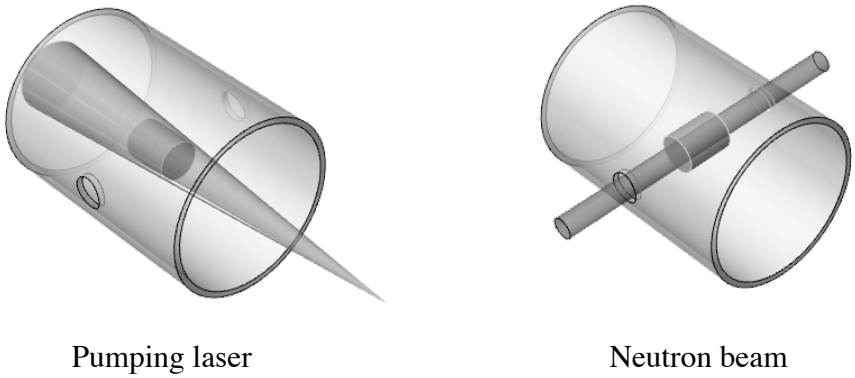

Figure 3.16: Arrangement of the glass cell in solenoid coil. In laser pumping, the glass cell is installed in a direction coaxial with the solenoid coil. The glass cell is rotated by 90 degrees when it is installed into the beam line and irradiated by the neutron beam. The aluminum cylinder around which the solenoid coil is wound and the permalloy film have holes 50 mm in diameter on the side surfaces to prevent direct neutron beam irradiation.

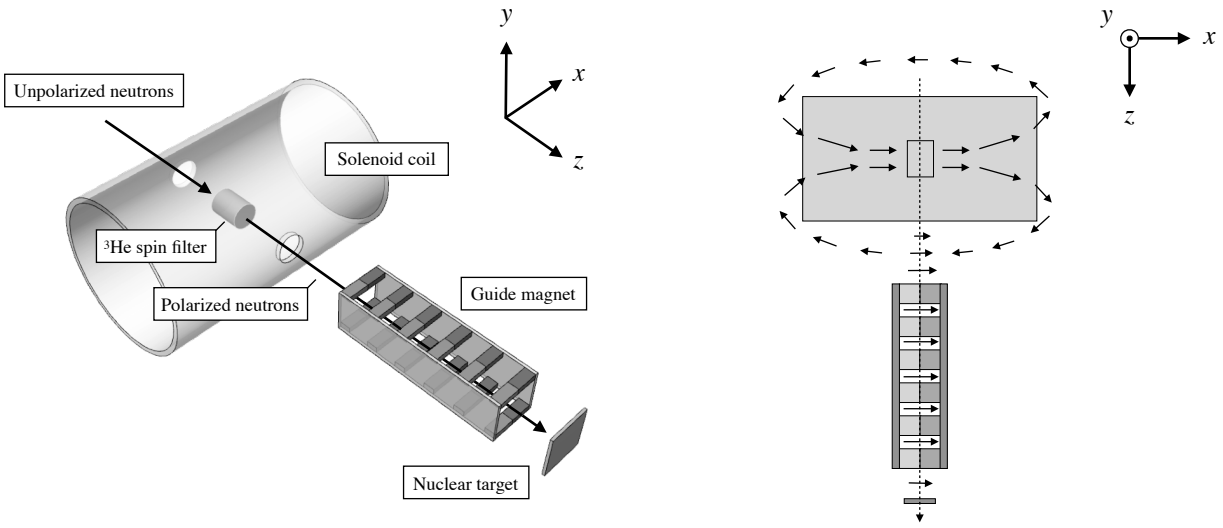

Figure 3.17: ^{3}He spin filter and a guide magnet for neutron spin transport. The left figure is a solid view of the system. Unpolarized neutrons were injected from the side of the solenoid coil and polarized by passing through the ^{3}He spin filter installed in the solenoid coil, after which they irradiate the downstream nuclear target. The right figure is a top view of the system. Solid arrows indicate the direction of the magnetic field and a dashed arrow indicates the direction of the neutron beam. The magnetic field antiparallel to x axis outside the solenoid coil was canceled by the guide magnet composed of permanent magnets, and in addition, the magnetic field was applied in the x axis parallel direction. Therefore, polarized neutrons always maintained polarization due to adiabatic transport in the guiding magnetic fields.

Table 3.6: Impurities within the lanthanum target evaluated by the Inductively Coupled Plasma (ICP) spectrometry.

Material	Quantity (ppm)
Neodymium	101
Cerium	81
Praseodymium	63
Samarium	57
Dysprosium	48
Yttrium	36

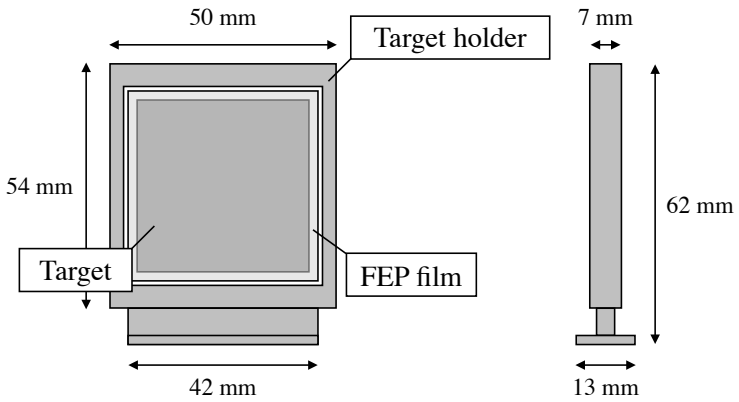

Figure 3.18: Illustration of the target and the target holder. The target packaged with FEP film is fixed to the PTFE holder.

in melamine. Emitted γ rays are considered to be isotropic because ^{14}N has no p-wave resonance or resonance with higher angular momentum below 400 eV. In addition, since the energy of the γ-rays are over 2000 keV – 11000 keV, corrections in the region of our interest are possible.

All targets were packaged in a 5 μm thick fluorinated-ethylene-propylene[2] (FEP) film to avoid oxidation and neutron scattering. FEP film is composed of only carbon and fluorine, which allow low background measurements because of their small neutron reaction cross sections. In addition, since it does not contain hydrogen, background by scattered neutrons is suppressed, and it is thus suitable as a packing material. The target packaged with FEP film is fixed to a polytetrafluoro-ethylene[3] (PTFE) holder as shown in Fig.3.18. PTFE is also a low background material like FEP. The target is installed in the center of the germanium detector with sub-milli-order precision by a target changer in BL04.

[2] $(-CF_2 - CF_2-)_n (-CF_2CF(CF_3)-)_m$
[3] $(-CF_2 - CF_2-)_n$

Chapter 4

Measurement

This chapter describes the results of asymmetry measurements of the ^{139}La$(\vec{n},\gamma)$ reaction with polarized neutrons as well as the methods used for calibration and correction of data. The experiments were carried out over three beam cycles as shown in Table 4.1 and all results are summarized in Table.4.2 at the end of this chapter. In the measurement, a ^{3}He spin filter was installed onto the beam line, and the polarization direction of ^{3}He was flipped by the AFP-NMR method approximately once every 4 hours. Pulse-height and time information of γ rays emitted in the (n,γ) reaction were acquired from germanium detector, and pulse-height and time information of transmitted neutrons which passed through the target were acquired from lithium glass detectors.

4.0.1 Determination of Neutron Energy by TOF method

Neutron energy E_n can be determined by the TOF method. The time information t^m acquired by the ADC and E_n have the following relationship,

$$\begin{aligned} E_n &= \frac{1}{2} m_n v_n^2 \\ &= \frac{1}{2} m_n \left(\frac{L}{t^m - t_0} \right)^2 , \end{aligned} \tag{4.1}$$

Table 4.1: Conditions for a series of measurements.

Series	Beam power (kW)	Measurement time (hour)	DNP method
March 2019	520	82	SEOP
May 2019	520	72	SEOP
June 2020	600	72	Hybrid-SEOP

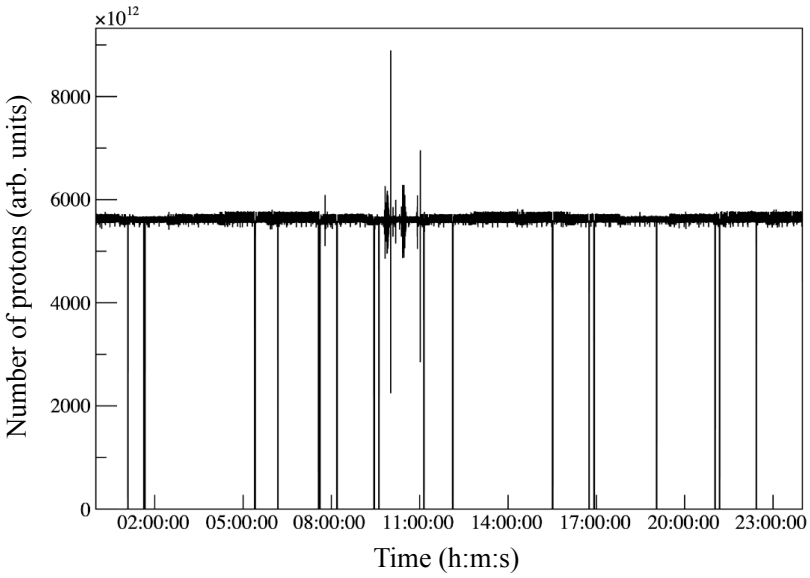

Figure 4.1: The time variation of the number of protons incident on a mercury target measured by the current transformer on May 28, 2019 is shown. The proton beam intensity fluctuates by approximately 1%. The decrease in the number of protons indicates that the proton beam injection stopped due to a malfunction of the accelerator.

where m_n is mass of neutron, v_n is velocity of neutron, L is the distance from the surface of the moderator to the target and t_0 is the timing offset of the data acquisition. The value of L was 21.5 m and 27.9 m for germanium detector and lithium glass detector, respectively, and the value of t_0 was approximately 2.5 μs.

4.0.2 Proton beam current correction

The number of protons injected into the spallation source was measured by the current transformer and provided with the time of incidence as shown in Fig.4.1. Since the number of neutrons produced by spallation is proportional to the number of incident protons, each measurement was normalized using this information.

4.1 Measurement of transmitted neutrons

Neutrons transmitted through the target are detected by lithium glass detectors. The performance of the ^{3}He spin filter, the ^{3}He polarization ratio, and neutron polarization ratio were evaluated by the measurement of transmitted neutrons, and they were used to correct the analysis of the $(\vec{n}, \gamma)$ reaction.

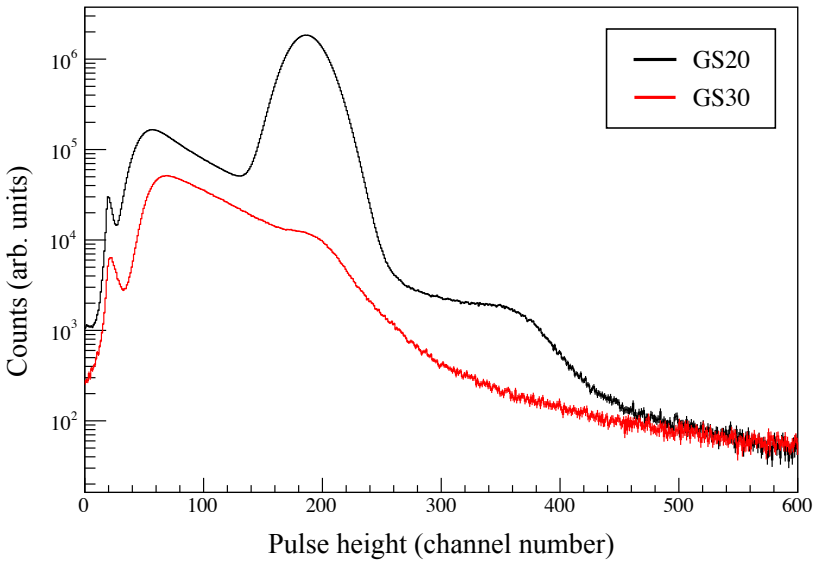

Figure 4.2: Neutron pulse-height spectra of GS20 and GS30. Black and red lines represent the spectra of GS20 and GS30, respectively. The ratio of the single neutron detection events in the 200 channel to the double neutron detection events in the 360 channel is approximately less than 0.1% and was statistically negligibly small in this measurement.

4.1.1 Neutron event selection

Two-dimensional data of the pulse-height and TOF information were acquired from the lithium glass detectors. Figure 4.2 shows the pulse height spectra of GS20 and GS30. The large peak near 200 channels in the pulse-height spectrum of GS20 corresponds to a single neutron detection event, and the peak near 360 channels corresponds to a double neutron detection event. Most components of the pulse-height spectrum of the GS30 is γ-ray background events, while the small peaks near 200 channels correspond to the single neutron detection events as well as those seen in the pulse-spectrum of GS20. This peak was used for the pulse-height calibration between GS20 and GS30. These neutron event regions were gated and neutron events were selected. Figure 4.3 shows the TOF spectra of GS20 and GS30, and there is a structure in which the number of events rapidly decreases around $t^m \sim$ 35000 μs in the spectrum of GS20, because low-energy neutrons were cut by the disk chopper. Since only γ-ray background exist in this region and the counts of both spectrum are equal, it is estimated that the γ-ray detection efficiency was approximately equivalent. The γ-ray background was removed by subtracting the spectrum of GS30 from GS20. γ-ray background events were less than approximately 1% of neutron events in the region excluding high and low energies (750 μs $\leqslant t^m \leqslant$ 25000 μs). Therefore, this region is used in the analysis involving the lithium glass detector.

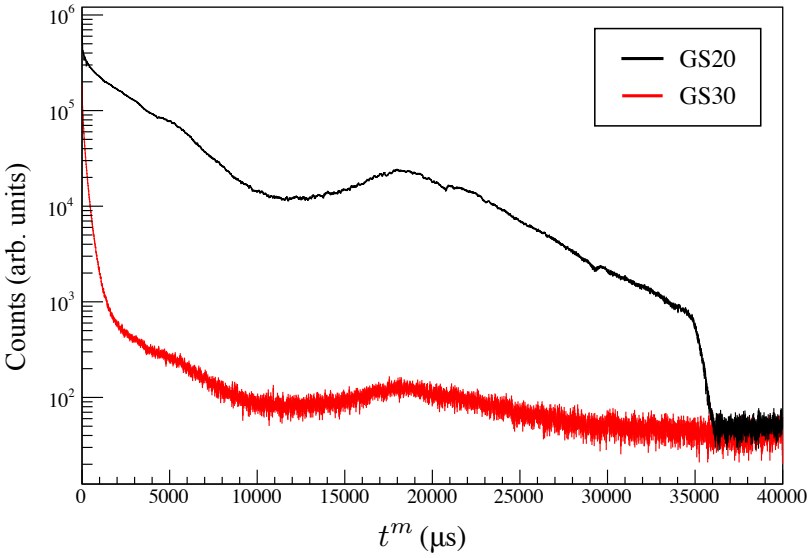

Figure 4.3: Neutron TOF spectra of GS20 and GS30. Black and red lines represent the spectra of GS20 and GS30, respectively.

4.1.2 Determination of Neutron transmittance and polarization ratio

The neutron transmittance for the unpolarized ^{3}He spin filter is written as

$$T_{\mathrm{unpol}} = T_{\mathrm{cell}} \exp\left(-n_{\mathrm{He}} t_{\mathrm{He}} \sigma_{\mathrm{He}}\right), \tag{4.2}$$

where T_{cell} is the neutron transmittance of the vacuum glass cell, n_{He} is the atomic number density of ^{3}He, t_{He} is the cell length and σ_{He} is the neutron total cross section of ^{3}He. Therefore, the effective thickness $n_{\mathrm{He}} t_{\mathrm{He}}$ of ^{3}He which fills the cell can be evaluated by measuring the transmittance of the unpolarized ^{3}He spin filter and the transmittance of the vacuum glass cell, separately. The ratio of the neutron TOF spectra of the two measurements is shown in Fig.4.4. The absorption cross section component contained in σ_{He} is extrapolated from the cross sections at 25 meV, assuming the energy dependence from the $1/v_n$ law. The value of $n_{\mathrm{He}} t_{\mathrm{He}}$ was evaluated by fitting using Eq.4.2. The largest contribution to the systematical uncertainty of the value of the $n_{\mathrm{He}} t_{\mathrm{He}}$ is the shape difference between the ^{3}He cell and the vacuum glass cell, and it is assumed that there is a shape difference of at most 1%. The neutron transmittance of the ^{3}He spin filter when the ^{3}He is polarized T_{pol} can be described as follows,

$$T_{\mathrm{pol}} = T_{\mathrm{unpol}} \cosh(P_{\mathrm{He}} n_{\mathrm{He}} t \Delta\sigma_{\mathrm{He}}), \tag{4.3}$$

where P_{He} is the polarization ratio of the ^{3}He and $\Delta\sigma_{\mathrm{He}}$ is the neutron absorption cross section of ^{3}He. As shown in Fig.4.5, the polarization ratio of ^{3}He was evaluated by fitting using Eq.4.3.

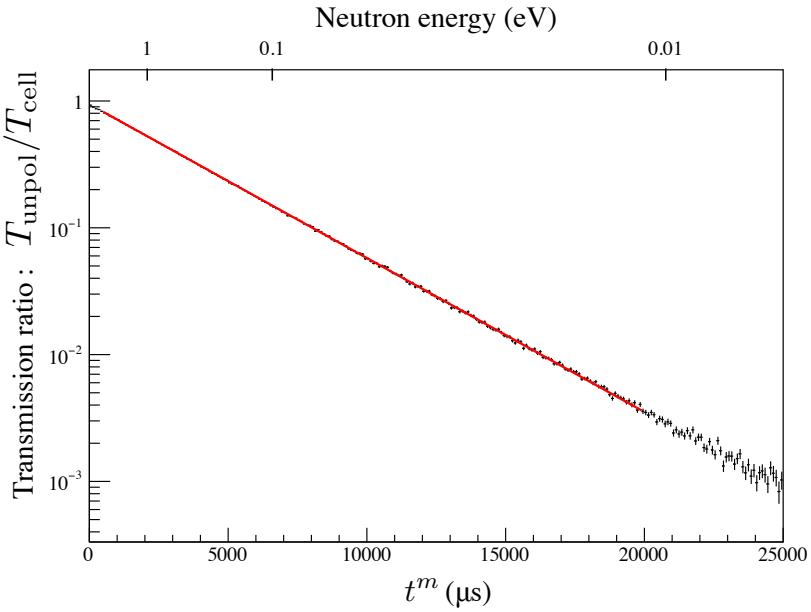

Figure 4.4: Ratio of neutron transmission through unpolarized ^{3}He to that through the vacuum glass cell. The solid line is the result of fitting by $T_{\rm unpol}/T_{\rm cell} = \exp(-n_{\rm He}t_{\rm He}\sigma_{\rm He})$. From this result, the effective thickness of ^{3}He can be determined.

The neutron polarization ratio P_n and the ^{3}He polarization ratio $P_{\rm He}$ are related through

$$P_n = \tanh(P_{\rm He}n_{\rm He}t\Delta\sigma_{\rm He}). \tag{4.4}$$

The neutron transmittance of the ^{3}He spin filter has time dependence due to the relaxation of ^{3}He polarization (See Appendix B for details on the mechanism of ^{3}He relaxation.). Therefore, the neutron transmittance of the ^{3}He spin filter and the polarization ratio of neutrons incident on the target also change. Figure 4.6 shows the time dependence of the polarization ratio of ^{3}He from the installation of the ^{3}He spin filter onto the beamline towards the end of the measurement. The polarization of ^{3}He relaxes with time according to the following,

$$P_{\rm He} = P_0 e^{-t/\tau_{\rm decay}}, \tag{4.5}$$

where P_0 is the polarization ratio of ^{3}He at the start of the measurement, $\tau_{\rm decay}$ is the relaxation of ^{3}He time and t is the measurement time. The relaxation of ^{3}He time was estimated by fitting using Eq.4.5. These results were used to correct the analysis of $(\vec{n},\gamma)$ reaction in the following section.

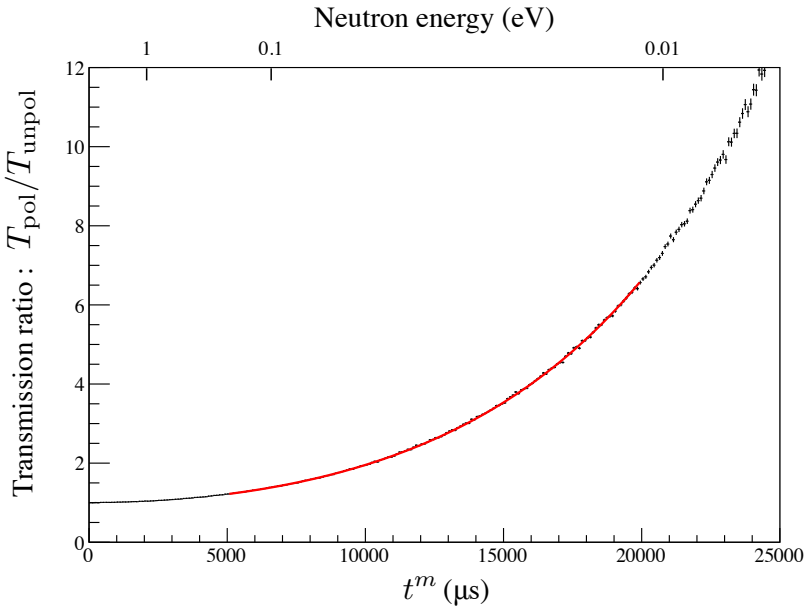

Figure 4.5: Ratio of neutron transmission through polarized ^{3}He to that through unpolarized ^{3}He. The solid line is the result of fitting by $T_{\rm pol}/T_{\rm unpol} = \cosh(P_{\rm He} n_{\rm He} t_{\rm He} \Delta\sigma_{\rm He})$. From this result, the ^{3}He polarization can be determined.

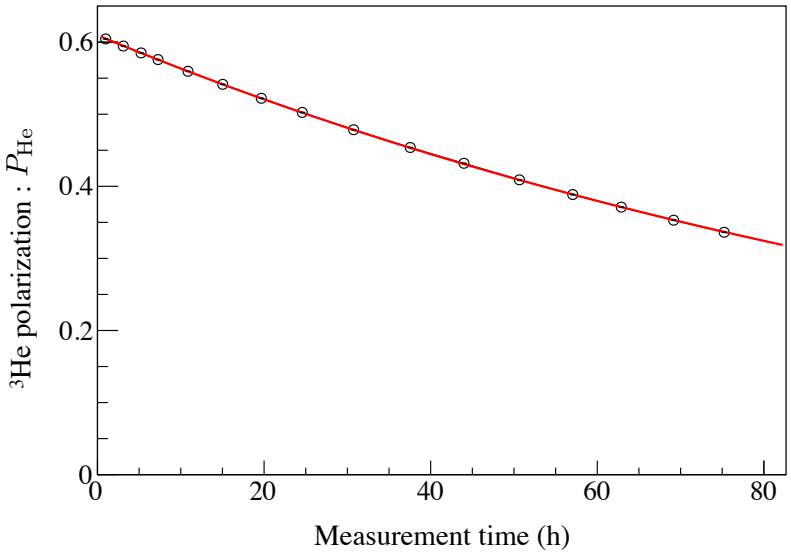

Figure 4.6: Time dependence of the polarization ratio of ^{3}He in the depolarization process. The polarization of ^{3}He relaxed with time. The solid line is the fitting result of the relaxation time constant using the exponential decay function as given by Eq.4.5

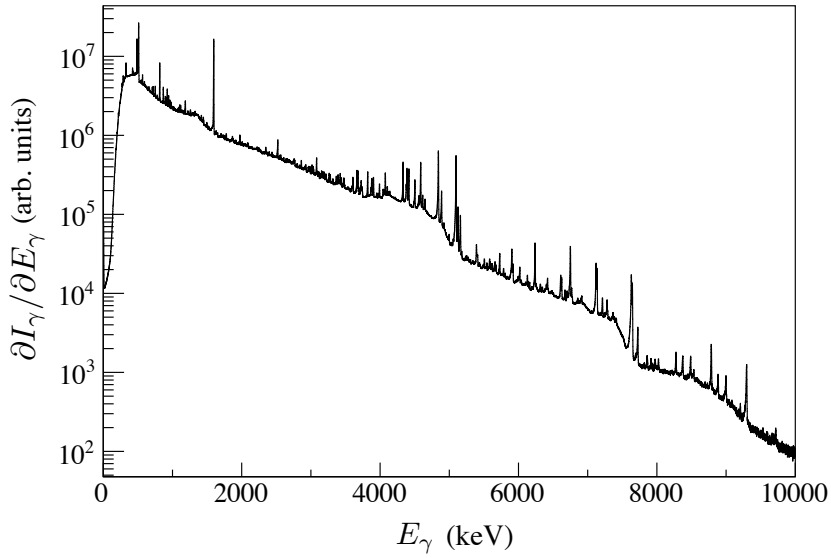

Figure 4.7: Pulse-height spectrum of γ rays from the (n, γ) reaction with a lanthanum target.

4.2 Measurement of γ rays from $(\vec{n}, \gamma)$ reaction

γ rays generated by the (n, γ) reaction were detected by the germanium detector. The germanium and neutron detectors can obtain two-dimensional pulse-height and TOF information. Hereinafter, the total number of γ-ray detected by the germanium detector is denote I_γ.

4.2.1 Energy calibration for γ-ray energy

Figure 4.7 shows the pulse-height spectrum of the germanium detector obtained by neutron irradiation of the lanthanum target. The value of the pulse-height is proportional to the energy deposit of γ rays in the germanium crystal. Since the utilization of peaks in the low and high energy regions enables energy calibration over a wide range, the energy calibration for the pulse-height utilizes peaks of a 511 keV photo-peak due to electron-positron pair production and a 5098 keV peak from the ^{139}La(n, γ) reaction. Figure 4.8 shows the neutron TOF spectrum of the germanium detector obtained by neutron irradiation of the lanthanum target.

4.2.2 Pile-up correction

As described in the previous chapter, the ADC that processes signals from the germanium detector which lose pulse-height information are labeled "pile-up events" when the time difference between the signals Δt in Fig.3.9 is in the range of 0.4 μs to 3.2 μs. When gated by γ-ray

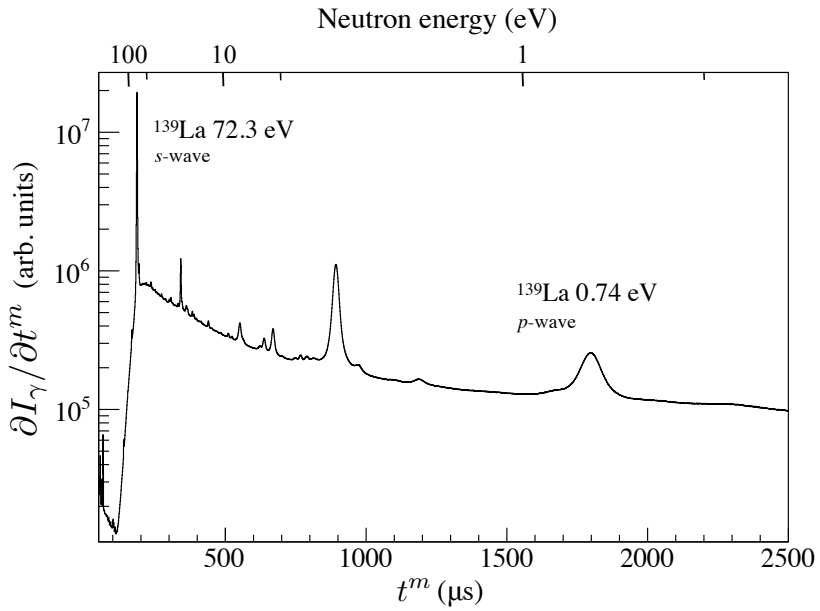

Figure 4.8: Neutron TOF spectrum of γ rays from the (n, γ) reaction with the lanthanum target. The resonance at around $t^m \sim 1800$ μs and 200 μs are the p-wave resonance of ^{139}La and the s-wave resonance of ^{139}La, respectively.

energy, a "pile-up event" is missing from the neutron TOF spectrum because it has no γ-ray energy information. If the number of "pile-up events" at time t^m is defined as $N_{\rm pu}$ and the number of "non pile-up events" (Events with both time and pulse height information) is defined as $N_{\rm npu}$, then the ratio of these events is defined as $R_{\rm pu} = N_{\rm pu}/N_{\rm npu}$. Events gated by γ-ray energy are corrected in the following relation.

$$N_{\rm gated} = N'_{\rm gated}\,(1 + R_{\rm pu})\,, \tag{4.6}$$

where $N'_{\rm gated}$ is the number of events before the correction when gated by γ-ray energy, and $N_{\rm gated}$ is the number of events after the correction. Figure 4.9 shows the spectrum of a typical pile-up ratio of the lower A-type detector in the vicinity of the p-wave resonance of the ^{139}La(n, γ) reaction. It can be seen from this that the pile-up correction is approximately 5% – 6% corrected in the vicinity of the p-wave resonance. Since the total "dead events" are one order of magnitude smaller than the "pile-up events", they are statistically negligibly small in this analysis.

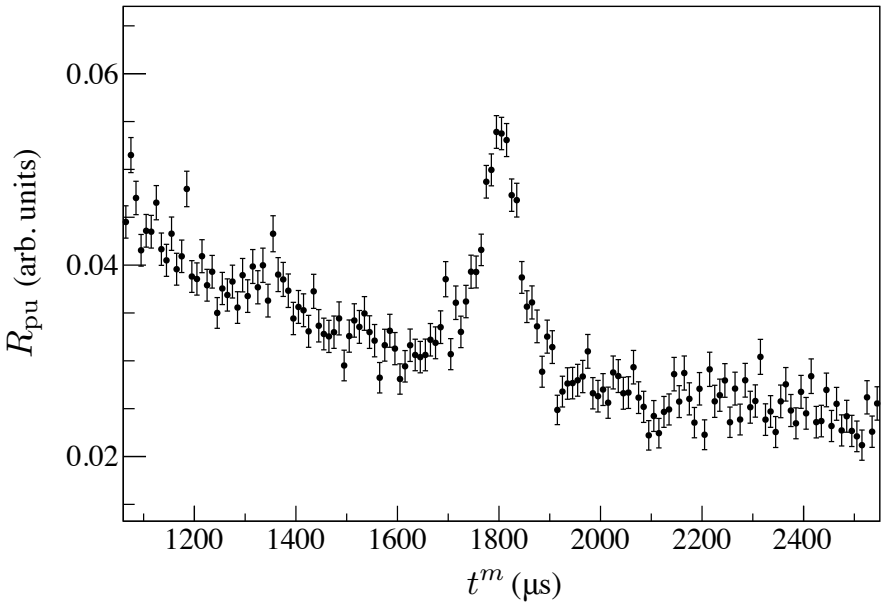

Figure 4.9: The spectrum of the pile-up ratio in the vicinity of the p-wave resonance in the ^{139}La(n,γ). At the resonance, since the count rate increases, the time difference between the signals becomes short, and pile-up events tend to occur.

4.2.3 Relative γ-ray detection efficiency correction

Each germanium crystal has different size, mounting angle, and γ-ray detection efficiency. Therefore, it is necessary to correct the relative γ-ray detection efficiency between crystals. As described in the previous chapter, 5269 keV γ rays from the ^{14}N(n,γ) reaction were used to correct the relative γ-ray detection efficiency. Figure 4.10 shows the γ-ray spectrum of the ^{14}N(n,γ) reaction, and in the vicinity of 5269 keV is closed up. Compton scattering background components included in the full-absorption peak region were subtracted, and the i-th detector's relative γ-ray detection efficiency ε_i was determined from the ratio of the number of events in the full width at quarter maximum (FWQM) region of the peak. The difference in relative γ-ray detection efficiency between the lower A-type detectors used in this measurement is less than 10%.

4.2.4 Transverse asymmetry

The transverse asymmetry using inclusive γ-ray transitions and single γ-ray transitions were analyzed. The γ-ray yield for the i-th detector in the p-wave resonance region for incident up- and down- spin neutrons can be written as, considering the small cross section in the vicinity

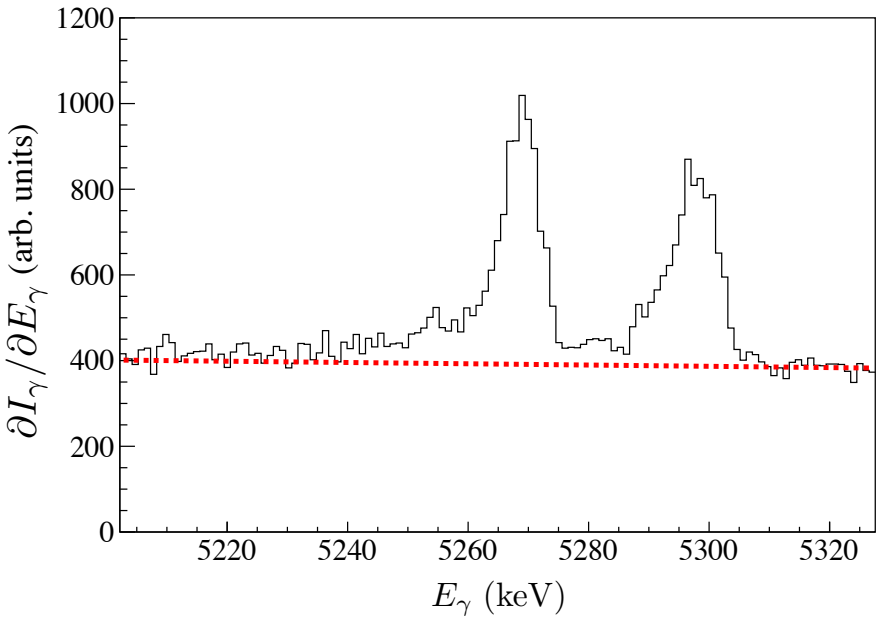

Figure 4.10: γ-ray spectrum of the ^{14}N(n,γ) reaction with melamine target, in particular, a detailed drawing around transitions of 5269 keV and 5298 keV from ^{14}N(n,γ). 5269 keV γ rays were used to correct the relative γ-ray detection efficiency. The dashed line shows the fit result of the background component estimated by a polynomial function.

of the p-wave resonance, respectively,

$$n^{\pm}_{n\gamma}(\theta_i,\varphi_i) \propto \int_{E_\gamma} dE_\gamma \int_{t^m} dt^m \int_{\Omega_i} d\Omega\, \sigma^{\pm}_{n\gamma}(\theta,\varphi)\varepsilon_i, \tag{4.7}$$

where θ_i and φ_i are the i-th detector's mounting angle, Ω_i is the i-th detector's solid angle. The integral region in the p-wave is defined as $E_p - 2\Gamma_p \leqslant E_n \leqslant E_p + 2\Gamma_p$. Resonance parameters, as in Table 2.3, have been well determined by previous studies and used in this analysis.

The γ-ray yield in each detector was weighted using the detector position and lower A-type detectors were added to give the following expressions,

$$N^{\pm} = {\sum_i}' \frac{n^{\pm}_{n\gamma}(\theta_i,\varphi_i)}{\varepsilon_i \lambda_i}, \tag{4.8}$$

where the i-th detector's angular weight factor λ_i is defined as $-\sin\theta_i \sin\varphi_i$ and ${\sum_i}'$ represents the summation of lower A-type detectors. The asymmetry ϵ_γ between N^+ and N^- is defined as follows,

$$\epsilon_\gamma = \frac{N^+ - N^-}{N^+ + N^-}, \tag{4.9}$$

and considering the difference in polarization ratio of neutron between up- and down- spin

neutrons, the transverse asymmetry $A'_{\rm LR}$ is expressed as follows using ϵ_γ

$$A'_{\rm LR} = \frac{2\epsilon_\gamma}{\left(P_n^+ + P_n^-\right) - \epsilon_\gamma \left(P_n^+ - P_n^-\right)}, \tag{4.10}$$

where $P_n^\pm$ is the neutron polarization ratio in each neutron polarization direction obtained from Eq.4.4. Here, when only the p-wave resonance region was focused, the background components in the vicinity of the p-wave resonance, derived from the s-wave resonance and resonances of other nuclei were subtracted from Eq.4.8. The transverse asymmetry $A'_{\rm LR}$ was then defined as in Eq.4.10.

4.2.5 Neutron multiple scattering event correction

Neutron scattering in the target prior to absorption alters the neutron momentum vector and hence impacts the asymmetry. Taking such scattering events into account, $A'_{\rm LR}$ is given by

$$A'_{\rm LR} = \frac{\left(N_{s=0}^+ + N_{s\geq 1}\right) - \left(N_{s=0}^- + N_{s\geq 1}\right)}{\left(N_{s=0}^+ + N_{s\geq 1}\right) + \left(N_{s=0}^- + N_{s\geq 1}\right)}, \tag{4.11}$$

where $N_{s=0}^\pm$ represents the number of events that emit γ rays without scattering in the target and $N_{s\geq 1}$ represents the number of events that emit γ rays after scattering more than once in the target, respectively. Therefore, $A'_{\rm LR}$ and the true asymmetry $A_{\rm LR}$ can be related by

$$A_{\rm LR} = A'_{\rm LR}\left(1 + \frac{N_{s\geq 1}}{N_r}\right), \tag{4.12}$$

where N_r is defined as $\frac{N_{s=0}^+ + N_{s=0}^-}{2}$, which is equal to the component of the p-wave resonance. The ratio was estimated using a Monte Carlo simulation and estimated to be $N_{s\geq 1}/N_r = 0.072 \pm 0.002$ in the vicinity of the p-wave resonance. In the simulation, the polarization direction of incident neutrons is assumed to be transverse to the beam axis and to be spatially isotropically scattered when potential scattering occurs in the target.

Inclusive γ-ray transition

The asymmetry in the resonance region and continuous regions was evaluated by setting the threshold for E_γ to 2000 keV – 15000 keV. Since most of the energy of delayed γ rays generated in this measurement is less than 2000 keV, the effect of delayed γ rays with time-dependent yield can be avoided by setting the threshold value to 2000 keV. As shown in Fig.4.11, it was confirmed that the value of the transverse asymmetry $A_{\rm LR}^{\rm all,inc}$ for inclusive γ-ray transitions before the background subtraction described later was zero over the entire region. The asymmetry was evaluated focusing on the p-wave region. The s-wave component was evaluated by

Table 4.2: Summary of measurement results.

Series	$A_{\mathrm{LR}}^{\mathrm{inc}}$	$A_{\mathrm{LR}}^{\mathrm{gnd}}$	$n_{\mathrm{He}}t_{\mathrm{He}}$ (atm $\cdot$ cm)	τ_{decay} (hours)	$\bar{P}_{\mathrm{He}}$
March 2019	0.015 ± 0.008	0.56 ± 0.24	19.3 ± 0.1	127.0 ± 0.1	0.5
May 2019	-0.010 ± 0.008	0.67 ± 0.33	19.3 ± 0.1	122.3 ± 0.1	0.5
June 2020	0.003 ± 0.005	0.86 ± 0.20	25.4 ± 0.1	93.8 ± 0.1	0.6
Combined	0.003 ± 0.004	0.73 ± 0.14	-	-	-

fitting linear functions with 1400 μs $\leqslant t^m \leqslant$ 1600 μs, 1900 μs $\leqslant t^m \leqslant$ 2200 μs and subtracted as shown Fig.4.12. Figure 4.13 shows γ-ray yield in the vicinity of the p-wave resonance according to the spin state of incident neutrons after background subtraction. As a result, the value of the transverse asymmetry $A_{\mathrm{LR}}^{\mathrm{inc}}$ for inclusive γ-ray transitions was zero consistent in all measurements.

Single γ-ray transition

The asymmetry for a single γ-ray transition was evaluated by applying the same procedure. In Fig.4.14, the peak at $E_\gamma = 5161$ keV is the transition from the compound state of $^{139}\mathrm{La} + n$ to the ground state of $^{140}\mathrm{La}$ (spin of the final state: $F = 3$). This 5161 keV transition is the highest energy transition from p-wave resonance in the $^{139}\mathrm{La}(n, \gamma)$ reaction and free from the background induced from the same reactions [30]. The gate range was full width at quarter maximum (FWQM) of the full-absorption peak of the 5161 keV. The neutron energy dependence of the asymmetry for the 5161 keV single γ-ray transition was evaluated. As shown in Fig.4.15, it was confirmed that the value of the transverse asymmetry $A_{\mathrm{LR}}^{\mathrm{all,gnd}}$ for the 5161 keV single γ-ray transition before the background subtraction was zero in the region outside of the p-wave resonance. The asymmetry was evaluated focusing on the p-wave region. The s-wave component was evaluated by fitting linear functions with 1100 μs $\leqslant t^m \leqslant$ 1600 μs, 1900 μs $\leqslant t^m \leqslant$ 3300 μs and subtracted as shown Fig.4.16. Figure 4.17 shows γ-ray yield in the vicinity of the p-wave resonance according to the spin state of incident neutrons after background subtraction and the transverse asymmetry TOF spectrum. As a result, the value of the transverse asymmetry for 5161 keV single γ-ray transition was a statistically significant value in all measurements. Finally, the results obtained for each measurement are shown in Table 4.2, where $\bar{P}_{\mathrm{He}}$ represents the average ^{3}He polarization ratio during the measurement.

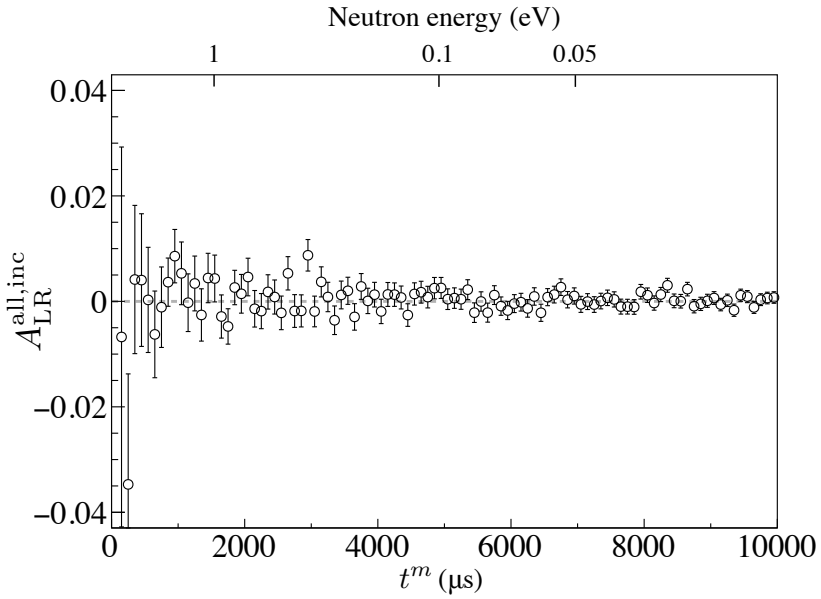

Figure 4.11: Asymmetry for the entire region when the threshold of the γ-ray was set to 2000 keV – 15000 keV.

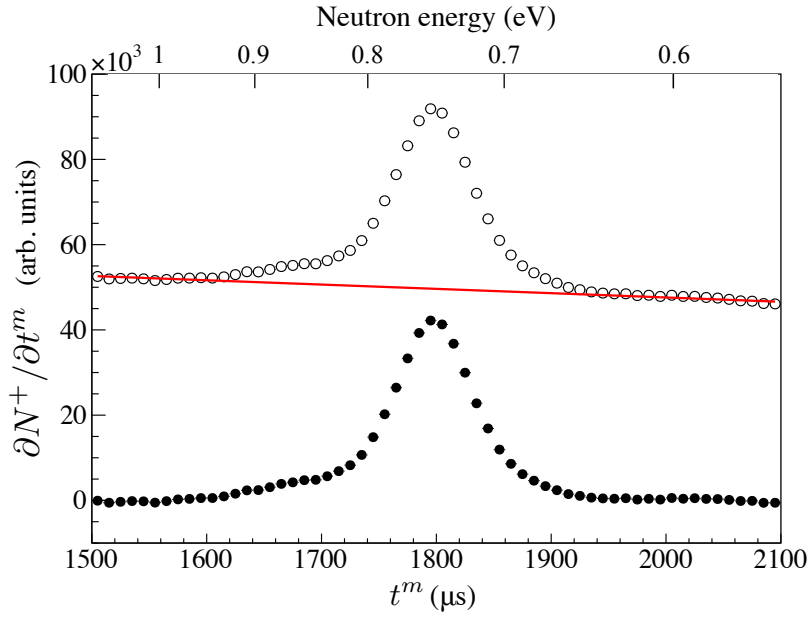

Figure 4.12: γ-ray yield in the vicinity of the p-wave resonance when the threshold of the γ-ray was set to 2000 keV – 15000 keV. White points show the γ-ray yield in the vicinity of the p-wave resonance for up-polarized neutrons. The solid line shows fitting results to background. Black points indicate p-wave components after subtraction of background. The small bump around $t^m \sim 1700$ μs is a result of the resonance of ^{149}Sm.

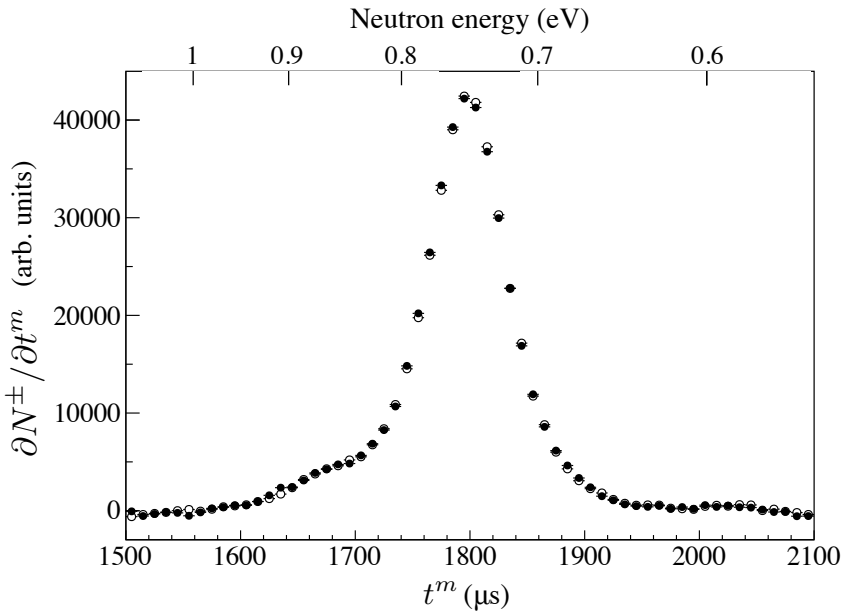

Figure 4.13: γ-ray yield in the vicinity of the p-wave resonance for each polarization direction of incident neutrons. White and black points indicate the up- and down- polarization, respectively.

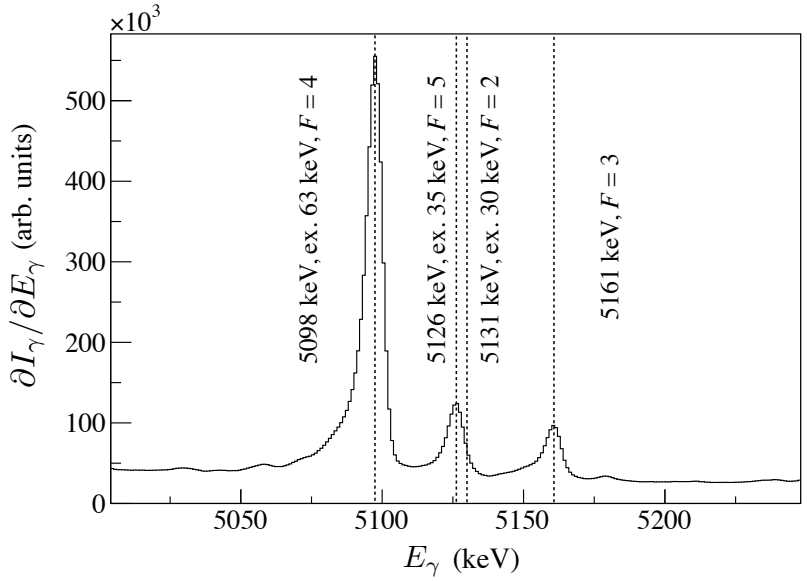

Figure 4.14: Pulse-height spectrum of γ-ray from ^{139}La(n, γ) reaction, in particular, a detailed drawing around 5161 keV. Only the 5161 keV peak was used in this analysis.

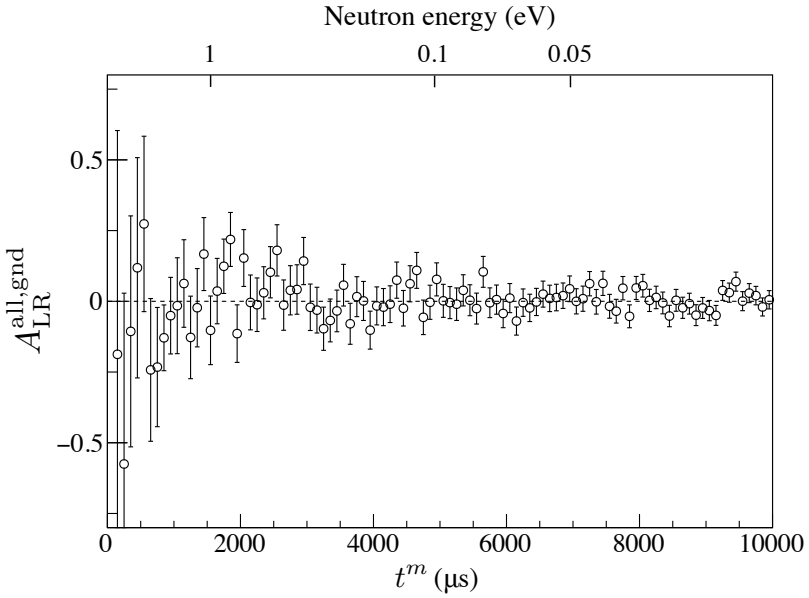

Figure 4.15: Asymmetry for the entire region for the 5161 keV single γ-ray transition.

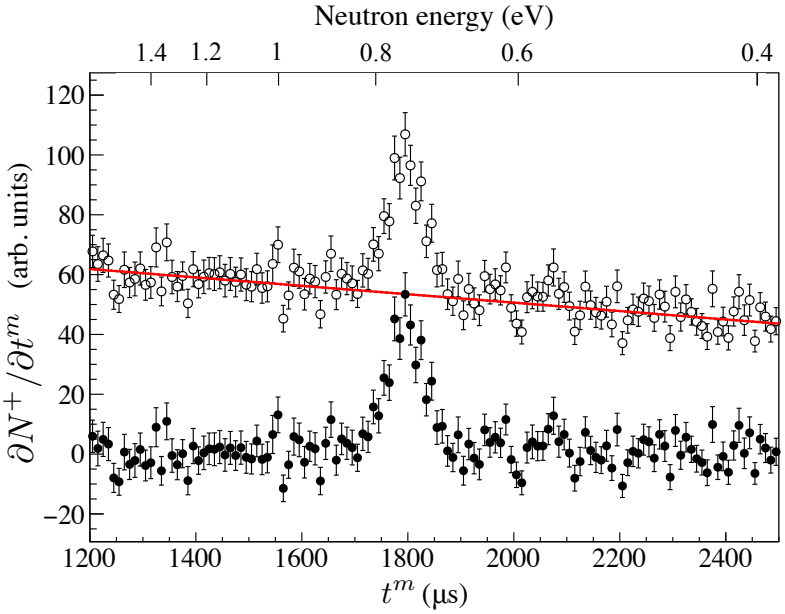

Figure 4.16: γ-ray yield in the vicinity of the p-wave resonance for up-polarized neutrons. White points show the γ-ray yield in the vicinity of the p-wave resonance for up-polarized neutrons. The solid line shows the result of fitting to background. Black points indicate p-wave components after subtraction of background.

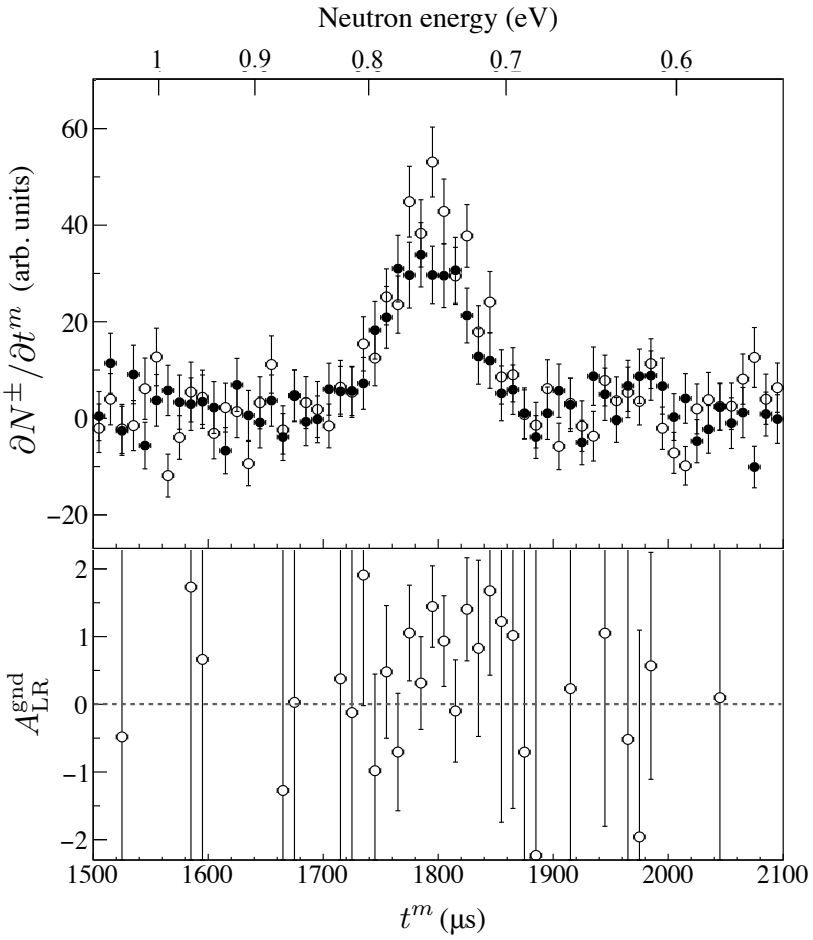

Figure 4.17: γ-ray yield in the vicinity of the p-wave resonance for each polarization direction of incident neutrons and the transverse asymmetry TOF spectrum. In the upper side figure, white and black points indicate the up- and down- polarization, respectively.

Chapter 5

Analysis

In this chapter, the experimental results obtained in the previous chapter are analyzed using the *sp*-mixing model. In addition, a combined analysis was carried out using the results of a previous study.

5.1 Analysis of $^{139}\mathrm{La}(\vec{n},\gamma)$ reaction using *sp*-mixing model

5.1.1 a_2 term analysis

The result of the asymmetry given by Table 4.2 was interpreted using the *sp*-mixing model, in which the differential cross section for a compound nuclear reaction induced by up- and down-spin neutrons $\frac{d\sigma^{\pm}_{n\gamma}(\theta,\varphi)}{d\Omega}$ can be written as,

$$\begin{aligned}\frac{d\sigma^{\pm}_{n\gamma}(\theta,\varphi)}{d\Omega} = \frac{1}{2} \quad \times \quad & \Bigg(a_0 + a_1\cos\theta + a_3\left(\cos^2\theta - \frac{1}{3}\right) \\ \pm \quad & \Bigg(-a_2\sin\theta\sin\varphi - a_4\sin\theta\cos\theta\sin\varphi \\ & +a_9\sin\theta\cos\varphi + a_{11}\sin\theta\cos\theta\cos\varphi\Bigg)\Bigg), \end{aligned} \tag{5.1}$$

where the definition of θ, φ follows Fig.2.8. The a_0 term consists of the s-wave (a_{0s}) and the p-wave (a_{0p}), respectively ($a_0 = a_{0s} + a_{0p}$).

The differential cross section $\frac{d\sigma^{\pm}_{n\gamma}(\theta,\varphi)}{d\Omega}$ without the s-wave component of the cross section $\frac{d\sigma^{\pm}_{n\gamma,p}(\theta,\varphi)}{d\Omega}$ is described as

$$\begin{aligned}\frac{d\sigma^{\pm}_{n\gamma,p}(\theta,\varphi)}{d\Omega} = \frac{a_{0p}}{2} \quad &\times \quad \left(1 + A_1\cos\theta + A_3\left(\cos^2\theta - \frac{1}{3}\right)\right. \\ &\pm \quad \left(-A_2\sin\theta\sin\varphi - A_4\sin\theta\cos\theta\sin\varphi\right. \\ &\qquad \left.\left. + A_9\sin\theta\cos\varphi + A_{11}\sin\theta\cos\theta\cos\varphi\right)\right), \end{aligned} \tag{5.2}$$

where

$$\begin{aligned} A_1 &= \frac{a_1}{a_{0p}}, \quad A_2 = \frac{a_2}{a_{0p}}, \quad A_3 = \frac{a_3}{a_{0p}}, \\ A_4 &= \frac{a_4}{a_{0p}}, \quad A_9 = \frac{a_9}{a_{0p}}, \quad A_{11} = \frac{a_{11}}{a_{0p}}. \end{aligned} \tag{5.3}$$

Generally, the resonance curve obtained by the (n,γ) reaction is broadened by the thermal motion of target nucleus, and the resonance energy shifts by the time structure of the incident neutron beam. As shown in Fig.5.1, the A_2 term satisfies the following relationship because a_{0p} and a_2 have the same energy dependence in the vicinity of the p-wave resonance.

$$\begin{aligned} A_2 &= \frac{a_2 * R_{\rm dop}(t^m) * R_{\rm mod}(t^m)}{a_{0p} * R_{\rm dop}(t^m) * R_{\rm mod}(t^m)} \\ &= \frac{a_2}{a_{0p}}, \end{aligned} \tag{5.4}$$

where $R_{\rm dop}(t^m)$ and $R_{\rm mod}(t^m)$ are the response function of the resonance width broadening due to thermal motion of target nucleus and time structure of neutron beam due to the moderation process. Therefore, the effects on these resonance structures are canceled, and A_2 is found to be a constant in the vicinity of the p-wave resonance.

The asymmetry $A_{+-,p}$ for the γ-ray yield for neutron spin in the p-wave resonance region after subtraction of the s-wave resonance component is given as

$$\begin{aligned} A_{+-,p} &= \frac{\int d\Omega \int dE_n \sigma^{+}_{n\gamma,p}(\theta,\varphi) - \int d\Omega \int dE_n \sigma^{-}_{n\gamma,p}(\theta,\varphi)}{\int d\Omega \int dE_n \sigma^{+}_{n\gamma,p}(\theta,\varphi) + \int d\Omega \int dE_n \sigma^{-}_{n\gamma,p}(\theta,\varphi)} \\ &= \frac{-\bar{A}_2\sin\theta\sin\varphi - \bar{A}_4\sin\theta\cos\theta\sin\varphi + \bar{A}_{11}\sin\theta\cos\theta\cos\varphi}{1 + \bar{A}_3\left(\cos^2\theta - \frac{1}{3}\right)}, \end{aligned} \tag{5.5}$$

where $\bar{A}_i$ is the integrated value of A_i. The integral region was defined as the total width of the resonance centered on the resonance ($E_p - 2\Gamma_p \leqslant E_n \leqslant E_p + 2\Gamma_p$). The effect of A_1 and A_9 are sufficient small upon integration, because they are both odd functions of energy centered at

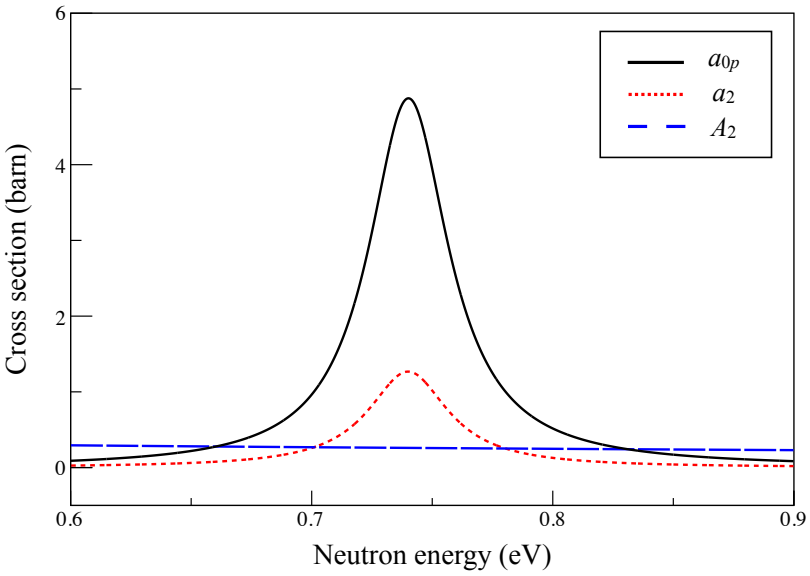

Figure 5.1: Energy dependence of the a_{0p}, a_2, and A_2 terms. The a_{0p} and a_2 terms have the same energy dependence in the vicinity of the p-wave resonance.

the p-wave resonance. A_4 and A_{11} are canceled when the geometric configuration of the γ-ray detectors satisfies symmetrical relations with respect to the x and z axis, respectively. The A_3 term was evaluated by a previous study [30] and found to be

$$\bar{A}_3 = 0.568 \pm 0.083. \tag{5.6}$$

Further, the definition and value of B_3 for $\theta = 0^\circ$ are given by

$$\begin{aligned} B_3 &\equiv 1 + \bar{A}_3 \left(\cos^2\theta - \frac{1}{3} \right) \\ &= 0.812 \pm 0.028. \end{aligned} \tag{5.7}$$

It follows that $A_{+-,p}$ has the following relationship,

$$\begin{aligned} A_{+-,p} \times B_3 &= -\bar{A}_2 \sin\theta \sin\varphi \\ &= \frac{\Gamma_p}{E_p - E_{s1}} \sqrt{\frac{\Gamma^n_{s1}}{\Gamma^n_p}} \sqrt{\frac{\Gamma^\gamma_{s1,\mathrm{gnd}}}{\Gamma^\gamma_{p,\mathrm{gnd}}}} \\ &\quad \times \left(-\frac{5}{8} \cos\phi_p - \frac{\sqrt{35}}{16} \sin\phi_p \right) \sin\theta \sin\varphi \\ &= -\left(0.719 \cos\phi_p + 0.418 \sin\phi_p \right) \sin\theta \sin\varphi. \end{aligned} \tag{5.8}$$

Table 5.1: Ratios of the γ width from each resonance to the corresponding ground state [30].

$\frac{\Gamma^{\gamma}_{s1,\mathrm{gnd}}}{\Gamma^{\gamma}_{s1}}$	:	$\frac{\Gamma^{\gamma}_{p,\mathrm{gnd}}}{\Gamma^{\gamma}_{p}}$	:	$\frac{\Gamma^{\gamma}_{s2,\mathrm{gnd}}}{\Gamma^{\gamma}_{s2}}$
1	:	0.796 ± 0.020	:	0.009 ± 0.006

The partial γ width used in the analysis is shown in Table 5.1. The measurement result $A_{\mathrm{LR}}^{\mathrm{gnd}}$ in the previous chapter and $A_{+-,p}$ in the theoretical calculation are equivalent. Therefore, the left side of Eq.5.8 gives the following values from Eq.5.7 and value of the $A_{\mathrm{LR}}^{\mathrm{gnd}}$,

$$A_{+-,p} \times B_3 = 0.59 \pm 0.12. \tag{5.9}$$

The following results are obtained by solving Eq.5.8 for ϕ_p,

$$\phi_p = \left(-14.5^{+13.1}_{-10.9}\right)^{\circ}, \quad \left(75.0^{+10.8}_{-13.4}\right)^{\circ}. \tag{5.10}$$

The value of x corresponding to ϕ_p is then

$$x = 0.97^{+0.06}_{-0.03}, \quad 0.26^{+0.22}_{-0.19}. \tag{5.11}$$

The above result is shown in Fig.5.2 in the xy plane. From these values of x, the value of W is determined using Eq.2.7.

$$W = \left(-2.17^{+0.16}_{-0.07}\right)\,\mathrm{meV}, \quad \left(-8.12^{+3.70}_{-20.7}\right)\,\mathrm{meV}. \tag{5.12}$$

Further, the value of $\kappa(J)$ from the value of ϕ_p is obtained as follows from Eq.2.20.

$$\kappa(J) = 0.61^{+0.17}_{-0.14}, \quad 3.22^{+6.53}_{-1.24}. \tag{5.13}$$

The restricted region of $|\kappa(J)|$ is shown in Fig.5.3.

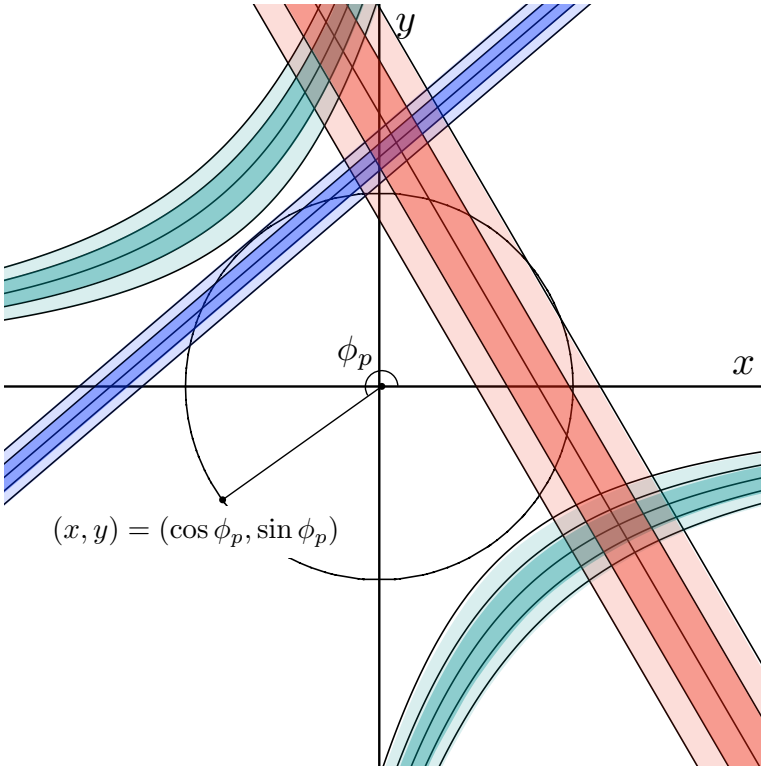

Figure 5.2: The limit region of ϕ_p on the xy-plane is obtained by measurements. Blue, red, and green regions represent the a_1, a_2, and a_3 terms, respectively. The dark color region represents the 1σ region, and the light color region represents the 2σ region.

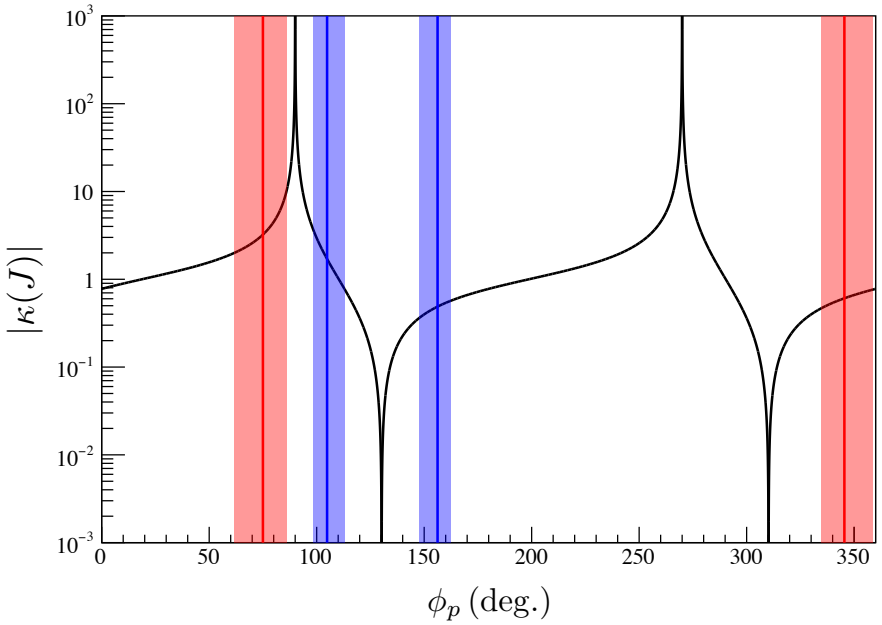

Figure 5.3: Value of $|\kappa(J)|$ as a function of ϕ_p. Blue and red regions represent the a_1 and a_2 terms results, respectively. The dark colored region represents the 1σ region.

5.1.2 Combined analysis integrating the results of previous studies

The same discussion as above is analyzed by integrating the measurement results of previous studies. Values of ϕ_p were limited by determination of a_1 and a_3 by measurement of angular distribution of (n, γ) reaction in a previous study [30]. As shown in Fig.5.4, each measurement limits the value of ϕ_p in the xy-plane. By multiplying the probability distributions in each measurement, we obtain a probability distribution derived from the three results shown in Fig.5.5. Then, considering the probability distribution on the unit circle, the distribution is as shown in Fig.5.6, and the region of the 95% confidence level is obtained as follows,

$$\phi_p = \left(105.4^{+9.1}_{-7.9}\right)^\circ . \tag{5.14}$$

The value of x corresponding to ϕ_p is then

$$x = -0.26^{+0.13}_{-0.15}. \tag{5.15}$$

The above result is shown in Fig.5.2 in the xy plane. From these values of x, the value of W is determined from the Eq.2.7.

$$W = \left(7.94^{+8.17}_{-2.85}\right) \text{meV}. \tag{5.16}$$

Further, the value of $\kappa(J)$ from the value of ϕ_p is obtained as follows from Eq.2.20.

$$\kappa(J) = 1.62^{+2.60}_{-0.95}. \tag{5.17}$$

The restricted region of $|\kappa(J)|$ is obtained by a combined analysis and shown in Fig.5.7.

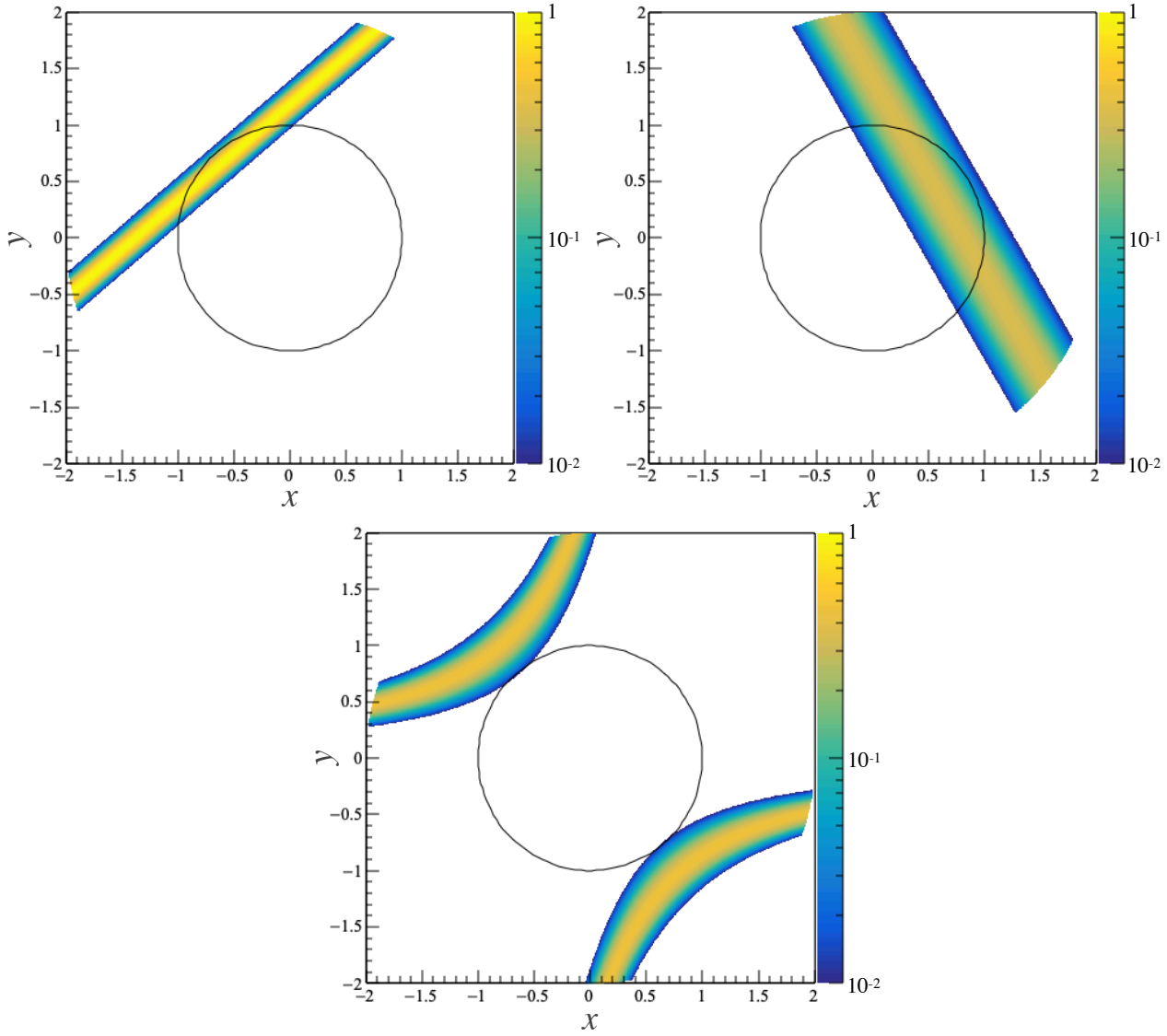

Figure 5.4: Determined range of ϕ_p on the xy-plane by correlation term measurement. The upper left shows the result of a_1, the upper right shows the result of a_2, the lower center shows the result of a_3, respectively [30].

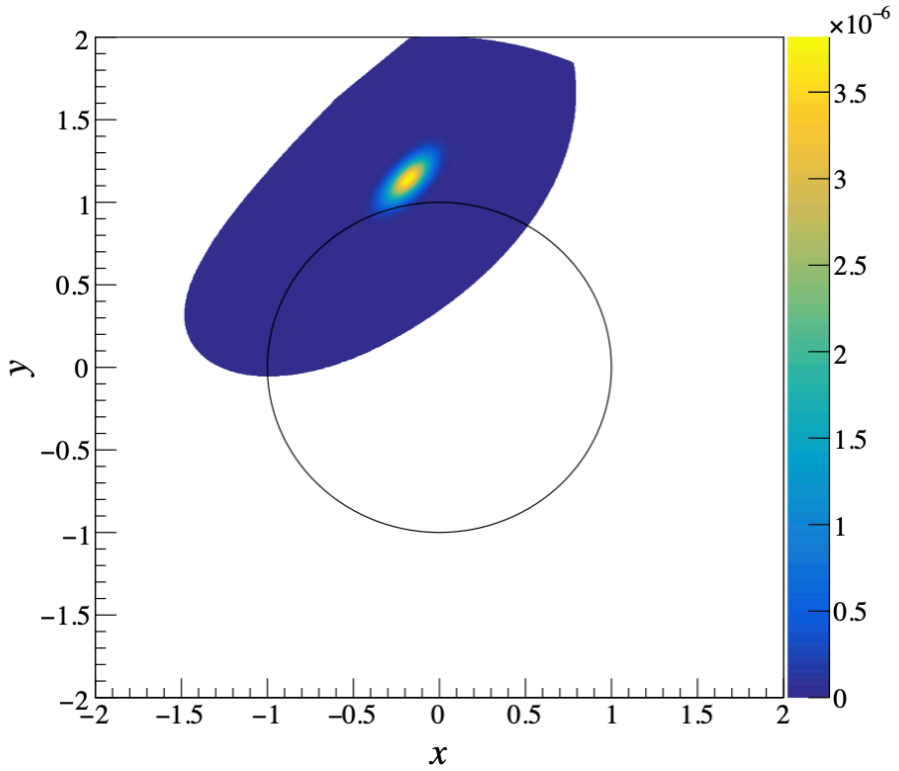

Figure 5.5: Visualization of the value of ϕ_p on the xy-plane by the combined analysis

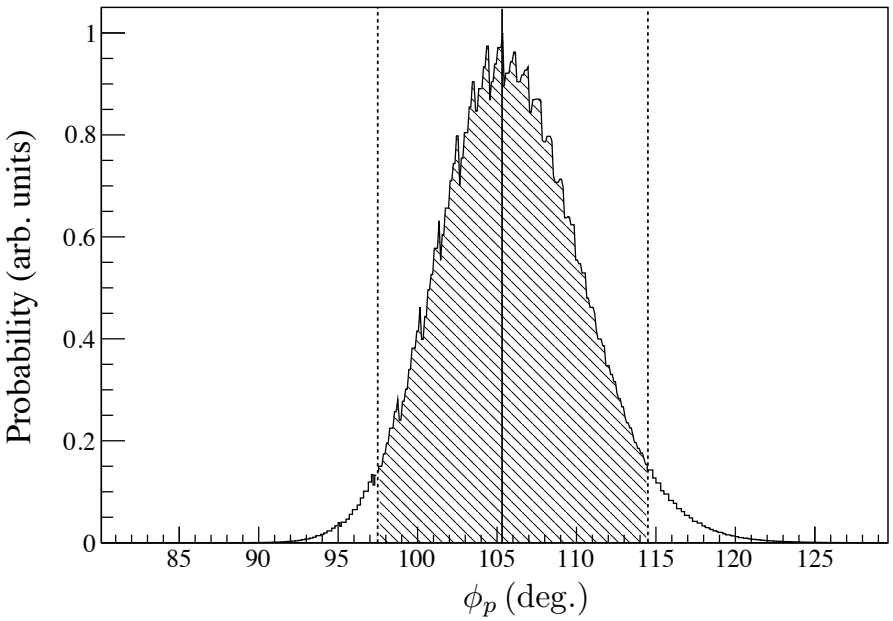

Figure 5.6: Probability distribution of ϕ_p on a unit circle by the combined analysis

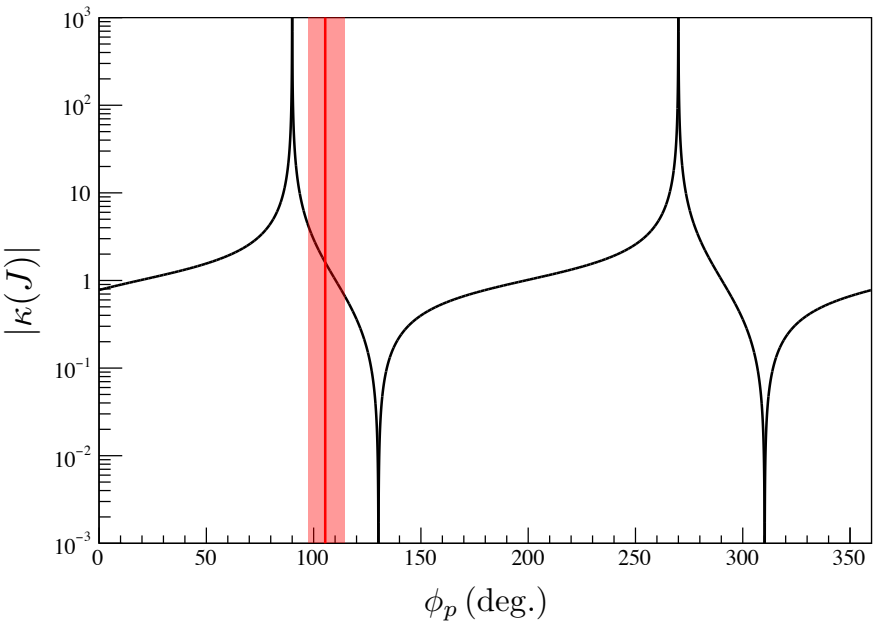

Figure 5.7: Value of $|\kappa(J)|$ as a function of ϕ_p by the combined analysis

Chapter 6

Discussion

6.1 Interpretation of $(\vec{n}, \gamma)$ reaction correlation measurements

In the previous chapter, the author tried to determine a single ϕ_p region by the combined analysis of measurement results. However, it is also true that there is the discrepancy of approximately $3\,\sigma$ between each measurement result. It is not possible to conclude whether this discrepancy is due to experimental uncertainty or to the incompleteness of the *sp*-mixing model. For example, in the *sp*-mixing model, it is assumed that the mixing occurs only in the entrance channel and no mixing occurs in the exit channel. However, there are few examples in which this was confirmed experimentally [71]. Under such circumstances, it is important not only to carry out further high-precision measurements, but also to give restrictions to ϕ_p multilaterally by different measurements or analysis. Specifically, the measurement of a_6 and a_{13} terms become possible by measuring the circular polarization of γ rays in the $(n, \vec{\gamma})$ reaction. The coherency of the exit channel can be discussed by studying in detail the final state dependence of the (n, γ) reaction. In addition, if the target can be polarized, ϕ_p can be also accessed by measuring the pseudo-magnetic rotation described in the later section [72].

6.2 Estimation of the sensitivity for the T-violation search

In this section, the results obtained by combined analyses are used to discuss quantitatively the search for T-violation.

6.2.1 Estimation of experimental sensitivity

The T-violating cross section in the transmission measurement may be described using EFT as in Eq.1.9. The P-violating cross section $\Delta\sigma_{\not P}$ in neutron-deuteron scattering may also be described using the Desplanques, Donoghue, Holstein (DDH) model as follows [29].

$$\frac{\Delta\sigma_{\not P}}{2\sigma_{\rm tot}} \simeq \frac{(0.395\ \text{b})}{2\sigma_{\rm tot}} h_\pi^1, \tag{6.1}$$

where h_π^1 is a P-violating pion nucleon coupling constant. The ratio of the T-violating weak matrix element to the P-violating weak matrix element can be obtained by taking the ratio of Eq.1.9 to Eq.6.1.

$$\frac{W_{\rm T}}{W} = \frac{\Delta\sigma_{\not T\not P}}{\Delta\sigma_{\not P}} \simeq (-0.47)\left[\frac{\bar{g}_\pi^{(0)}}{h_\pi^1} + (0.26)\frac{\bar{g}_\pi^{(1)}}{h_\pi^1}\right]. \tag{6.2}$$

Upper limits are given for $\bar{g}_\pi^{(0)}$ and $\bar{g}_\pi^{(1)}$ from nEDM and ^{199}Hg atomic EDM measurements, respectively [73, 74].

$$\bar{g}_\pi^{(0)} < 1.6 \times 10^{-10}, \quad \bar{g}_\pi^{(1)} < 0.5 \times 10^{-11}. \tag{6.3}$$

The value of h_π^1 utilizes the limitations of the DDH coupling constants by various experiments shown in Fig.6.1. Although the experimental result of ^{18}F gives a smaller value than the $\vec{n}p$ measurement [38], considering the complexity of the system, we adopt the result of $\vec{n}p$ measurement, which is a simple few-body system, in this estimation.

$$h_\pi^1 = (2.6 \pm 1.2_{\rm stat} \pm 0.2_{\rm sys}) \times 10^{-7}. \tag{6.4}$$

Thus, the $W_{\rm T}/W$ is restricted as follows,

$$\left|\frac{W_{\rm T}}{W}\right| < 2.9 \times 10^{-4}. \tag{6.5}$$

Substitution in Eq.2.20 gives the following relationship,

$$|\Delta\sigma_{\rm T}| < 1.4 \times 10^{-4}\ \text{barn}, \tag{6.6}$$

where the values of $\kappa(J)$ and $\Delta\sigma_{\rm P}$ are 1.6 and 0.3 barn, respectively.

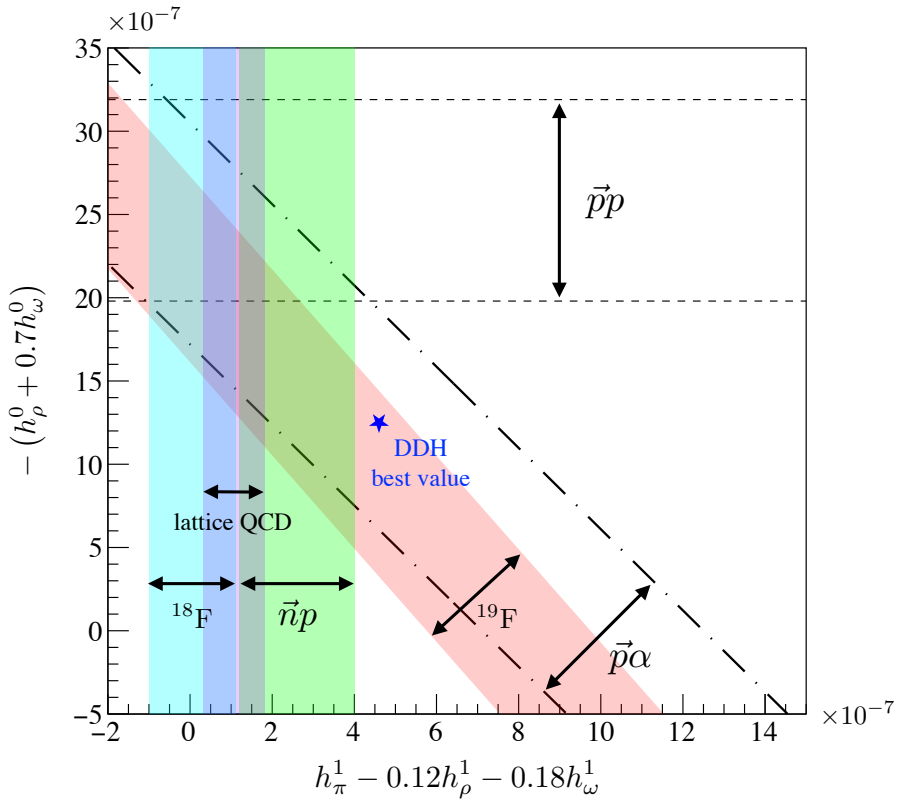

Figure 6.1: Experimental constraints on isoscalar and isovector DDH couplings. Limitations from five experimental results are shown: $\vec{p}p$, $\vec{p}\alpha$, $\vec{n}p$, ^{18}F, and ^{19}F [75–77]. The DDH best value point is indicated by a blue star and limiting regions by lattice QCD are indicated by blue bands [29, 78].

6.2.2 Estimation of statistical reach of experiment

The author discusses from a statistical point of view the optimum thickness of the nuclear target and the measurement time required to reach the upper limit of nEDM discussed in the previous section. First, the measurement of P_x is discussed. When unpolarized neutrons are injected into a polarized nuclear target as shown in Fig.6.2, the number of neutrons with positive and negative spin $N_{\mathrm{P}_\pm}$ can be described as follows,

$$N_{\mathrm{P}_\pm} = Ne^{-O_\mathrm{t}}e^{-O_\mathrm{He}}\left[\cosh\left(P_\mathrm{He}O'_\mathrm{He}\right) \mp P_x \sinh\left(P_\mathrm{He}O'_\mathrm{He}\right)\right], \tag{6.7}$$

where N is the number of incident neutrons, O_t, O_He, and O'_He are defined as follows,

$$O_\mathrm{t} \equiv n_\mathrm{t}t_\mathrm{t}\sigma_\mathrm{t}, \quad O_\mathrm{He} \equiv n_\mathrm{He}t_\mathrm{He}\sigma_\mathrm{He}, \quad O'_\mathrm{He} \equiv n_\mathrm{He}t_\mathrm{He}\Delta\sigma_\mathrm{He}, \tag{6.8}$$

where n_t is number density of the target, t_t is thickness of the target and σ_t is the total cross section of the target nucleus. Therefore, the sum of the counts N' of different spin components can be described as follows,

$$N_{\mathrm{P}_+} + N_{\mathrm{P}_-} = N' = 2Ne^{-O_\mathrm{t}}e^{-O_\mathrm{He}}\cosh\left(P_\mathrm{He}O'_\mathrm{He}\right). \tag{6.9}$$

Assuming that the neutron transmittance T_unpol for the nuclear target and the unpolarized ^{3}He spin analyzer are known as follows (Here, it is assumed that the contribution of the change in neutron transmittance according to the polarization of the nuclear target is negligibly small.),

$$T_\mathrm{unpol} = e^{-O_\mathrm{t}}e^{-O_\mathrm{He}}. \tag{6.10}$$

The neutron transmittance T_pol when the ^{3}He spin analyzer is polarized can then be described as follows,

$$T_\mathrm{pol} = \frac{N'}{2N} = T_\mathrm{unpol}\cosh\left(P_\mathrm{He}O'_\mathrm{He}\right). \tag{6.11}$$

Therefore, P_x can be described as

$$P_x = \frac{N_{\mathrm{P}_+} - N_{\mathrm{P}_-}}{N_{\mathrm{P}_+} + N_{\mathrm{P}_-}} \frac{T_\mathrm{pol}}{\sqrt{T_\mathrm{pol}^2 - T_\mathrm{unpol}^2}}. \tag{6.12}$$

Next, in the A_x measurement, the incident neutron is polarized using the spin polarizer, and it is injected to the nuclear target as shown in Fig.6.2. The asymmetry of the count of transmitted neutrons $N_{\mathrm{A}_\pm}$ is taken according to the polarization direction of neutrons. The A_x

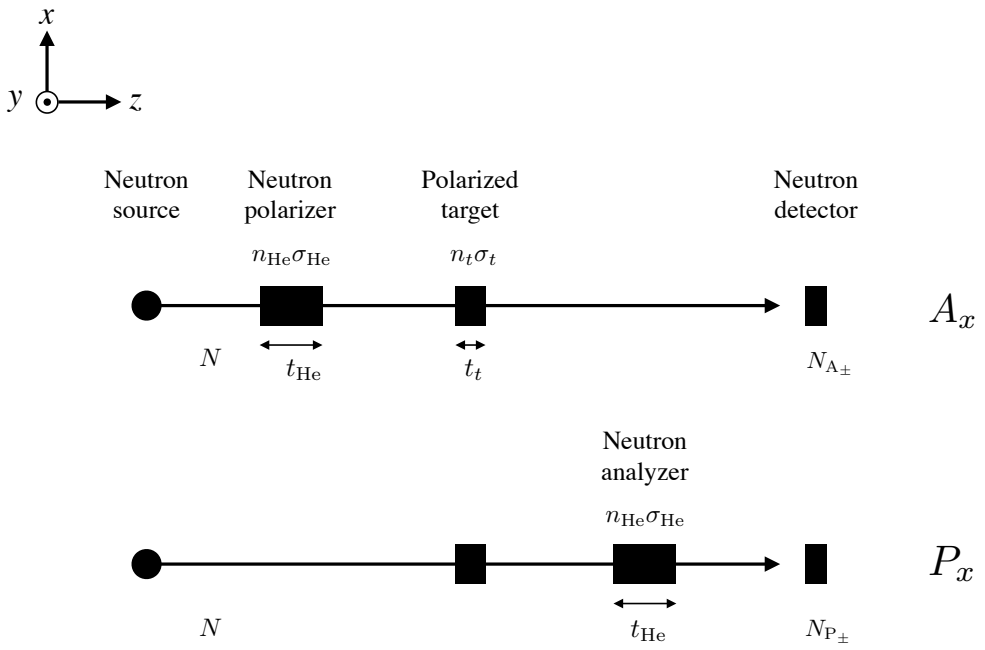

Figure 6.2: Top view of the concept of the experimental setup for the T-violation search for the measurement of A_x and P_x.

can be described as

$$A_x = \frac{N_{\mathrm{A}_+} - N_{\mathrm{A}_-}}{N_{\mathrm{A}_+} + N_{\mathrm{A}_-}}. \tag{6.13}$$

The statistical uncertainties of A_x and P_x in Eq.6.12 and Eq.6.13 can be described as

$$\begin{aligned} \Delta A_x &= \frac{2\sqrt{N_{A+}N_{A-}}}{(N_{A+}+N_{A-})^{3/2}} = \frac{1}{\sqrt{2NT_{\mathrm{pol}}}}, \\ \Delta P_x &= \frac{2\sqrt{N_{P+}N_{P-}}}{(N_{P+}+N_{P-})^{3/2}} \frac{T_{\mathrm{pol}}}{\sqrt{T_{\mathrm{pol}}^2 - T_{\mathrm{unpol}}^2}} = \frac{1}{\sqrt{2NT_{\mathrm{pol}}}} \frac{T_{\mathrm{pol}}}{\sqrt{T_{\mathrm{pol}}^2 - T_{\mathrm{unpol}}^2}}, \end{aligned} \tag{6.14}$$

where the following condition was used for the deformation of Eq.6.14,

$$N_{\mathrm{A}_+} = N_{\mathrm{A}_-} = N_{\mathrm{P}_+} = N_{\mathrm{P}_-} = NT_{\mathrm{pol}}. \tag{6.15}$$

Taking into account the neutron and target nuclear polarization of A_x and P_x in Eq.2.29 and 2.30, we can rewrite as follows,

$$\begin{aligned} A_x &= 4\left(P_n P_{\rm t}\frac{{\rm Re}\,A^*D}{|A|^2} + P_n^2 P_{\rm t}\frac{{\rm Im}\,B^*C}{|A|^2}\right), \\ P_x &= 4\left(P_n P_{\rm t}\frac{{\rm Re}\,A^*D}{|A|^2} - P_n^2 P_{\rm t}\frac{{\rm Im}\,B^*C}{|A|^2}\right), \\ A_x + P_x &= P_n P_{\rm t}\frac{8\,{\rm Re}\,A^*D}{|A|^2}, \end{aligned} \tag{6.16}$$

where P_n and $P_{\rm t}$ are the polarization ratio of the incident neutron and target nucleus. The following relationship is required for a 95% confidence level determination of $8\,{\rm Re}\,A^*D$ values through A_x and P_x measurements,

$$1.96\sqrt{\Delta {A_x}^2 + \Delta {P_x}^2} = P_n P_{\rm t}\frac{8\,{\rm Re}\,A^*D}{|A|^2}. \tag{6.17}$$

The following relational expression is obtained by substituting Eq.6.14 and applying equation deformation,

$$\frac{1}{\sqrt{N}} = P_n P_{\rm t}\frac{8\,{\rm Re}\,A^*D}{|A|^2}\sqrt{\frac{T_{\rm pol}^2 - T_{\rm unpol}^2}{2T_{\rm pol}^2 - T_{\rm unpol}^2}}\frac{\sqrt{2T_{\rm unpol}}}{1.96}. \tag{6.18}$$

Therefore, the optimum target thickness can be estimated by defining the right side of the above equation as the FOM. Figure 6.3 shows the thickness dependence of the FOM. The optimum thickness of the target is obtained by minimizing N in Eq.6.18 with a maximum at approximately 3.2 cm. Next, the optimum effective thickness of ^{3}He is estimated. In general, when determining the optimum effective thickness of ^{3}He for the neutron polarizer, the FOM is defined as FOM $\equiv P_n^2 T_n$. Figure 6.4 describes the neutron transmittance, polarization ratio and the FOM for 70% ^{3}He polarization and $E_n = 0.74$ eV. The optimum effective thickness of ^{3}He at 300 K is $n_{\rm He}t_{\rm He} = 72$ atm $\cdot$ cm. The time required for the T-violation search is estimated based on the optimized target thickness and the effective thickness of ^{3}He discussed above. The time required to measure the cross section equivalent to the upper limit of nEDM given in Eq.6.6 is given by Eq.6.3. Assuming that the experiment is carried out at the Port07 of J-PARC MLF as shown in Fig.6.5, the neutron flux spectrum at the Port07 is estimated as shown in Fig.6.6 by Monte-Carlo simulation when the proton power is 1 MW. We assume that the target with cross-sectional area of 4×4 cm^2 is located 15 m from the moderator surface. In this case, the flux of neutrons irradiated to the target is 1.8×10^7 n/s at 0.74 ± 0.05 eV. Therefore, the measurement time required for the target polarization ratio and the ^{3}He polarization ratio is estimated as shown in Fig.6.7. Assuming the ideal case where ^{3}He and the nucleus are perfectly polarized

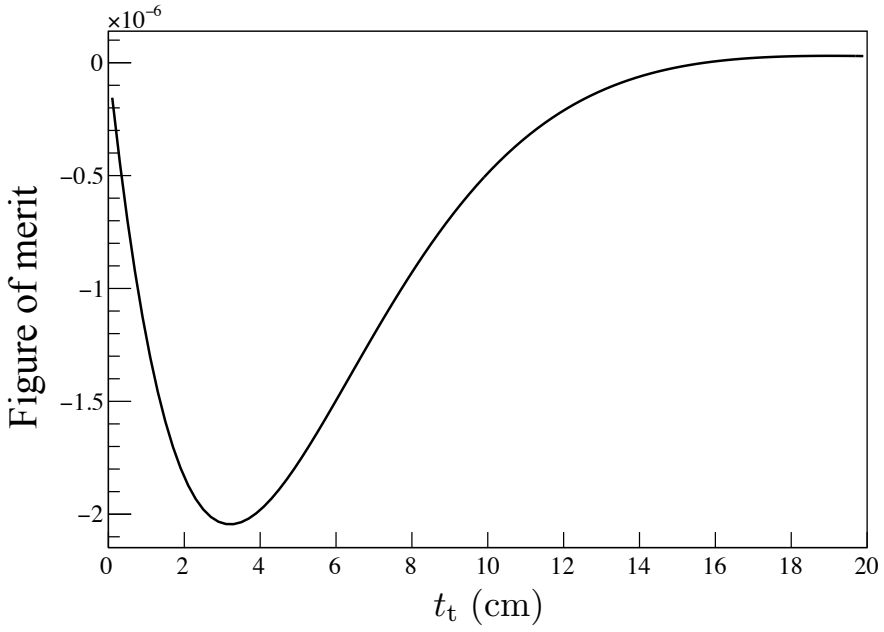

Figure 6.3: Target thickness dependence of the FOM. The FOM defined in Eq.6.18 has extremal value at $t_t = 3.2$ cm, therefore the optimum thickness of the target is 3.2 cm.

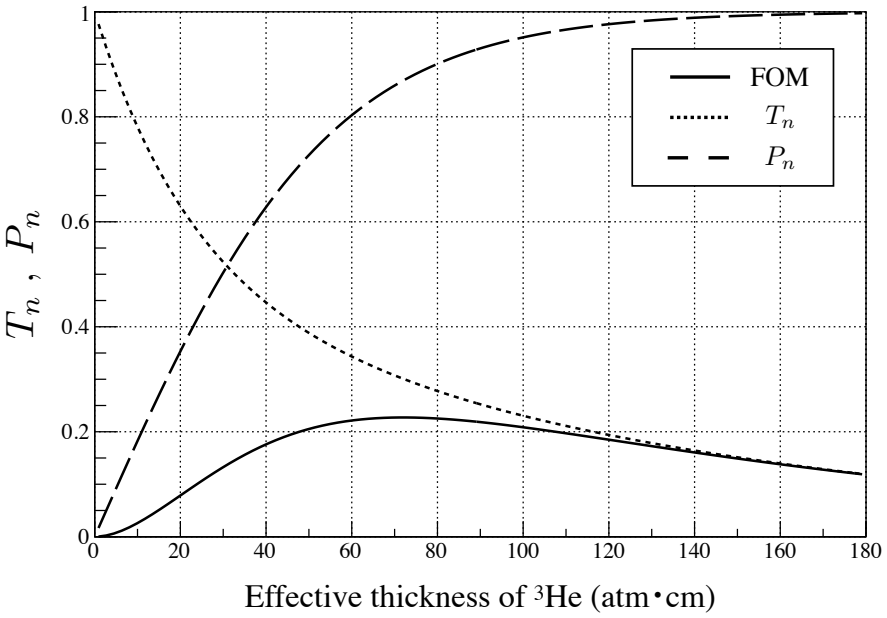

Figure 6.4: Effective thickness of ^{3}He dependence on transmittance, polarization, and FOM. When the polarization ratio of ^{3}He is 70%, the FOM has a maximum at $n_{\mathrm{He}} t_{\mathrm{He}} = 72$ atm $\cdot$ cm which is the optimum thickness.

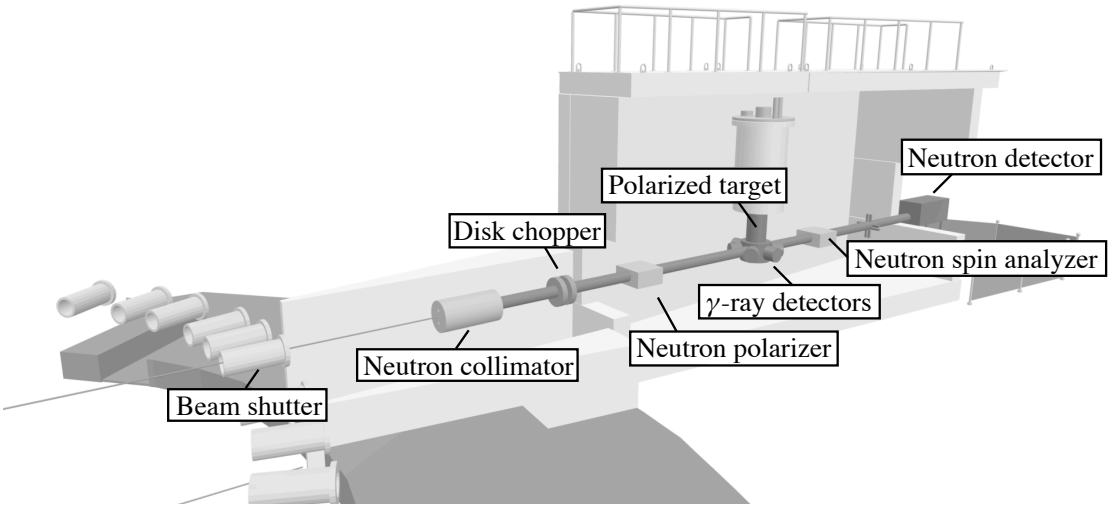

Figure 6.5: 3D view of the experimental setup for the T-violation search created by Dr. Morishima.

and suppression factor $|\sin\beta/\beta| \sim 1$ (discussed in detail in later chapters as "pseudomagnetic field"), the time required is estimated to be approximately half a day. On the other hand, assuming the real case where the target nuclear polarization ratio is 40%, the polarization ratio of ^{3}He is 70%, the suppression factor is also approximately 1 as a realistic case which can be achieved by the present technology, the time required is estimated to be approximately 10 days. In addition, the measurement time dependence of the T-violation search for the value of ϕ_p is shown in Fig.6.8.

6.2.3 Method for determining higher order tensor polarization component

In the discussion of the experimental sensitivity in the previous section, it was sufficient to consider the leading term of the forward scattering amplitude (only the vector polarized component). In practice, however, the nuclear spin of ^{139}La is 7/2 and has a higher order tensor polarization component. Therefore, it is necessary to separate the false T-violation signal caused by the higher order tensor polarization component, and they are determined by measuring the correlation terms.

Equation 2.25 describes the forward scattering amplitude for a nuclear target with spin 1/2. The forward scattering amplitude for a target with a nuclear spin of 7/2 can be described as [79]

$$f = \alpha + \boldsymbol{\sigma} \cdot \boldsymbol{\beta}, \tag{6.19}$$

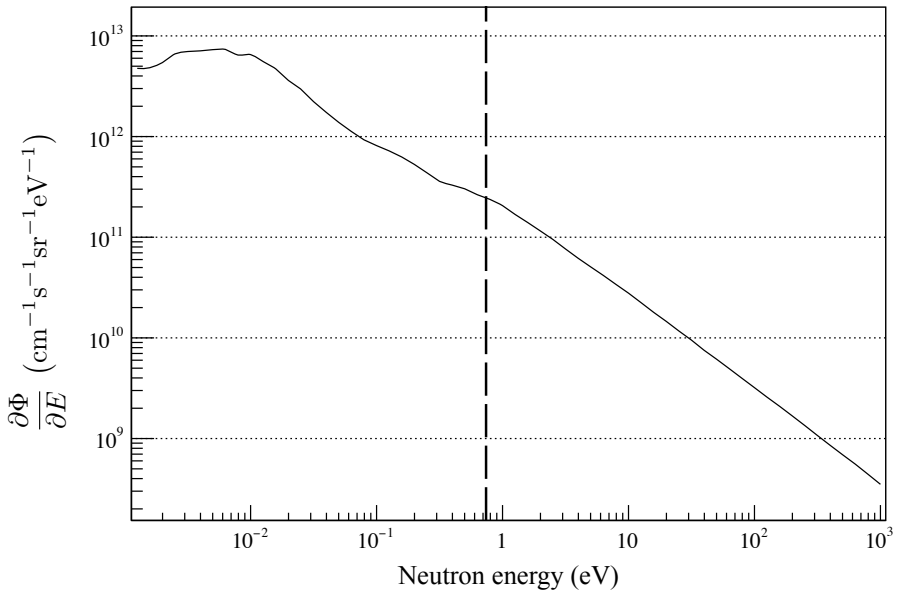

Figure 6.6: Time-integrated intensity on the moderator for the Port07 (coupled moderator). The dashed line shows the 0.74 eV region [53]

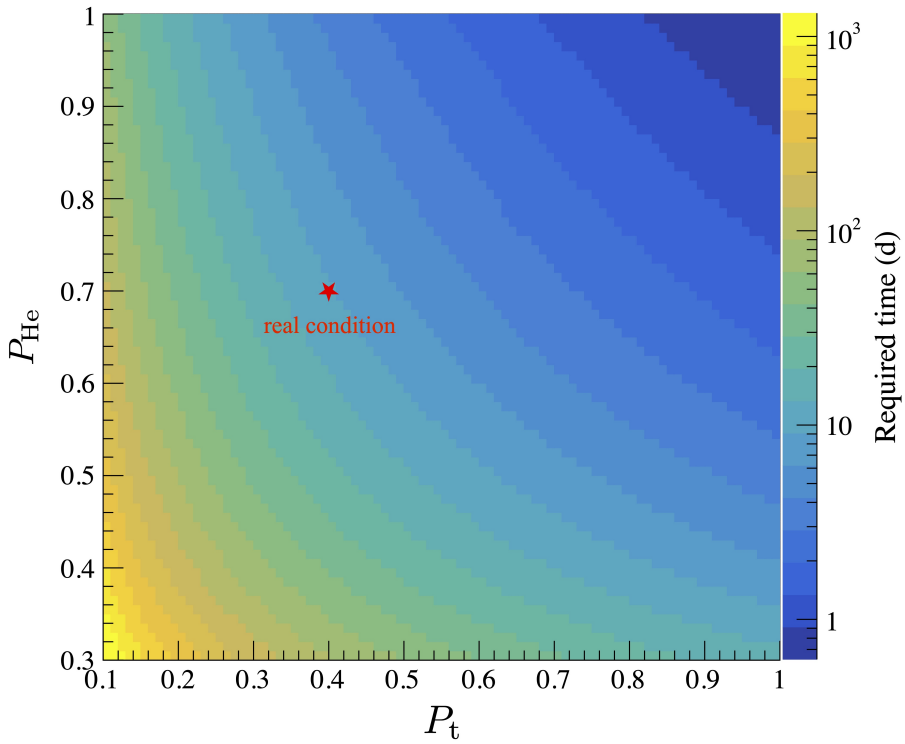

Figure 6.7: Polarization dependence of the time taken to reach the T-violation search region equivalent to nEDM assuming $\kappa(J) = 1.6$. The values realistically achievable with current techniques are shown by red stars.

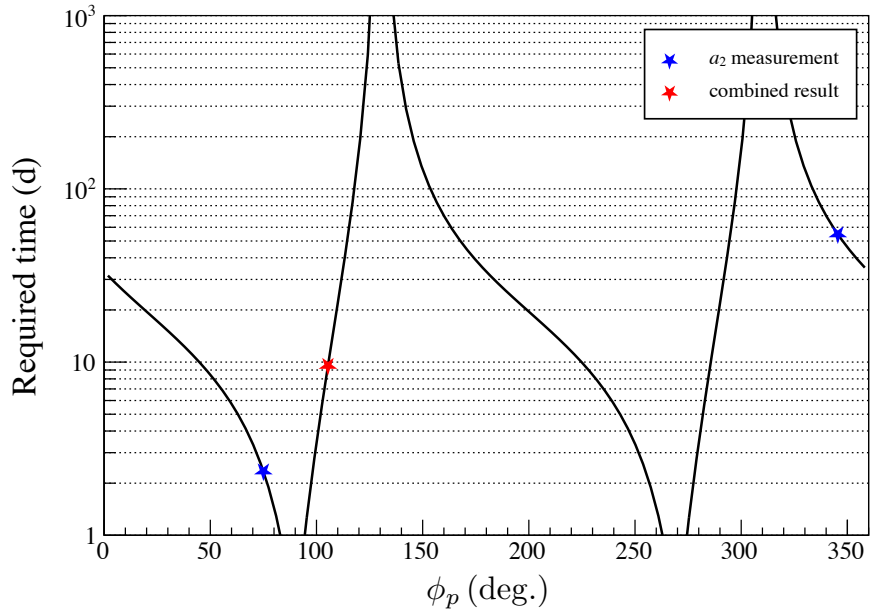

Figure 6.8: ϕ_p dependence of measurement time for the T-violation search. The star marks indicate the center value of each analysis result. Red indicates the case of the combined analysis and blue one indicates the case of the a_2 measurement. The polarization of ^{3}He and nuclear target are assumed to be 0.7 and 0.4 ("real condition"), respectively.

where α and β are respectively expressed as follows.

$$
\begin{aligned}
\alpha &= A' + P_1 H' \left(\hat{\boldsymbol{k}}_n \cdot \hat{\boldsymbol{I}}\right) + P_2 E' \left(\left(\hat{\boldsymbol{k}}_n \cdot \hat{\boldsymbol{I}}\right)^2 - \frac{1}{3}\right) \\
\boldsymbol{\beta} &= \left(C' + P_1 K' \left(\hat{\boldsymbol{k}}_n \cdot \hat{\boldsymbol{I}}\right) - \frac{1}{3} P_2 F' + \frac{2}{3} P_3 B'_3 \left(\hat{\boldsymbol{k}}_n \cdot \hat{\boldsymbol{I}}\right)\right) \hat{\boldsymbol{k}}_n \\
&\quad + \left(P_1 B' + P_2 F' \left(\hat{\boldsymbol{k}}_n \cdot \hat{\boldsymbol{I}}\right) - \frac{1}{3} P_3 B'_3 \left(1 - \left(\hat{\boldsymbol{k}}_n \cdot \hat{\boldsymbol{I}}\right)^2\right)\right) \hat{\boldsymbol{I}} \\
&\quad + \left(P_1 D' + P_2 G' \left(\hat{\boldsymbol{k}}_n \cdot \hat{\boldsymbol{I}}\right)\right) \left(\hat{\boldsymbol{k}}_n \times \hat{\boldsymbol{I}}\right),
\end{aligned}
\tag{6.20}
$$

where P_i is the spherical-tensor polarization of the i-th rank, and coefficients in the amplitude for ^{139}La are the following: In this case also, the following relationship is obtained using the density matrix $\mathfrak{S}$ defined in Eq.2.27,

$$
\mathfrak{S} = A + B\boldsymbol{\sigma} \cdot \hat{\boldsymbol{I}} + C\boldsymbol{\sigma} \cdot \hat{\boldsymbol{k}} + D\boldsymbol{\sigma} \cdot (\hat{\boldsymbol{I}} \times \hat{\boldsymbol{k}}), \tag{2.27}
$$

where,

$$
\begin{aligned}
A &= e^{i\alpha}\cos\beta, \quad B = ie^{i\alpha}\frac{\sin\beta}{\beta}\beta_B, \\
C &= ie^{i\alpha}\frac{\sin\beta}{\beta}\beta_C, \quad D = ie^{i\alpha}\frac{\sin\beta}{\beta}\beta_D, \\
\alpha &= Z\left(A' + P_1 H'\left(\hat{\boldsymbol{k}}_n\cdot\hat{\boldsymbol{I}}\right) + P_2 E'\left(\left(\hat{\boldsymbol{k}}_n\cdot\hat{\boldsymbol{I}}\right)^2 - \frac{1}{3}\right)\right), \\
\beta_B &= Z\left(P_1 B' + P_2 F'\left(\hat{\boldsymbol{k}}_n\cdot\hat{\boldsymbol{I}}\right) + \frac{1}{3}P_3 B_3'\left(\left(\hat{\boldsymbol{k}}_n\cdot\hat{\boldsymbol{I}}\right)^2 - 1\right)\right), \\
\beta_C &= Z\left(C' + P_1 K'\left(\hat{\boldsymbol{k}}_n\cdot\hat{\boldsymbol{I}}\right) - \frac{1}{3}P_2 F' + \frac{2}{3}P_3 B_3'\left(\hat{\boldsymbol{k}}_n\cdot\hat{\boldsymbol{I}}\right)\right), \\
\beta_D &= Z\left(P_1 D' + P_2 G'\left(\hat{\boldsymbol{k}}_n\cdot\hat{\boldsymbol{I}}\right)\right), \\
\beta &= \sqrt{\beta_B^2 + \beta_C^2 + \beta_D^2}, \\
Z &= \frac{2\pi\rho}{k}z.
\end{aligned}
\tag{6.21}
$$

In Eq.2.29, 2.30, and 2.31, the polarization direction of neutrons is only along the x-axis, however the following relation is obtained by polarization along the y- or z-axis.

$$
A_y = 4\left(\frac{\mathrm{Re}\,A^*B}{|A|^2} + \frac{\mathrm{Im}\,C^*D}{|A|^2}\right),\ A_z = 4\left(\frac{\mathrm{Re}\,A^*C}{|A|^2} + \frac{\mathrm{Im}\,D^*B}{|A|^2}\right), \tag{6.22}
$$

$$
P_y = 4\left(\frac{\mathrm{Re}\,A^*B}{|A|^2} - \frac{\mathrm{Im}\,C^*D}{|A|^2}\right),\ P_z = 4\left(\frac{\mathrm{Re}\,A^*C}{|A|^2} - \frac{\mathrm{Im}\,D^*B}{|A|^2}\right), \tag{6.23}
$$

$$
\begin{aligned}
K_{\pm y}^{\pm y} &= \frac{|A|^2 \pm 2\,\mathrm{Re}\,A^*B + |B|^2}{|A|^2},\quad K_{\mp y}^{\pm y} = \frac{|C|^2 \pm 2\,\mathrm{Re}\,C^*D + |D|^2}{|A|^2}, \\
K_{\pm z}^{\pm z} &= \frac{|A|^2 \pm 2\,\mathrm{Re}\,A^*C + |C|^2}{|A|^2},\quad K_{\mp z}^{\pm z} = \frac{|D|^2 \pm 2\,\mathrm{Re}\,D^*B + |B|^2}{|A|^2}.
\end{aligned}
\tag{6.24}
$$

The determination of the tensor polarization component is attempted by combining the above observable quantities. First, the determination of P_1 is carried out by measuring $K_{\mp z}^{\pm z}$ including B term. The B term contains β_B depending on P_1, P_2, and P_3, and β_B depends on B', F', and B_3', and their dependence on neutron energy is different (See Appendix C for details). The spin rotation due to the pseudomagnetic field (discussed in the next section) varies with the magnitude of the polarization. Thus, P_1 is determined, however the polarization components contained in $P_2\left(\hat{\boldsymbol{k}}_n\cdot\hat{\boldsymbol{I}}\right)$ and $P_3\left(\left(\hat{\boldsymbol{k}}_n\cdot\hat{\boldsymbol{I}}\right)^2 - 1\right)$ are indefinite. Then, it is considered to change

the $\hat{\boldsymbol{k}}_n \cdot \hat{\boldsymbol{I}}$ formed by the angle between neutron beam direction and the target polarization direction. One way to change the $\hat{\boldsymbol{k}}_n \cdot \hat{\boldsymbol{I}}$ using the divergence of the incident neutron beam by scanning the neutron upstream slit. Another way is to change it by tilting the direction of the polarization maintaining magnetic field applied to the target. Scanning $\hat{\boldsymbol{k}}_n \cdot \hat{\boldsymbol{I}}$ in the above method changes $P_2\big(\hat{\boldsymbol{k}}_n \cdot \hat{\boldsymbol{I}}\big) + P_3\big(\big(\hat{\boldsymbol{k}}_n \cdot \hat{\boldsymbol{I}}\big)^2 - 1\big)$, so that P_3 and $P_2\big(\hat{\boldsymbol{k}}_n \cdot \hat{\boldsymbol{I}}\big)$ are determined from the minimum values ($\hat{\boldsymbol{k}}_n \cdot \hat{\boldsymbol{I}} \sim 0$). Finally, to determine P_2, the $K^{\pm z}_{\pm z}$ are measured and its asymmetry is calculated as follows,

$$\frac{K^{+z}_{+z} - K^{-z}_{-z}}{K^{+z}_{+z} + K^{-z}_{-z}} = \frac{2\,\mathrm{Re}\,A^* C}{|A|^2}. \tag{6.25}$$

The C term depends on C', $P_1 K'$, $P_2 F'/3$, and $P_3 B_3' 2/3$. The asymmetry calculation cancels $\hat{\boldsymbol{k}}_n \cdot \hat{\boldsymbol{I}}$-dependent $P_1 K'$ and $P_3 B_3' 2/3$. Therefore, only C' and $P_2 F'/3$ can be extracted, and P_2 can be determined by fitting with P_2 as a free parameter. The higher order tensor polarization components are determined by the above process, and finally the D term is measured by A_x and P_x measurements.

6.2.4 Pseudo-magnetic rotation in target

When a polarized neutron propagates in a polarized nuclear target, neutron spin rotates around the nuclear spin vector due to the neutron–nucleus strong interaction [80]. This property produced by nuclear spin and polarized neutrons is called "Pseudo-magnetism", compared with the Larmor precession of neutron in magnetic field as shown in Fig.6.9. The B term in Eq.2.27 corresponds to the incoherent amplitude due to the pseudomagnetic field. The existence of this term causes a large spin rotation in the target and can generate false T-violation. Also, as shown in the Eq.6.21, $|\sin\beta/\beta|$ behaves as a suppression factor, and the experimental sensitivity for the D term can be reduced. Therefore, suppressing spin rotation by applying a compensation magnetic field corresponding to the pseudo-magnetic field has been discussed. The effective magnetic moment of neutrons in a matter with number density N has the following relation.

$$\mu_{\mathrm{eff}} = \frac{\mu_n m_n}{2\pi\hbar^2 N}, \tag{6.26}$$

where μ_n is the neutron magnetic moment. For β_B in Eq.6.21, the term due to the external compensation magnetic field is added as follows,

$$\beta_B = Z\left(P_1 B' - \mu_{\mathrm{eff}} B_0 + P_2 F'\left(\hat{k}_n \cdot \hat{I}\right) + \frac{1}{3} P_3 B_3'\left(\left(\hat{k}_n \cdot \hat{I}\right)^2 - 1\right)\right), \tag{6.27}$$

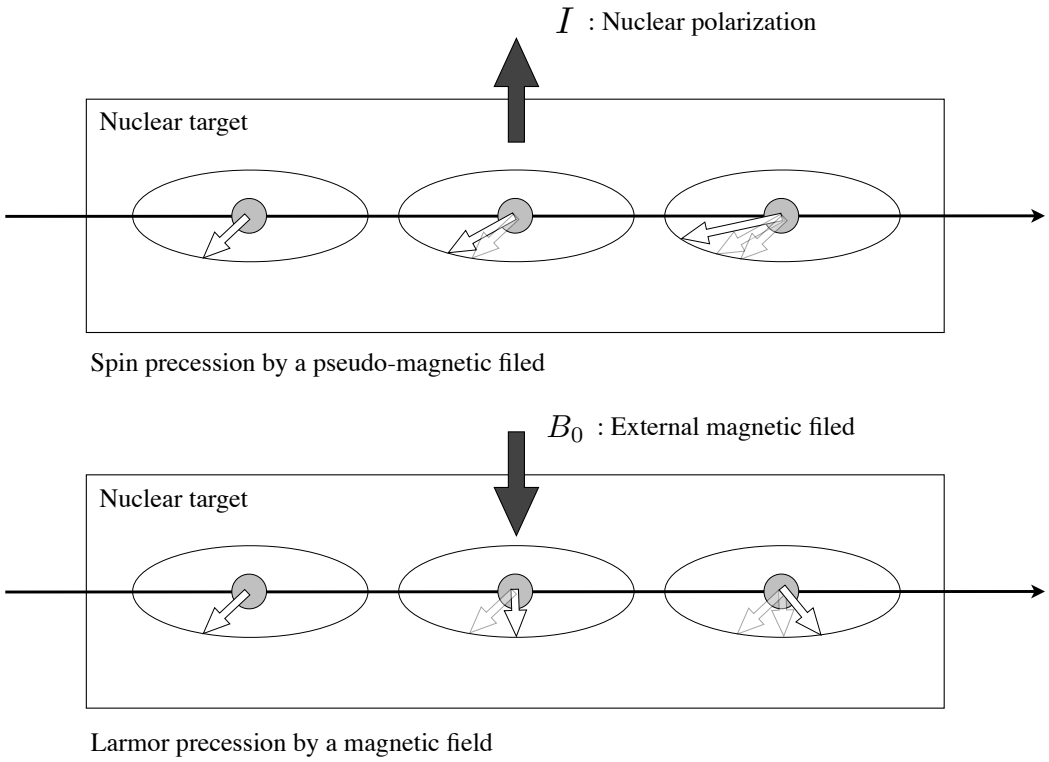

Figure 6.9: Illustration of the spin precession by a pseudo-magnetic field and a magnetic field. The upper figure shows spin rotation due to a pseudo magnetic field, and the lower figure shows spin rotation due to a magnetic field.

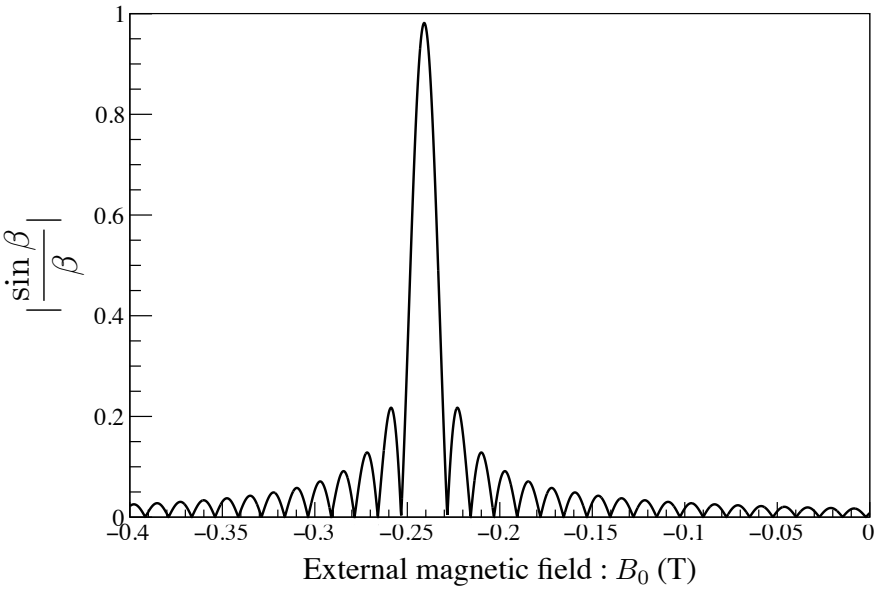

Figure 6.10: Magnetic field dependence of the suppression factor vicinity of the p-wave resonance in a 3.2-cm-thick $LaAlO_3$ crystal. It is not suppressed when the magnetic field which can cancel the pseudo-magnetic field is applied, and the damped oscillation can be observed when it is removed.

where B_0 is the magnetic field applied in the direction parallel to the nuclear spin. When an external magnetic field is applied to a nuclear spin polarized $LaAlO_3$ target, the suppression factor exhibits damped oscillation as shown in Fig.6.10. Since the B term, which is primarily responsible for producing the pseudo-magnetic field, depends on the nuclear polarization, the applied magnetic field must be adjusted according to the nuclear polarization of the target. When a $LaAlO_3$ crystal with a thickness of 3.2 cm is 100% polarized, it is necessary to apply an external magnetic field of approximately 0.24 T to cancel the pseudo magnetic field. As shown in Fig.6.11, the amount of spin rotation of neutrons changes according to the amplitude of the pseudo-magnetic field. This dependence can therefore be used to determine the polarization of the target nucleus discussed in the previous section.

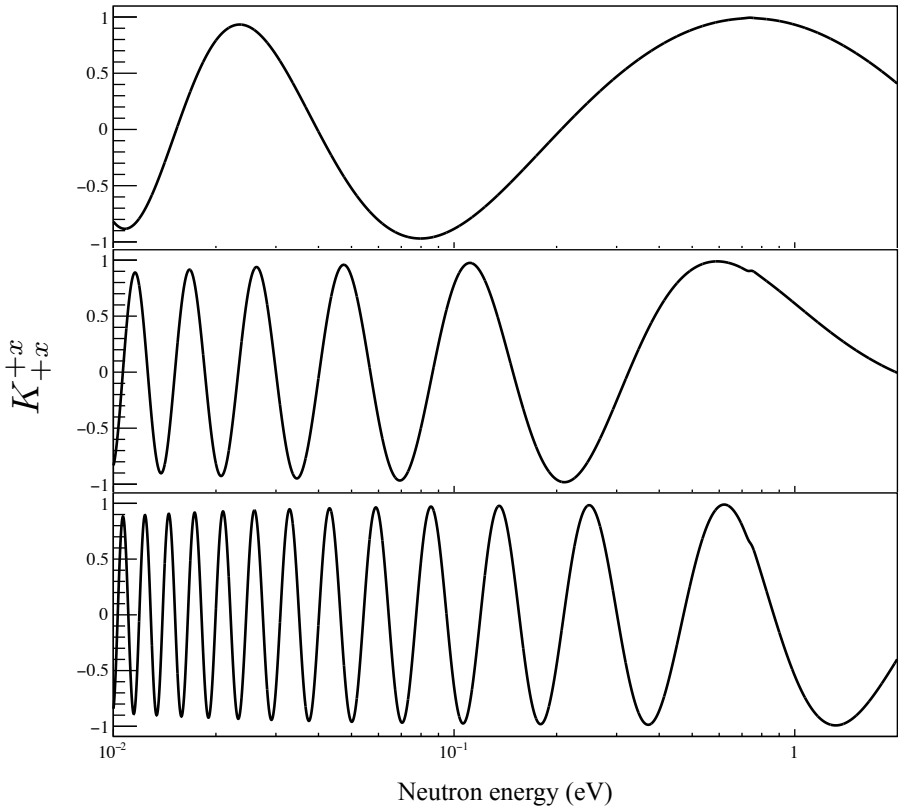

Figure 6.11: Energy dependence of neutron spin rotation due to the pseudo-magnetic field. The above figure shows the energy dependence of the neutron spin rotation when the B' term is completely suppressed by an external magnetic field. The middle and lower figures show the external magnetic field increased by 0.01 T from the fully suppressed condition.

Chapter 7

Conclusion

In order to access BSM physics, a new type of T-violation search using the symmetry violation enhancement mechanism in compound nuclear reactions has been discussed. The enhancement parameter $\kappa(J)$ should be determined experimentally. Angular correlation measurements in the $^{139}\mathrm{La}(n,\gamma)$ reaction with unpolarized neutrons in previous studies have constrained the value of the parameter, however the precise range remains uncertain. In this study, the angular correlation measurement was improved by polarizing the incident neutrons. A large $^{3}\mathrm{He}$ spin filter was installed onto J-PARC MLF BL04 to produce polarized neutrons. In order to minimize the depolarization of $^{3}\mathrm{He}$, a large solenoid coil and a guide magnet for neutron polarized transport were developed using FEM analysis. As a result, a sufficiently long relaxation time ($\tau_{\mathrm{decay}} \sim 100$ hour) was achieved. A left-right asymmetry for single γ-ray transitions was found in $^{139}\mathrm{La}(\vec{n},\gamma)$ using polarized neutrons $A_{\mathrm{LR}}^{\mathrm{gnd}} = 0.73 \pm 0.14$. The ϕ_p and $\kappa(J)$ were restricted by the analysis using the *sp*-mixing model. Restricted regions are uniquely determined by an integrated analysis using limitations from previous studies. Results are obtained to be $\phi_p = \left(105.4^{+9.1}_{-7.9}\right)^{\circ}$ and $\kappa(J) = 1.62^{+2.60}_{-0.95}$. Using these results, the author estimated the experimental sensitivity of the T-violation search. As the result, it was clarified that this method can be a powerful probe for the T-violation search. In addition, the condition required for the T-violation search was quantitatively clarified.

It is also desirable to verify the robustness of the *sp*-mixing model by measuring the correlation term in further (n,γ) reactions. Concretely, it seems to be an effective method of measuring correlation terms such as a_6 or a_{13} through the measurement of circularly polarization of γ rays in the $(n,\vec{\gamma})$ reaction.

Appendices

Appendix A

The angular distribution in (n, γ) reaction

On the basis of the *sp*-mixing model, we consider the amplitude of the (n, γ) reaction caused by the *s*- and *p*-wave neutrons, as shown in Fig.A.1. There are amplitudes where the entrance and exit channels are unchanged and amplitudes where the entrance and exit channels are different through the weak interaction.

$$
\begin{aligned}
V_1 &= -\sum_{r_s} \frac{1}{2k} \frac{\sqrt{g_{r_s} \Gamma^n_{r_s} \Gamma^\gamma_{r_s f}}}{E_n - E_{r_s} + i\Gamma_{r_s}/2}, \\
V_2 &= -\sum_{r_p} \frac{1}{2k} \frac{\sqrt{g_{r_p} \Gamma^n_{r_p} \Gamma^{\gamma f}_{r_p}}}{E_n - E_{r_p} + i\Gamma_{r_p}/2}, \\
V_3 &= -\sum_{r_s, r_p} \frac{1}{2k} \frac{\sqrt{g_{r_s} \Gamma^n_{r_s}} W \sqrt{\Gamma^\gamma_{r_p f}}}{\left(E_n - E_{r_p} + i\Gamma_{r_p}/2\right)\left(E_n - E_{r_s} + i\Gamma_{r_s}/2\right)}, \\
V_4 &= -\sum_{r_s, r_p} \frac{1}{2k} \frac{\sqrt{g_{r_p} \Gamma^n_{r_p}} W \sqrt{\Gamma^\gamma_{r_s f}}}{\left(E_n - E_{r_s} + i\Gamma_{r_s}/2\right)\left(E_n - E_{r_p} + i\Gamma_{r_p}/2\right)},
\end{aligned}
\tag{A.1}
$$

where k is the neutron momentum, E_n is the kinetic energy of the neutron, Γ^n_r is the neutron width, Γ^γ_{rf} is the partial γ width to f-th final state, E_r is the resonance energy of the neutron resonance and W is the weak matrix element. where g_r is statistical weight factor and defined as

$$
g_r = \frac{2J_r + 1}{2(2I + 1)}, \tag{A.2}
$$

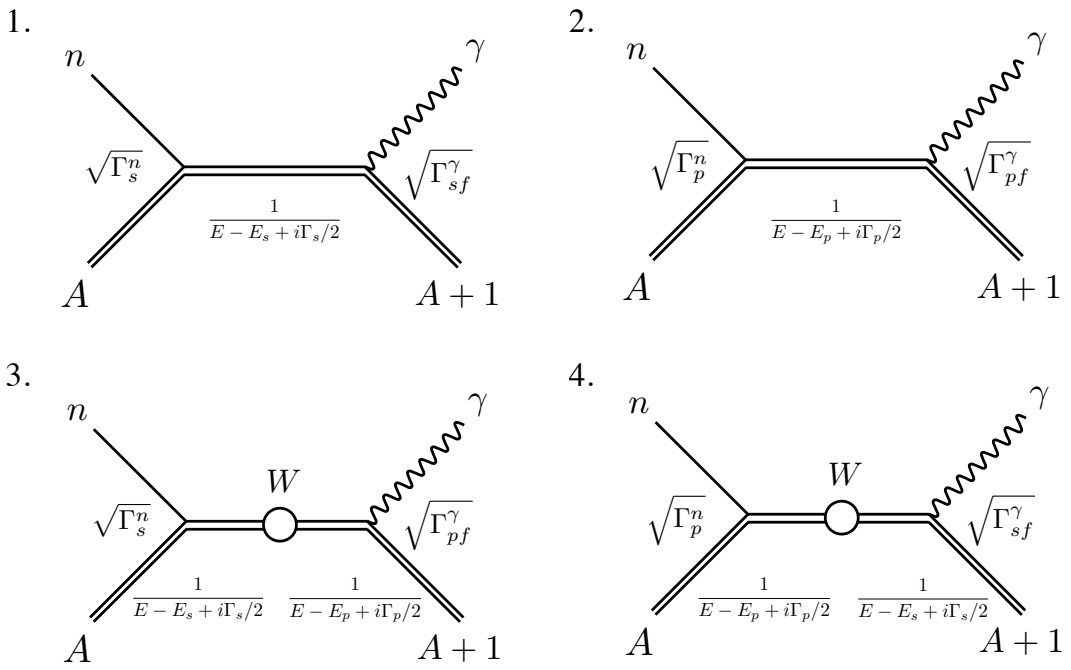

Figure A.1: Diagrams of amplitude of (n,γ) reactions through s- and p-wave state. The circle denotes the weak interaction.

where J_r and I is the spin of the compound status and the target nucleus, respectively. Each correlation term for the (n,γ) reaction can be described as a_1–a_{17} using V_1–V_4:

$$
\begin{aligned}
a_0 &= \sum_{r_s} |V_{1r_s}|^2 + \sum_{r_p} \left|V_{2r_p}\right|^2, \\
a_1 &= 2\,\mathrm{Re} \sum_{r_s r_p j} V_{1r_s} V_{2r_p}^* P \left(J_{r_s} J_{r_p} \frac{1}{2} j 1 I F \right) z_{r_p j}, \\
a_2 &= -2\,\mathrm{Im} \sum_{r_s r_p j} V_{1r_s} V_{2r_p}^* \beta_j P \left(J_{r_s} J_{r_p} \frac{1}{2} j 1 I F \right) z_{r_p j}, \\
a_3 &= 3\sqrt{10}\,\mathrm{Re} \sum_{r_p j r'_p j'} V_{2r_p} V_{2r'_p}^* P \left(J_{r_p} J_{r'_p} j j' 2 I F \right) \left\{ \begin{array}{ccc} 2 & 1 & 1 \\ 0 & \frac{1}{2} & \frac{1}{2} \\ 2 & j & j' \end{array} \right\} z_{r_p j} z_{r_p j'}, \\
a_4 &= -6\sqrt{5}\,\mathrm{Im} \sum_{r_p j r'_p j'} V_{2r_p} V_{2r'_p}^* P \left(J_{r_p} J_{r'_p} j j' 2 I F \right) \left\{ \begin{array}{ccc} 2 & 1 & 1 \\ 1 & \frac{1}{2} & \frac{1}{2} \\ 2 & j & j' \end{array} \right\} z_{r_p j} z_{r_p j'}, \\
a_5 &= -\,\mathrm{Re} \sum_{r_s r'_s} V_{1r_s} V_{1r'_s}^* P \left(J_{r_s} J_{r_s} \frac{1}{2} \frac{1}{2} 1 I F \right)
\end{aligned}
$$

$$
\begin{aligned}
& -6\mathrm{Re}\sum_{r_p j r'_p j'} V_{2r_p} V^*_{2r'_p} P\left(J_{r_p} J_{r'_p} jj'1IF\right) \left\{ \begin{array}{ccc} 0 & 1 & 1 \\ 1 & \frac{1}{2} & \frac{1}{2} \\ 1 & j & j' \end{array} \right\} z_{r_p j} z_{r_p j'}, \\
a_6 &= -2\,\mathrm{Re}\sum_{r_s} V_{1r_s} V^*_{2r_p} \delta_{J_{r_s} J_{r_p}} z_{r_p \frac{1}{2}}, \\
a_7 &= \sqrt{3}\,\mathrm{Re}\sum_{r_s i_p j} V_{1r_s} V^*_{2r_p} P\left(J_{r_s} J_{r_p} \frac{1}{2}\frac{3}{2} 2IF\right) z_{r_p \frac{3}{2}}, \\
a_8 &= -18\,\mathrm{Re}\sum_{r_p j r'_p j'} V_{2r_p} V^*_{2r'_p} P\left(J_{r_p} J_{r'_p} jj'1IF\right) \left\{ \begin{array}{ccc} 2 & 1 & 1 \\ 1 & \frac{1}{2} & \frac{1}{2} \\ 2 & j & j' \end{array} \right\} z_{r_p j} z_{r_p j'} \\
a_9 &= -2\,\mathrm{Re}\sum_{r_s r'_s j} V_{1r_s} V^*_{3r'_s} P\left(J_{r_s} J_{r_s} \frac{1}{2}\frac{1}{2} 1IF\right) \\
& \quad -12\,\mathrm{Re}\sum_{r_p j r'_p j'} V_{2r_p} V^*_{4r'_p} P\left(J_{r_p} J_{r'_p} jj'1IF\right) \left\{ \begin{array}{ccc} 0 & 1 & 1 \\ 1 & \frac{1}{2} & \frac{1}{2} \\ 1 & j & j' \end{array} \right\} z_{r_p j} z_{r_p j'}, \\
a_{10} &= -2\,\mathrm{Re}\sum_{r_s} \left[V_{2r_p} V^*_{3r_s} + V_{1r_s} V^*_{4r_p}\right] \delta_{J_{r_s} J_{r_p}} z_{r_p \frac{1}{2}}, \\
a_{11} &= \sqrt{3}\,\mathrm{Re}\sum_{r_s r_p} \left[V_{2r_p} V^*_{3r_s} + V_{1r_s} V^*_{4r_p}\right] P\left(J_{r_s} J_{r'_p} \frac{1}{2}\frac{3}{2} 2IF\right) z_{r_p \frac{1}{2}}, \\
a_{12} &= -36\,\mathrm{Im}\sum_{r_s i_p j} V_{2r_p} V^*_{4r_p} P\left(J_{r_p} J'_{r_p} jj1IF\right) \left\{ \begin{array}{ccc} 2 & 1 & 1 \\ 1 & \frac{1}{2} & \frac{1}{2} \\ 1 & j & j' \end{array} \right\} z_{r_p j} z_{r_p j'}, \\
a_{13} &= 2\,\mathrm{Re}\sum_{r_s} V_{1r_s} V^*_{3r_s} + 2\,\mathrm{Re}\sum_{r_p} V_{2r_p} V^*_{4r_p}, \\
a_{14} &= 2\,\mathrm{Re}\sum_{r_s r_p j} \left[V_{2r_p} V^*_{3r_s} + V_{1r_s} V^*_{4r_p}\right] P\left(J_{r_s} J_{r'_p} \frac{1}{2} j1IF\right) z_{r_p j}, \\
a_{15} &= 2\,\mathrm{Im}\sum_{r_s r_p j} \left[V_{2r_p} V^*_{3r_s} - V_{1r_s} V^*_{4r_p}\right] P\left(J_{r_s} J_{r'_p} \frac{1}{2} j1IF\right) z_{r_p j}, \\
a_{16} &= 6\sqrt{10}\,\mathrm{Re}\sum_{r_p j r'_p j'} V_{2r_p} V^*_{4r'_p} P\left(J_{r_p} J_{r'_p} jj'2IF\right) \left\{ \begin{array}{ccc} 2 & 1 & 1 \\ 0 & \frac{1}{2} & \frac{1}{2} \\ 2 & j & j' \end{array} \right\} z_{r_p j} z_{r_p j'}, \\
a_{17} &= -12\sqrt{5}\,\mathrm{Im}\sum_{r_p j r'_p j'} V_{2r_p} V^*_{4r'_p} P\left(J_{r_p} J_{r'_p} jj'2IF\right) \left\{ \begin{array}{ccc} 2 & 1 & 1 \\ 1 & \frac{1}{2} & \frac{1}{2} \\ 2 & j & j' \end{array} \right\} z_{r_p j} z_{r_p j'}, \qquad \text{(A.3)}
\end{aligned}
$$

where

$$P\left(JJ'jj'kIF\right) = \quad (-1)^{J+J'+j'+I+F}\frac{3}{2}\sqrt{\left(2J+1\right)\left(2J'+1\right)\left(2j+1\right)\left(2J'+1\right)} \times \left\{ \begin{array}{ccc} k & j & j' \\ I & J' & J \end{array} \right\} \left\{ \begin{array}{ccc} k & 1 & 1 \\ F & J & J' \end{array} \right\}, \tag{A.4}$$

$$\beta_j = \left\{ \begin{array}{ll} 1 & \left(j=\frac{1}{2}\right) \\ -\frac{1}{2} & \left(j=\frac{3}{2}\right) \end{array} \right. , \tag{A.5}$$

where J, j, I, and F are the spin of the compound state, total angular momentum of the neutron, spin of the target nucleus and spin of the final state, respectively. The ratios of partial neutron widths to neutron widths of p-wave resonances are given as

$$z_{r_p j} = \left\{ \begin{array}{ll} x_{r_p} = \sqrt{\frac{\Gamma^n_{p,j=\frac{1}{2}}}{\Gamma_p}} & \left(j=\frac{1}{2}\right) \\ y_{r_p} = \sqrt{\frac{\Gamma_{p,j=\frac{3}{2}}}{\Gamma_p}} & \left(j=\frac{3}{2}\right) \end{array} \right. . \tag{A.6}$$

Appendix B

^{3}He polarization relaxation

The polarization of ^{3}He is relaxed by various factors. These main factors are the relaxation by the magnetic dipole interaction between ^{3}He, by the collision to the glass cell wall, by the magnetic impurities in the cell, and by the spatial inhomogeneity of the magnetic field. When the polarization relaxation rates for each relaxation process are Γ_{dipol}, Γ_{wall}, Γ_{imp}, and Γ_{field}, the ^{3}He polarization relaxation rate Γ_{He} and the polarization relaxation time constant T_1 of a certain ^{3}He spin filter have the following relation,

$$\frac{1}{T_1} = \Gamma_{\mathrm{He}} = \Gamma_{\mathrm{dipol}} + \Gamma_{\mathrm{wall}} + \Gamma_{\mathrm{imp}} + \Gamma_{\mathrm{field}} + \cdots . \tag{B.1}$$

While Γ_{dipol}, Γ_{wall}, and Γ_{imp} are intrinsic values of the spin filter, Γ_{field} depends on the external magnetic field. Therefore it is important to design the magnetic field according to the measurement environment. Since ^{3}He atoms thermally motion in the glass cell, the neutron polarization is relaxed by a spatial inhomogeneity of the magnetic field, and the polarization relaxation rate Γ_{field} due to the spatial inhomogeneity of the magnetic field is given as follows:

$$\Gamma_{\mathrm{field}} = D\frac{\left|\vec{\nabla}B_x\right|^2 + \left|\vec{\nabla}B_y\right|^2}{B_0^2}, \tag{B.2}$$

where D is the diffusion coefficient of ^{3}He, and Fig.B.1 shows the relationship between spatial inhomogeneity and relaxation time. It is shown that the mean free path of ^{3}He collisions in the glass cell becomes shorter as the pressure increases, and the relaxation time becomes longer and less affected by the spatial inhomogeneity of the magnetic field. The gas pressure of ^{3}He in the spin filter used in this experiment is 3 atm. To achieve a relaxation time of about 100 hours, the spatial inhomogeneity of the magnetic field less than approximately 2×10^{-3} cm^{-1} is required. In general, the spatial uniformity of the magnetic field is improved by increasing the diameter

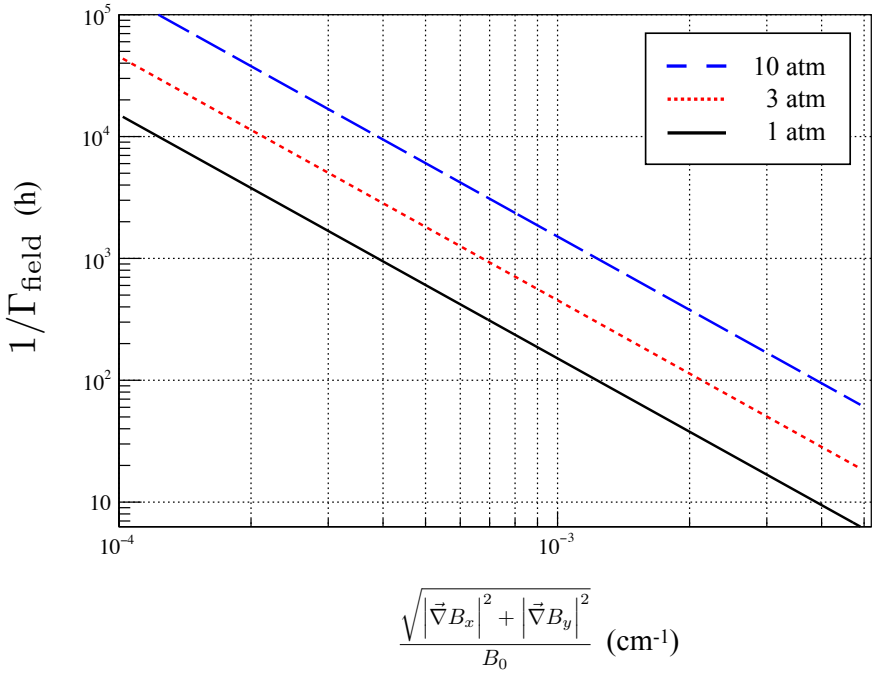

Figure B.1: Relation between spatial homogeneity of magnetic field and relaxation time. The solid, dotted and dashed lines show when the gas pressure is 1, 3, and 10 atm, respectively. As the gas pressure in the cell becomes higher, the mean free path of ^{3}He becomes shorter and the influence of the spatial inhomogeneity of the magnetic field decreases.

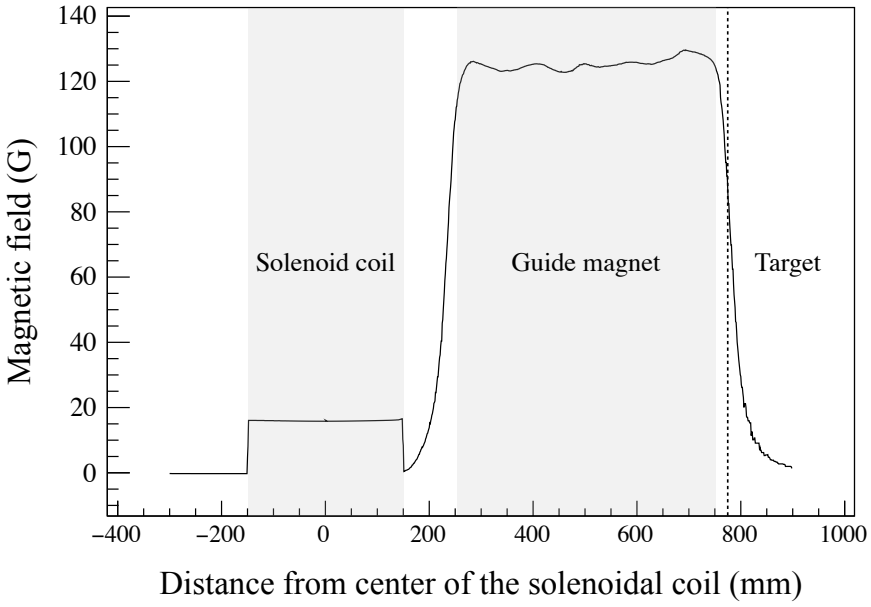

Figure B.2: Magnetic field in the x-axis direction from the solenoid coil to the target position estimated by FEM analysis. A magnetic field of 15 G is applied to the ^{3}He cell section, 80 G was applied to the target installation position, and a nonzero magnetic field was applied to the surface of the solenoid coil.

and the length of the solenoid coil. However, due to the spatial restriction of the installation position in the beamline, there is a restriction especially on the diameter. In addition, it is necessary to connect the solenoid magnetic field and the magnetic field for neutron polarized transport without making zero magnetic field. For this purpose, as shown in Fig.3.17, it is necessary to install a guide magnet near the solenoid to cancel the magnetic field generated by the solenoid. Furthermore, as shown in Fig.3.16, since neutrons pass through the side of the solenoid, we do not want to place as much material as possible in the neutron transmission region from the viewpoint of radio activation. There are three constraints: (1) Constraints on the radial direction of the solenoid coil, (2) Constraints on the arrangement of the guide magnet, and (3) Constraints on the material of the solenoid coil. Under these constraints, the parameters of the polarizers were determined by FEM analysis. As a result, as shown in Fig.B.2, the system which can transport the neutron polarization while keeping the quantization axis without making zero magnetic field region from the ^{3}He cell to the target was realized. In addition, by adjusting the position of the guide magnet and the size of the hole made in the permalloy film wound on the solenoid surface, we found a parameter that minimizes the effect of the guide magnetic field on the spatial homogeneity of the magnetic field inside the solenoid. As shown in Fig.B.3, a solenoid coil has been developed that satisfies the spatial homogeneity 2×10^{-3} cm^{-1} of the magnetic field at the cell installation position.

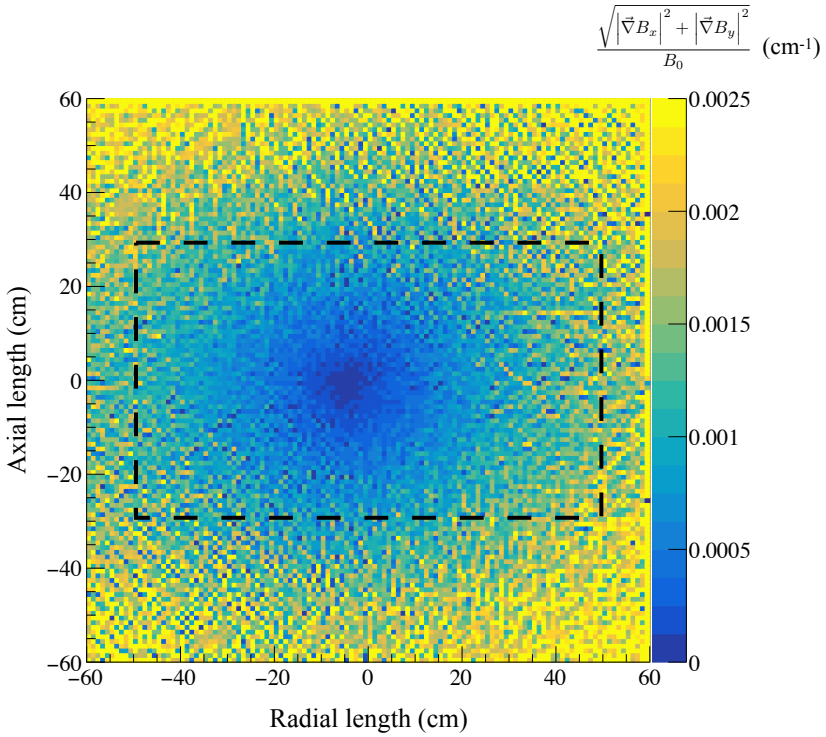

Figure B.3: Homogeneity of the magnetic field around the ^{3}He spin filter installation position in the solenoid coil estimated by the FEM analysis.

Appendix C

Forward scattering amplitude for ^{139}La

Coefficient of the forward scattering amplitude for ^{139}La with $I = 7/2$ in Eq.6.20 is described as [79]

$$
\begin{aligned}
A' &= \frac{-1}{32k}\left(7\frac{\Gamma^n_{s1}}{E-E_{s1}+i\Gamma_{s1}/2}+9\frac{\Gamma^n_{s0}}{E-E_{s0}+i\Gamma_{s0}/2}+9\frac{\Gamma^n_{p}}{E-E_{p}+i\Gamma_{p}/2}\right)+\frac{1}{16}\left(9a_{s0}+7a_{s1}\right),\\
B' &= \frac{-1}{32k}\left[7\frac{\Gamma^n_{s0}}{E-E_{s0}+i\Gamma_{s0}/2}-7\frac{\Gamma^n_{s1}}{E-E_{s1}+i\Gamma_{s1}/2}\right.,\\
&\quad \left.+\frac{\Gamma^n_{p}}{E-E_{p}+i\Gamma_{p}/2}\left(-\frac{39}{4}x_S^2+\frac{9}{2}\sqrt{\frac{7}{5}}x_Sy_S+\frac{63}{20}y_S^2\right)\right]+\frac{7}{16}\left(a_{s0}-a_{s1}\right),\\
C' &= \frac{3\sqrt{3}}{32k}\frac{\sqrt{\Gamma^n_{s0}}W\sqrt{\Gamma^n_{p}}}{\left(E-E_{p}+i\Gamma_{p}/2\right)\left(E-E_{s0}+i\Gamma_{s0}/2\right)}\times\left(\sqrt{7}x_S-\sqrt{5}y_S\right),\\
D' &= \frac{\sqrt{21}}{8k}\frac{x_s\sqrt{\Gamma^n_{s0}}W_{\mathrm{T}}\sqrt{\Gamma^n_{p}}}{\left(E-E_{p}+i\Gamma_{p}/2\right)\left(E-E_{s0}+i\Gamma_{s0}/2\right)},\\
H' &= -\frac{3\sqrt{7}}{32k}\frac{\sqrt{\Gamma^n_{s0}}W\sqrt{\Gamma^n_{p}}}{\left(E-E_{p}+i\Gamma_{p}/2\right)\left(E-E_{s0}+i\Gamma_{s0}/2\right)}\times\left(x_S+\sqrt{35}y_S\right),\\
K' &= -\frac{\sqrt{21}}{128k}\frac{\Gamma^n_{p}}{E-E_{p}+i\Gamma_{p}/2}\times\left(3\sqrt{\frac{3}{7}}x_S^2-18\sqrt{\frac{3}{5}}x_Sy_S+\frac{11}{5}\sqrt{21}y_S^2\right),\\
E' &= \frac{3\sqrt{21}}{256k}\frac{\Gamma^n_{p}}{E-E_{p}+i\Gamma_{p}/2}\times\left(5\sqrt{\frac{3}{7}}x_S^2-6\sqrt{\frac{3}{5}}x_Sy_S-\frac{11}{5}\sqrt{21}y_S^2\right),
\end{aligned}
$$

$$
\begin{aligned}
F' &= -\frac{3\sqrt{21}}{32k}\frac{\sqrt{\Gamma^n_{s0}}W\sqrt{\Gamma^n_p}}{(E-E_p+i\Gamma_p/2)\,(E-E_{s0}+i\Gamma_{s0}/2)}\times\left(x_S+\sqrt{\frac{7}{5}}y_S\right),\\
G' &= \frac{9\sqrt{7}i}{32\sqrt{5}k}\frac{\sqrt{\Gamma^n_{p1}}W^{pp}_T\sqrt{\Gamma^n_p}}{(E-E_p+i\Gamma_p/2)\,(E-E_{p1}+i\Gamma_{p1}/2)}\times(x_Sy_{S1}-x_{S1}y_S),\\
(B'_3) &= \frac{189}{256k}\frac{\Gamma^n_p}{E-E_p+i\Gamma_p/2}\left(\frac{1}{7}x_S^2+\frac{2}{\sqrt{35}}x_Sy_S+\frac{1}{5}y_S^2\right),
\end{aligned}
\tag{C.1}
$$

where a_{s0} and a_{s1} are neutron scattering lengths with the total spins $J=4$ and $J=3$, correspondingly, W_T^{pp} is a T-violating matrix element due to interference between p-wave resonances and is considered to be negligibly smaller than $W_{\rm T}$. The x_S and y_S satisfy the following relationship from Eq.2.19.

$$
\begin{aligned}
\begin{bmatrix} x_S \\ y_S \end{bmatrix} &= \frac{1}{\sqrt{3(2I+1)}}\begin{bmatrix} -\sqrt{2I-1} & 2\sqrt{I+1} \\ 2\sqrt{I+1} & \sqrt{2I-1} \end{bmatrix}\begin{bmatrix} x \\ y \end{bmatrix} \quad \left(J=I-\frac{1}{2}\right),\\
\begin{bmatrix} x_S \\ y_S \end{bmatrix} &= \frac{1}{\sqrt{3(2I+1)}}\begin{bmatrix} -2\sqrt{I} & \sqrt{2I+3} \\ \sqrt{2I+3} & 2\sqrt{I} \end{bmatrix}\begin{bmatrix} x \\ y \end{bmatrix} \quad \left(J=I+\frac{1}{2}\right).
\end{aligned}
\tag{C.2}
$$

Figures C.1 and C.2 show the energy dependence of the real and imaginary parts of correlation terms. The forward scattering amplitudes of nuclear spins larger than 1/2 have correlation terms due to higher order tensor polarization. Since their presence can cause false T-violation, it is important to establish a evaluation method and separation method of the tensor polarization component. Here, we focus on the different energy dependence of each correlation term, and discuss the separation method of each correlation term and higher tensor polarization. Equation 6.19 is rewritten as follows when it is separated by the energy dependent and independent matrix terms.

$$
f = R\alpha^\mu\mathcal{L}_{\mu\nu}\mathcal{W}^\nu, \tag{C.3}
$$

where R is the nuclear radius and each matrix can be expressed as,

$$
\alpha^\mu = \begin{bmatrix} \alpha \\ \beta_{\hat{I}} \\ \beta_{\hat{\boldsymbol{k}}_n} \\ \beta_{\hat{\boldsymbol{k}}_n\times\hat{I}} \end{bmatrix}, \qquad \mathcal{W}^\nu = \begin{bmatrix} \frac{a}{R} \\ \frac{i}{kR}\frac{\Gamma^n_s}{\Gamma_s}R_s \\ \frac{i}{kR}\frac{\Gamma^n_p}{\Gamma_p}R_p \\ \frac{1}{kR}\frac{\sqrt{\Gamma^n_s}v\sqrt{\Gamma^n_p}}{\Gamma_s\Gamma_p}R_sR_p \\ \frac{i}{kR}\frac{\sqrt{\Gamma^n_p}v^{pp'}_T\sqrt{\Gamma^n_{p'}}}{\Gamma_p\Gamma_{p'}}R_pR_{p'} \end{bmatrix}, \tag{C.4}
$$

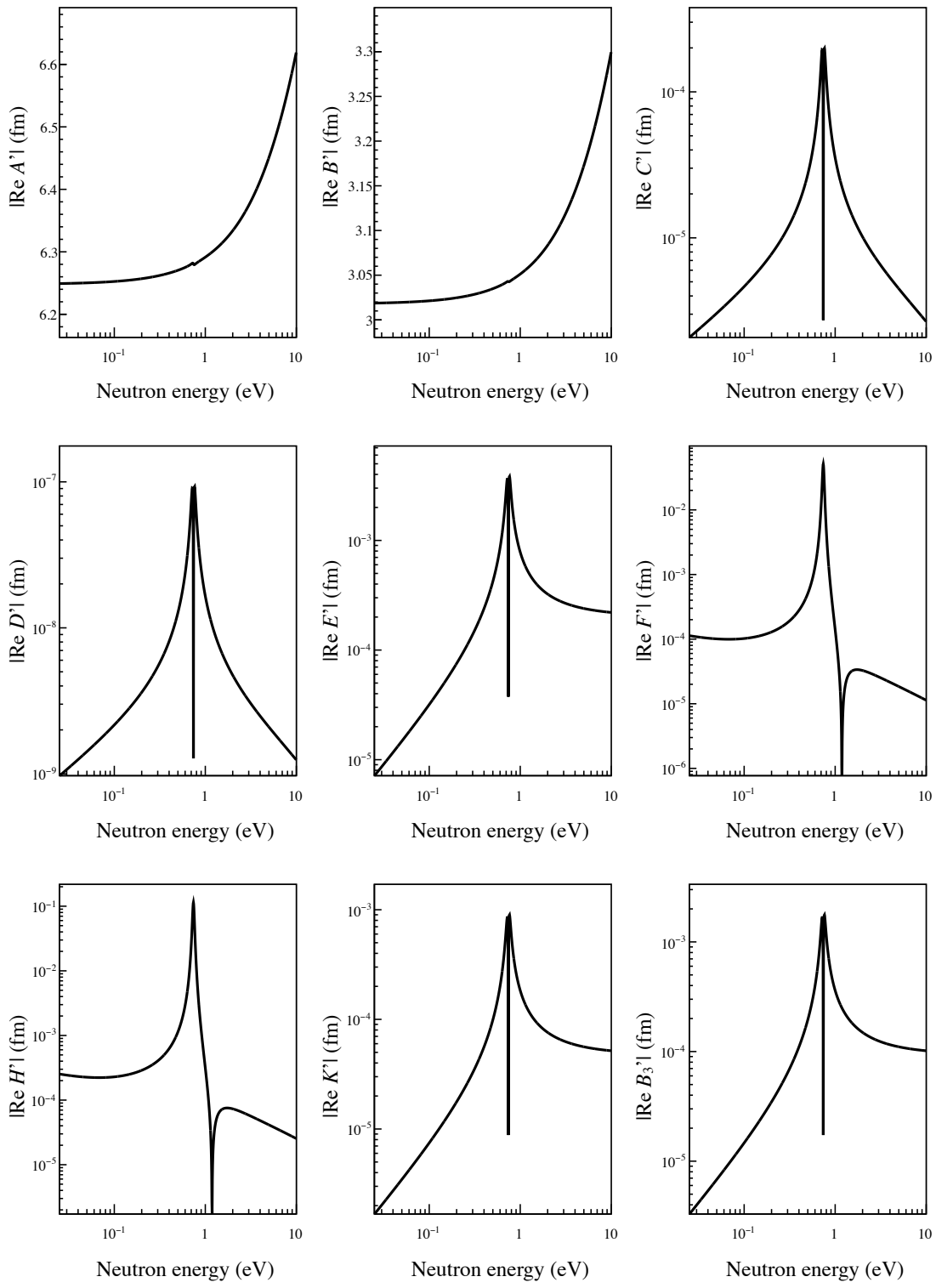

Figure C.1: Energy dependence of the real part of forward scattering amplitude for ^{139}La with $I = 7/2$.

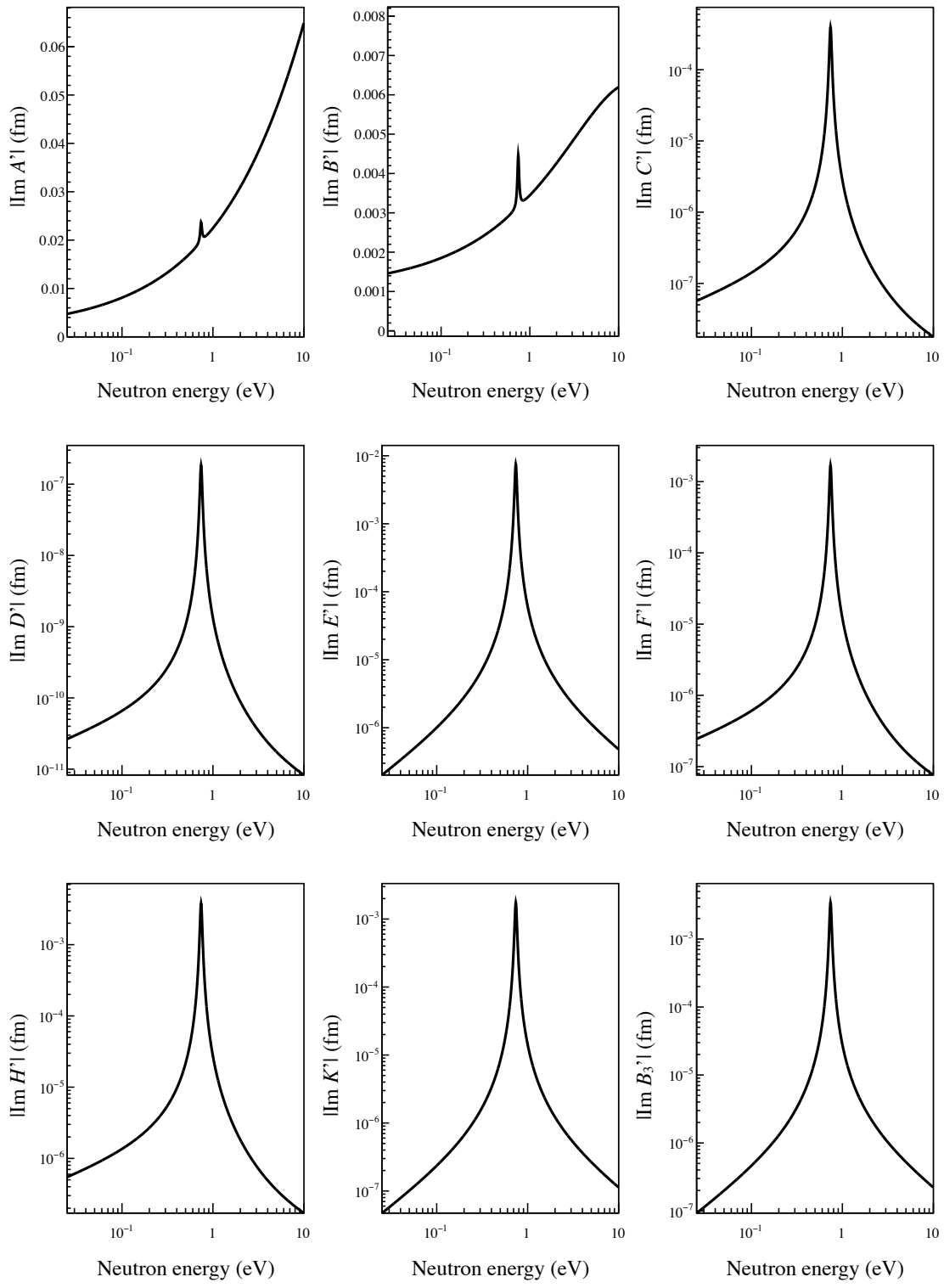

Figure C.2: Energy dependence of the imaginary part of forward scattering amplitude for ^{139}La with $I = 7/2$.

$$\mathcal{L}_{\mu\nu} = \begin{bmatrix} 1 & X_A & X_A + P_2 X_E \left(\left(\hat{\boldsymbol{k}}_n \cdot \hat{\boldsymbol{I}} \right)^2 - \frac{1}{3} \right) & P_1 X_H^{\mathrm{P}} \left(\hat{\boldsymbol{k}}_n \cdot \hat{\boldsymbol{I}} \right) & 0 \\ P_1 \frac{\Delta a}{a} & P_1 X_B & P_1 X_B \epsilon_B - \frac{1}{3} P_3 X_{B_3} \left(1 - \left(\hat{\boldsymbol{k}}_n \cdot \hat{\boldsymbol{I}} \right)^2 \right) & P_2 X_F^{\mathrm{P}} \left(\hat{\boldsymbol{k}}_n \cdot \hat{\boldsymbol{I}} \right) & 0 \\ 0 & 0 & \left(P_1 X_K + \frac{2}{3} P_3 X_{B_3} \right) \left(\hat{\boldsymbol{k}}_n \cdot \hat{\boldsymbol{I}} \right) & X_C^{\mathrm{P}} - \frac{1}{3} P_2 X_F^{\mathrm{P}} & 0 \\ 0 & 0 & 0 & P_1 X_D^{\mathrm{PT}} \frac{w}{v} & P_2 X_G^{\mathrm{T}} \end{bmatrix}, \tag{C.5}$$

where R_r gives the Bright-Wigner amplitude formula for the rth resonance as follows,

$$R_r = \frac{i\Gamma_r/2}{E - E_r + i\Gamma_r/2}. \tag{C.6}$$

Each constant contained in the energy independent matrix $\mathcal{L}_{\mu\nu}$ can be described as follows,

$$\begin{aligned} &a = \tfrac{1}{16}\left(9a_{s0} + 7a_{s1}\right), && \Delta a = \tfrac{7}{16}\left(a_{s0} - a_{s1}\right), && \epsilon_B = -x^2 + 2\sqrt{\tfrac{5}{7}}xy + \tfrac{2}{35}y^2, \\ &X_A = \tfrac{9}{32}, && X_B = \tfrac{7}{32}, && X_C^{\mathrm{P}} = -\tfrac{9}{16}x, \\ &X_D^{\mathrm{PT}} = -\tfrac{7}{16}\left(-x + \sqrt{\tfrac{5}{7}}y\right), && X_H^{\mathrm{P}} = \tfrac{7\sqrt{3}}{16}\left(x + 2\sqrt{\tfrac{5}{7}}y\right), && X_K = \tfrac{7}{16}\left(x^2 + \sqrt{\tfrac{5}{7}}xy - \tfrac{1}{70}y^2\right), \\ &X_E = \tfrac{9}{16}\left(\sqrt{\tfrac{7}{5}}xy + \tfrac{13}{20}y^2\right), && X_F^{\mathrm{P}} = \tfrac{9}{16}\sqrt{\tfrac{7}{5}}y, && X_G^{\mathrm{T}} = -\tfrac{9\sqrt{7}}{256\sqrt{5}}\left(x_S y'_S - x'_S y_S\right), \\ &X_{B_3} = -\tfrac{81}{320}y^2. \end{aligned} \tag{C.7}$$

The energy dependence matrix $\mathcal{W}^\nu$ obtained via the matrix expansion shows clearly that each correlation term has a different energy dependence, and Fig.C.3 shows the polar coordinate representation of each component of the $\mathcal{W}^\nu$. Since the D term has the energy dependence of the third component of the $\mathcal{W}^\nu$, the energy dependence is different in the whole region from the zeroth component, in the p-wave resonance part from the first component, and in the s-wave resonance part from the second component. In addition, it is estimated that these contributions can be easily discriminated, since the amplitude also differs at least 10^2 times or more.

Next, a method of discriminating other correlation terms with the same energy dependence as the D term is discussed. All the components in the fourth column of the $\mathcal{L}_{\mu\nu}$ have the same energy dependence as the D term. The angle between the nuclear target and the neutron beam in Eq.C.5 is defined as χ, and it can be expressed as follows by matrix decomposition for each rank of the tensor polarization.

$$\begin{aligned} \mathcal{L}_{\mu\nu} = {} & \mathcal{L}_{\mu\nu}^{(0)\chi^0} + P_1 \mathcal{L}_{\mu\nu}^{(1)\chi^0} + P_2 \mathcal{L}_{\mu\nu}^{(2)\chi^0} + P_3 \mathcal{L}_{\mu\nu}^{(3)\chi^0} \\ & + \cos\chi \left(P_1 \mathcal{L}_{\mu\nu}^{(1)\chi^1} + P_2 \mathcal{L}_{\mu\nu}^{(2)\chi^1} + P_3 \mathcal{L}_{\mu\nu}^{(3)\chi^1} \right) \\ & + \cos^2\chi \left(P_2 \mathcal{L}_{\mu\nu}^{(2)\chi^2} + P_3 \mathcal{L}_{\mu\nu}^{(3)\chi^2} \right), \end{aligned} \tag{C.8}$$

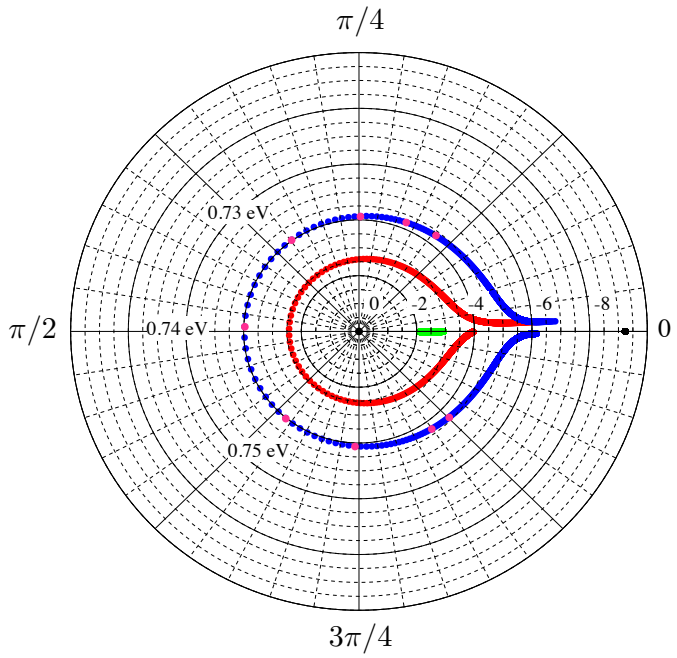

Figure C.3: Polar representation of the neutron energy dependence of each element of the $\mathcal{W}^\mu$ matrix. The radius is defined as $\mathcal{W}^\mu$ and the argument is $\arg(\mathcal{W}^\mu)$. The black, green, red, and blue dots represent $10\log|\mathcal{W}^0|$, $10\log|\mathcal{W}^1|$, $\log|\mathcal{W}^2|$, $\log|\mathcal{W}^3|$, respectively. The dots are plotted every 0.001 eV, and the pink dots are plotted every 0.01 eV. Since the real parts of $\mathcal{W}^2$ and $\mathcal{W}^3$ change their sign in p-wave resonance, their phases change rapidly vicinity of the p-wave resonance.

where the index i in matrix $\mathcal{L}_{\mu\nu}^{(i)\chi^k}$ represents the rank of the proportional tensor polarization, and k represents the power exponent of the proportional $\cos^i\chi$. Therefore, by controlling the tilt angle χ and the polarization P_i, each element is determined from its dependence.

Bibliography

[1] G. Aad, T. Abajyan, B. Abbott, *et al.*, "Observation of a new particle in the search for the Standard Model Higgs boson with the ATLAS detector at the LHC," *Physics Letters B*, vol. 716, no. 1, pp. 1 – 29, 2012.

[2] S. Chatrchyan, V. Khachatryan, A. Sirunyan, *et al.*, "Observation of a new boson at a mass of 125 GeV with the CMS experiment at the LHC," *Physics Letters B*, vol. 716, no. 1, pp. 30 – 61, 2012.

[3] G. Hinshaw, D. Larson, E. Komatsu, *et al.*, "Nine-year Wilkinson Microwave Anisotropy Probe (WMAP) observations: cosmological parameter results," *The Astrophysical Journal Supplement Series*, vol. 208, no. 2, p. 19, 2013.

[4] A. D. Sakharov. *JETP Lett.*, vol. 5, p. 24, 1967.

[5] A. M. Sirunyan, A. Tumasyan, W. Adam, , *et al.*, "Search for supersymmetry in proton-proton collisions at 13 TeV using identified top quarks," *Physical Review D*, vol. 97, no. 1, p. 012007, 2018.

[6] P. D. Group, P. Zyla, R. Barnett, J. Beringer, O. Dahl, D. Dwyer, D. Groom, C.-J. Lin, K. Lugovsky, E. Pianori, *et al.*, "Review of particle physics," *Progress of Theoretical and Experimental Physics*, vol. 2020, no. 8, p. 083C01, 2020.

[7] R. D. Peccei and H. R. Quinn, "CP conservation in the presence of pseudoparticles," *Physical Review Letters*, vol. 38, no. 25, p. 1440, 1977.

[8] H.-Y. Cheng, "The strong CP problem revisited," *Physics Reports*, vol. 158, no. 1, pp. 1–89, 1988.

[9] M. Le Dall and A. Ritz, "CP-violation and electric dipole moments," *Hyperfine Interactions*, vol. 214, no. 1, pp. 87–95, 2013.

[10] C. Abel, S. Afach, N. J. Ayres, *et al.*, "Measurement of the Permanent Electric Dipole Moment of the Neutron," *Phys. Rev. Lett.*, vol. 124, p. 081803, Feb 2020.

[11] M. Pospelov and A. Ritz, "Electric dipole moments as probes of new physics," *Annals of Physics*, vol. 318, no. 1, pp. 119 – 169, 2005. Special Issue.

[12] J. H. Smith, E. M. Purcell, and N. F. Ramsey *Phys. Rev.*, vol. 108 (1), pp. 120–122, 1957.

[13] P. D. Miller, f. W. B.Dress, J. K. Baird, and N. F. Ramsey *Phys. Rev, Lett.*, vol. 19 (7), pp. 381–384, 1967.

[14] W. B. Dress, J. K. Baird, P. D. Miller, and N. F. Ramsey *Phys. Rev.*, vol. 170 (5), pp. 1200–1206, 1968.

[15] J. K. Baird, P. D. Miller, W. B. Dress, and N. F. Ramsey *Phys. Rev.*, vol. 179 (5), pp. 1285–1291, 1969.

[16] W. B. Dress, P. D. Miller, and N. F. Ramsey *Phys. Rev. D.*, vol. 7 (11), pp. 3147–3149, 1973.

[17] W. B. Dress, P. D. Miller, J. M. Pendlebury, *et al. Phys. Rev. D.*, vol. 15(1), pp. 9–21, 1977.

[18] I. S. Altarev, Y. V. Borisov, A. B. Brandin, *et al. Nuc. Phys. A*, vol. 341(2), pp. 269–283, 1980.

[19] I. S. Altarev, Y. V. Borisov, A. B. Brandin, *et al. Phys. Lett.*, vol. 102B (1), pp. 13–16, 1981.

[20] J. M. JPendlebury, K. Smith, Golub, *et al. Phys. Lett*, vol. 136B (5,6), pp. 327–330, 1984.

[21] I. S. Altarev, Y. V. Borisov, A. B. Brandin, *et al. JETP. Lett.*, vol. 44, no. 8, pp. 460–464, 1986.

[22] K. Smith, N. Crampin, J. Pendlebury, *et al.*, "A search for the electric dipole moment of the neutron," *Physics Letters B*, vol. 234, no. 1, pp. 191 – 196, 1990.

[23] I. S. Altarev, Y. V. Borisov, N. V. Borovikova, *et al. Phys. Lett. B*, vol. 276, pp. 242–246, 1992.

[24] P. G. Harris, C. A. Baker, K. Green, *et al. Phys. Rev. Lett.*, vol. 85, no. 1, pp. 904–907, 1999.

[25] C. A. Baker, D. D. Doyle, P. Geltenbort, *et al. Phys. Rev. Lett.*, vol. 97, p. 131801, 2006.

[26] O. P. Sushkov and V. V. Flambaum, "Parity breaking in the interaction of neutrons with heavy nuclei," *Soviet Physics Uspekhi*, vol. 25, pp. 1–12, jan 1982.

[27] V. Gudkov, "On CP violation in nuclear reactions," *Physics Reports*, vol. 212, no. 2, pp. 77 – 105, 1992.

[28] J. D. Bowman and V. Gudkov, "Search for time reversal invariance violation in neutron transmission," *Phys. Rev. C*, vol. 90, p. 065503, Dec 2014.

[29] Y.H.Song, R. Lazauskas, and V. Gudkov *Phys. Rev. C.*, vol. 83, p. 065503, 2011.

[30] T. Okudaira, S. Takada, K. Hirota, *et al.*, "Angular distribution of γ rays from neutron-induced compound states of ^{140}La," *Phys. Rev. C*, vol. 97, p. 034622, Mar 2018.

[31] D. Nagle, J. Bowman, C. Hoffman, *et al.*, "High energy physics with polarized beams and polarized targets," in *by GH Thomas, AIP Conference Proceedings*, no. 51, p. 224, 1978.

[32] R. Balzer, R. Henneck, Jacquemart, *et al.*, "Parity violation in proton-proton scattering at 45 Mev," *Phys. Rev. C*, vol. 30, pp. 1409–1430, Nov 1984.

[33] P. von Rossen, U. von Rossen, and H. E. Conzett, "Test of parity conservation in *pp* scattering at 46 MeV," *AIP Conference Proceedings*, vol. 69, no. 2, pp. 1442–1445, 1981.

[34] V. Yuan, H. Frauenfelder, R. W. Harper, *et al.*, "Measurement of Parity Nonconservation in the Proton-Proton Total Cross Section at 800 MeV," *Phys. Rev. Lett.*, vol. 57, pp. 1680–1683, Oct 1986.

[35] V. Alfimenkov, S. Borzakov, V. T. Vo, *et al.*, "Experimental investigation of parity violating effect in the ^{117}Sn neutron p resonance," tech. rep., Joint Inst. for Nuclear Research, 1981.

[36] V. P. Alfimenkov, S. B. Borzakov, V. V. Thuan, Y. D. Mareev, L. B. Pikelner, A. S. Khrykin, and E. I. Sharapov *Nucl. Phys. A*, vol. 435, p. 352, 1983.

[37] G. Mitchell, J. Bowman, S. Penttilä, *et al.*, "Parity violation in compound nuclei : experimental methods and recent results," *Physics Reports*, vol. 354, no. 3, pp. 157 – 241, 2001.

[38] D. Blyth, J. Fry, N. Fomin, *et al.*, "First observation of p-odd γ Asymmetry in Polarized Neutron Capture on Hydrogen," *Phys. Rev. Lett.*, vol. 121, p. 242002, Dec 2018.

[39] A. Abragam and M. Goldman, "Principles of dynamic nuclear polarisation," *Reports on Progress in Physics*, vol. 41, pp. 395–467, mar 1978.

[40] Koga, Jun, Takada, Shusuke, Yoshioka, Tamaki, *et al.*, "Measurement of the angular distribution of prompt gamma-rays emitted in the ^{117}Sn(n,γ) reaction for a T-violation search," *EPJ Web Conf.*, vol. 219, p. 09004, 2019.

[41] Endo, Shunsuke, Shimizu, Hirohiko M., Kitaguchi, Masaaki, *et al.*, "Measurement of the angular distribution of γ rays emitted from the compound state after neutron capture by ^{81}Br for a search of T-violation," *EPJ Web Conf.*, vol. 219, p. 09003, 2019.

[42] P. Hautle and M. Iinuma, "Dynamic nuclear polarization in crystals of Nd^{3+}: $LaAlO_3$, a polarized ^{139}La target for a test of time-reversal invariance," *Nuclear Instruments and Methods in Physics Research Section A: Accelerators, Spectrometers, Detectors and Associated Equipment*, vol. 440, no. 3, pp. 638–642, 2000.

[43] C. Von Borczyskowski and E. Boroske, "Nuclear quadrupole resonance after nuclear polarisation during an optical pumping cycle," *Chemical Physics*, vol. 35, no. 3, pp. 367–374, 1978.

[44] R. Vilhjalmsson and J. Köppen, "Dynamic nuclear polarization of tin-119 nuclei in free radical solutions," *Chemical Physics Letters*, vol. 50, no. 3, pp. 442–444, 1977.

[45] M. Bulatowicz, R. Griffith, M. Larsen, *et al.*, "Laboratory Search for a Long-Range T-Odd, P-Odd Interaction from Axionlike Particles Using Dual-Species Nuclear Magnetic Resonance with Polarized ^{129}Xe and ^{131}Xe Gas," *Physical review letters*, vol. 111, no. 10, p. 102001, 2013.

[46] B. Gotschy, G. Denninger, H. Obloh, W. Wilkening, and J. Schneider, "Overhauser shift and dynamic nuclear polarization in InP," *Solid State Communications*, vol. 71, no. 7, pp. 629 – 632, 1989.

[47] V. Flambaum and O. Sushkov, "Angular and polarization correlations in the (n,γ) reaction," *Nuclear Physics A*, vol. 435, no. 2, pp. 352 – 380, 1985.

[48] A. Sonzogni, "Nudat 2.0: Nuclear structure and decay data on the internet," in *AIP Conference Proceedings*, vol. 769, pp. 574–577, American Institute of Physics, 2005.

[49] S. F. Mughabghab, *Atlas of Neutron Resonances: Resonance Parameters and Thermal Cross Sections. Z= 1-100*. Elsevier, 2006.

[50] K. SHIBATA, O. IWAMOTO, T. NAKAGAWA, *et al.*, "Jendl-4.0: A new library for nuclear science and engineering," *Journal of Nuclear Science and Technology*, vol. 48, no. 1, pp. 1–30, 2011.

[51] R. Terlizzi, U. Abbondanno, G. Aerts, *et al.*, "The ^{139}La (n, γ) cross section: Key for the onset of the s-process," *Physical Review C*, vol. 75, no. 3, p. 035807, 2007.

[52] G. Hacken, J. Rainwater, H. Liou, *et al.*, "Neutron resonance spectroscopy: ^{139}La," *Physical Review C*, vol. 13, no. 5, p. 1884, 1976.

[53] J-PARC, "Web site of J-PARC." https://j-parc.jp/c/index.html.

[54] K. Kino, M. Furusaka, F. Hiraga, *et al.*, "Measurement of energy spectra and spatial distributions of neutron beams provided by the ANNRI beamline for capture cross-section measurements at the J-PARC/MLF," *Nuclear Instruments and Methods in Physics Research Section A: Accelerators, Spectrometers, Detectors and Associated Equipment*, vol. 626, pp. 58–66, 2011.

[55] A. Kimura, T. Fujii, S. Fukutani, *et al.*, "Neutron-capture cross-sections of ^{224}Cm and ^{246}Cm measured with an array of large germanium detectors in the ANNRI at J-PARC/MLF," *Journal of nuclear science and technology*, vol. 49, no. 7, pp. 708–724, 2012.

[56] T. Kin, K. Furutaka, S. Goko, *et al.*, "Development of a 4π germanium spectrometer for nuclear data measurements at J-PARC," in *2009 IEEE Nuclear Science Symposium Conference Record (NSS/MIC)*, pp. 1194–1197, IEEE, 2009.

[57] S. Takada, T. Okudaira, F. Goto, *et al.*, "Characterization of germanium detectors for the measurement of the angular distribution of prompt -rays at the ANNRI in the MLF of the J-PARC," *Journal of Instrumentation*, vol. 13, pp. P02018–P02018, feb 2018.

[58] T. Nakao, K. Terada, A. Kimura, *et al.*, "Developments of a new data acquisition system at ANNRI," *EPJ Web Conf.*, vol. 146, p. 03021, 2017.

[59] K. Shibata, O. Iwamoto, T. Nakagawa, N. Iwamoto, A. Ichihara, S. Kunieda, S. Chiba, K. Furutaka, N. Otuka, T. Ohsawa, T. Murata, H. Matsunobu, A. Zukeran, S. Kamada, and J. Katakura, "Jendl-4.0: A new library for nuclear science and engineering," *J. Nucl. Sci. Technol*, vol. 48, pp. 1–30, 2011.

[60] CAEN, "Web site of CAEN." https://www.caen.it/.

[61] T. E. Chupp, M. E. Wagshul, K. P. Coulter, *et al.*, "Polarized, high-density, gaseous ^{3}He targets," *Phys. Rev. C*, vol. 36, pp. 2244–2251, Dec 1987.

[62] E. Babcock, I. Nelson, S. Kadlecek, *et al.*, "Hybrid Spin-Exchange Optical Pumping of ^{3}He," *Physical review letters*, vol. 91, no. 12, p. 123003, 2003.

[63] S. Kadlecek, *Spin Relaxation in Alkali Vapors*. University of Wisconsin–Madison, 1999.

[64] J. T. Singh, P. A. Dolph, W. A. Tobias, , *et al.*, "Development of high-performance alkali-hybrid polarized ^{3}He targets for electron scattering," *Physical Review C*, vol. 91, no. 5, p. 055205, 2015.

[65] B. Chann, E. Babcock, L. Anderson, *et al.*, "Measurements of ^{3}He spin-exchange rates," *Physical Review A*, vol. 66, no. 3, p. 032703, 2002.

[66] A. Abragam, "Principles of Nuclear Magnetism. Chap.8," *Oxford Univ. Press, London/New York. WALMSLEY, RH, AND SHPORER, M.(1978) J. Chem. Phys*, vol. 68, pp. 2584–2590, 1961.

[67] N. Newbury, A. Barton, G. Cates, *et al.*, "Gaseous ^{3}He magnetic dipolar spin relaxation," *Physical Review A*, vol. 48, no. 6, p. 4411, 1993.

[68] G. D. Cates, D. J. White, T.-R. Chien, *et al.*, "Spin relaxation in gases due to inhomogeneous static and oscillating magnetic fields," *Phys. Rev. A*, vol. 38, pp. 5092–5106, Nov 1988.

[69] Meeker, D. C. , "Finite Element Method Magnetics." http://www.femm.info.

[70] T. Oku, H. Hayashida, H. Kira, *et al.*, "Development of Compact Laser Optics for an In-situ Spin-Exchange Optical Pumping ^{3}He Neutron Spin Filter,"

[71] H. M. Shimizu *Mem. Fac. Sci. Kyoto Univ. Ser. Phys. Astrophys. Chem*, vol. 38, pp. 203–251, 1992.

[72] V. Alfimenkov, Y. D. Mareev, V. Novitskii, L. Pikel'Ner, and V. Skoi, "Interaction of polarized neutrons with polarized La nuclei and the structure of the cross section at energies up to 20 eV," *Physics of Atomic Nuclei*, vol. 57, no. 11, pp. 1854–1857, 1994.

[73] C. Abel, S. Afach, N. J. Ayres, *et al.*, "Measurement of the permanent electric dipole moment of the neutron," *Physical Review Letters*, vol. 124, no. 8, p. 081803, 2020.

[74] W. C. Griffith, M. D. Swallows, T. H. Loftus, *et al.*, "Improved limit on the permanent electric dipole moment of ^{199}Hg.," *Phys. Rev.Lett.*, vol. 102, p. 101601, 2009.

[75] E. G. Adelberger and W. C. Haxton, "Parity Violation in the Nucleon-Nucleon Interaction," *Ann. Rev. Nucl. Part. Sci.*, vol. 35, pp. 501–558, 1985.

[76] W. C. Haxton and E. M. Henley, *Symmetries and Fundamental Interactions in Nuclei*. WORLD SCIENTIFIC, 1995.

[77] W.C.HAXTON, *NUCLEAR CONSTRAINTS ON THE WEAK NUCLEON-NUCLEON INTERACTION*, pp. 75–85.

[78] J. Wasem, "Lattice QCD calculation of nuclear parity violation," *Phys. Rev. C*, vol. 85, p. 022501, Feb 2012.

[79] V. Gudkov and H. M. Shimizu, "Neutron spin dynamics in polarized targets," *Phys. Rev. C*, vol. 102, p. 015503, Jul 2020.

[80] V. Baryshevsky, *High-energy Nuclear Optics Of Polarized Particles*. World Scientific Publishing Company, 2012.